



Universiteit  
Leiden  
The Netherlands

## Low energy electron transmission through layered materials and chiral organic films

Neu, P.S.

### Citation

Neu, P. S. (2024, June 12). *Low energy electron transmission through layered materials and chiral organic films*. Retrieved from <https://hdl.handle.net/1887/3762501>

Version: Publisher's Version

License: [Licence agreement concerning inclusion of doctoral thesis in the Institutional Repository of the University of Leiden](#)

Downloaded from: <https://hdl.handle.net/1887/3762501>

**Note:** To cite this publication please use the final published version (if applicable).

LOW ENERGY ELECTRON TRANSMISSION  
THROUGH LAYERED MATERIALS  
AND CHIRAL ORGANIC FILMS

Proefschrift

ter verkrijging van

de graad van doctor aan de Universiteit Leiden,

op gezag van rector magnificus prof.dr.ir. H. Bijl,

volgens besluit van het college voor promoties

te verdedigen op woensdag 12 juni 2024

klokke 13:45 uur

door

Peter Sebastian Neu

geboren te Duisburg, Duitsland

Promotores:

Prof.dr.ir. S.J. van der Molen

Prof.dr.ir. R.M. Tromp

Promotiecommissie:

Prof.dr. C. Kumpf (Forschungszentrum Jülich GmbH)

Dr. Z. Zanolli (Universiteit Utrecht)

Prof.dr. J. Aarts

Prof.dr. M.P. van Exter

Prof.dr.ir. T.H. Oosterkamp

Prof.dr. J.M. van Ruitenbeek

An electronic version of this thesis is available at

<https://scholarlypublications.universiteitleid.nl/>.

Printed by Gildeprint in Enschede.

The work presented in this dissertation was funded by the Dutch Research Council (NWO).

The cover shows an optical micrograph of molybdenum disulfide ( $\text{MoS}_2$ ) flakes during sample preparation. The mechanically exfoliated  $\text{MoS}_2$  flakes are brought into contact with a holey transmission electron microscopy grid. The colorful optical interference fringes appear when the polymer stamp (with the  $\text{MoS}_2$  flakes attached) is almost in contact with the substrate.







# CONTENTS

<b>1 INTRODUCTION</b> .....	<b>1</b>
1.1 VAN DER WAALS MATERIALS .....	2
1.2 PROBING VAN DER WAALS MATERIALS WITH ELECTRONS .....	3
1.3 ELECTRON-MATTER INTERACTIONS .....	5
1.3.1 <i>Elastic electron scattering: the electron wave</i> .....	5
1.3.2 <i>Elastic and Inelastic Mean Free Path</i> .....	8
1.4 CHIRALITY.....	9
1.4.1 <i>Chirality-Induced Spin Selectivity (CISS)</i> .....	11
1.5 OUTLINE OF THIS THESIS.....	14
REFERENCES .....	15
<b>2 LOW-ENERGY ELECTRONS: MICROSCOPY AND SPECTROSCOPY</b> .....	<b>19</b>
2.1 INTRODUCTION .....	20
2.2 THE ESCHER SETUP.....	20
2.3 LOW-ENERGY ELECTRON MICROSCOPY (LEEM).....	21
2.4 ELECTRON VOLT-TRANSMISSION ELECTRON MICROSCOPY (eV-TEM) .....	23
2.5 PHOTOEMISSION ELECTRON MICROSCOPY (PEEM) WITH POLARIZED LIGHT .....	25
REFERENCES .....	27
<b>3 EXTRACTING TRANSVERSE ELECTRON MEAN FREE PATHS IN GRAPHENE AT LOW ENERGY</b> .....	<b>29</b>
ABSTRACT.....	29
3.1 INTRODUCTION .....	30
3.2 INTERFERENCE MODEL WITH LOSSES .....	31
3.3 RESULTS.....	33
3.4 CONCLUSIONS .....	38
APPENDIX.....	39
REFERENCES .....	40
<b>4 SYMMETRIES OF ELECTRON INTERACTIONS WITH HBN-GRAPHENE HETEROSTACKS</b> .....	<b>43</b>
4.1 INTRODUCTION .....	44
4.2 RESULTS .....	44
4.2.1 <i>Geometry and images</i> .....	44
4.2.2 <i>Spectra</i> .....	47
4.2.3 <i>Calculated spectra and electron density distributions</i> .....	51
4.2.4 <i>Elastic and inelastic mean free paths</i> .....	54
4.2.5 <i>Symmetry upon flipping the sample</i> .....	56
4.3 CONCLUSION .....	60
APPENDIX.....	62
<i>Sample fabrication</i> .....	62
<i>Flipped sample</i> .....	63
<i>Free-standing hBN</i> .....	63
REFERENCES .....	65

<b>5 ELECTRON TRANSMISSION AND MEAN FREE PATH IN MOLYBDENUM DISULFIDE AT ELECTRONVOLT ENERGIES .....</b>	<b>69</b>
ABSTRACT.....	69
5.1 INTRODUCTION.....	70
5.2 EXPERIMENT.....	70
5.3 RESULTS.....	71
5.4 DISCUSSION.....	76
5.5 SUMMARY .....	77
APPENDIX.....	78
<i>Optical Images</i> .....	78
<i>Projected Density of States</i> .....	78
<i>Mean Free Path: comparing with previous work</i> .....	79
REFERENCES .....	80
<b>6 PHOTOEMISSION FROM CHIRAL MOLECULE FILMS .....</b>	<b>83</b>
6.1 INTRODUCTION.....	84
6.2 EXPERIMENTAL .....	86
6.2.1 <i>Linear polarization and photoemission</i> .....	86
6.2.2 <i>Principal tests on gold structures</i> .....	88
6.2.3 <i>Polarization-dependent Photoemission from BINAP</i> .....	90
6.2.4 <i>Further calculation of transmitted polarization</i> .....	98
6.3 CONCLUSIONS AND RECOMMENDATIONS .....	99
REFERENCES .....	101
<b>SUMMARY.....</b>	<b>105</b>
<b>SAMENVATTING.....</b>	<b>107</b>
<b>ZUSAMMENFASSUNG .....</b>	<b>111</b>
<b>ACKNOWLEDGEMENTS.....</b>	<b>115</b>
<b>CURRICULUM VITAE .....</b>	<b>117</b>
<b>LIST OF PUBLICATIONS.....</b>	<b>119</b>





# 1 INTRODUCTION

## 1.1 Van der Waals materials

Graphene, a material consisting of carbon atoms arranged in a planar hexagonal lattice, exhibits many mechanical and electronic properties intrinsically linked to its two-dimensional (2D) nature. Although monolayer graphene is only one atom thick, it is surprisingly strong [1–3], making it ideal as a membrane for electron microscopy. The mechanical strength comes from the covalent bonds between the carbon atoms, that naturally all occur in a plane. Furthermore, the electronic properties resulting from the 2D honeycomb structure are remarkable: the band structure of graphene has a linear dispersion relation at the Fermi level, also called a photon-like dispersion [4]. In other words, the electrons have zero effective mass.

When going from one layer of graphene to two layers, i.e., bilayer graphene, even more interesting electronic properties may occur. In the natural stacking, where the second hexagonal lattice is shifted by half a diagonal of the hexagon (AB or Bernal stacking), the valence and conduction band avoid each other parabolically (zero bandgap semiconductor) [5]. However, when stacking two graphene layers with a twist angle of approximately  $1.1^\circ$ , called the magic angle, such ‘twisted bilayer graphene’ (TBG) was shown to be superconducting [6]. The associated flat bands [7] are a result of the larger moiré superlattice forming due to the twist and were predicted for certain, magic angles only [8].

The crucial step towards graphene research was to separate single graphene layers from the mother material graphite by the so-called ‘scotch-tape exfoliation’ method [9]. Graphite can be seen as a crystal in which many graphene layers are on top of each other, with a weak, van der Waals coupling between these layers. Therefore, layers of graphene can be pulled apart from the graphite by sticking scotch tape to the top and bottom. By iteratively applying this scotch-tape exfoliation method the first monolayer graphene samples were produced from graphite, a method that led to the Physics Nobel prize for Geim and Novoselov.

Graphene is not the only material that can be thinned down to single layers; there is an entire family. Such materials, that only have relatively weak van der Waals bonds between well-defined layers and covalent bonds within the layers, are known as the class of van der Waals (vdW) materials. Van der Waals materials come in different forms, varying from graphene, with a purely planar structure and only carbon atoms, to more complicated structures containing several atomic species per unit layer.

The electrical properties of vdW materials strongly depend on the number of layers. For example, a monolayer of molybdenum disulfide ( $\text{MoS}_2$ ) is a direct band gap semiconductor, but a  $\text{MoS}_2$  multilayer has an indirect band gap. Furthermore, the low defect density (per area) makes few-layer materials suitable as single photon emitters [10]. Imaging 2D materials with low energy electrons will allow us to identify sample areas of different composition and band structure, that typically form in the growth and fabrication process.

The systems studied in this thesis are sketched in Figure 1.1. They reach from the conducting graphene (a), via the insulating hexagonal boron nitride (hBN, b) consisting of two elements in the same plane, to semiconducting molybdenum disulfide ( $\text{MoS}_2$ , c), a so-called transition metal dichalcogenide, or TMD. The materials in Figure 1.1 all share a 2D honeycomb structure. Out of plane, these layers can be arranged differently, with the preferred atomic orientation shown

in the bottom row.  $\text{MoS}_2$  is different from graphene and hBN, as the atoms in a unit layer are still arranged in different atomic sheets, with the Mo plane sandwiched between the S plane. This also allows for more variations in vertical stacking, known as polytypes, with the 2H polytype (Mo atoms and S atoms alternating in-plane positions each layer) being the most stable.

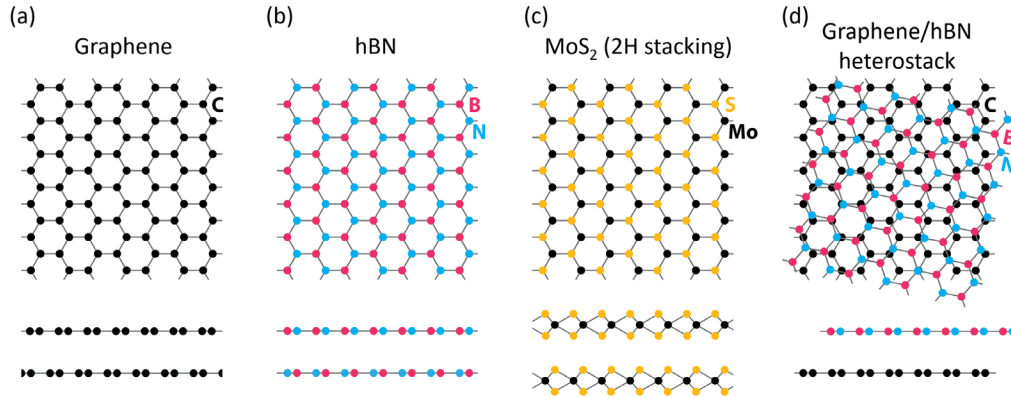


Figure 1.1: Atomic lattices of the two-dimensional materials studied in this thesis: graphene (a), hexagonal boron nitride (hBN, b), molybdenum disulfide ( $\text{MoS}_2$ , c) and a heterostack (d) of hexagonal boron nitride on top of graphene. The top row shows the in-plane structure. Note that only one layer is shown for the crystals a-c, whereas one layer of graphene and one layer of hBN is shown for the heterostack (d). The bottom row shows a side view of two layers. For the graphene, hBN and  $\text{MoS}_2$  the preferred stacking order is shown.

By stacking layers of van der Waals materials, one can create materials that do not occur in nature. The resulting stack will thus have (electronic) material properties that differ from the original material(s). This is to some extent comparable to a reaction in chemistry, but easily reversible as the layers could be peeled apart again, the interaction between layers being relatively weak. After seeing the diversity of phenomena enabled by stacking two graphene layers, we can only imagine the rich possibilities of combining different van der Waals materials layer by layer.

In Figure 1.1d, a heterostack of hBN on graphene breaking the top-down symmetry of the system is shown. The graphene-hBN heterostack is common in experiments, as a hBN substrate is used for its insulating and flatness properties in device fabrication. Typically, the twist angle, randomly chosen in Fig. 1.1d, is not controlled. Part of the emergent electronic band structure of such a heterostack is investigated in Chapter 4.

## 1.2 Probing van der Waals materials with electrons

In this thesis, we will probe van der Waals materials using low energy electrons that have an energy range of about 0-50 eV. The basic experiment is shown in Figure 1.2: Electrons with a tunable energy  $E$  (above the vacuum energy) are directed towards the sample, e.g., a freestanding bilayer of  $\text{MoS}_2$  as depicted in Figure 1.2. The electrons hit the sample at perpendicular incidence to the surface. Then the electron waves are either transmitted or reflected with a certain probability strongly depending on the electron energy. We note that the



point where the electrons are reflected is not well defined (like the arrow in Fig. 1.2 may suggest), as the scattering process is quantum mechanical. In practice, some electrons will also be scattered inelastically and/or absorbed by the material.

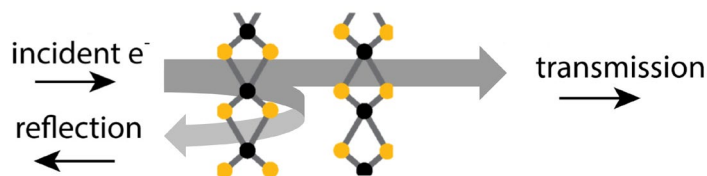


Figure 1.2: The basic idea of a reflection/transmission experiment with low-energy electrons. Electrons traveling in a vacuum are directed towards a few-layered sample. The electrons hit the sample (at perpendicular incidence to the 2D planes). The electron flux is partially reflected and partially transmitted.

In terms of experimental techniques, imaging the reflected electrons is known as low energy electron microscopy (LEEM) and imaging the transmitted electrons is named electron Volt-transmission electron microscopy (eV-TEM) [11]. Imaging refers to acquiring a spatially resolved image of the sample, rather than recording one reflectivity or transmissivity value. Recording a well-resolved 2D image of the sample is important, as samples typically consist of areas of different thickness and composition, resulting in different reflectivity/transmissivity. The microscopy techniques used will be described in more detail in Chapter 2.

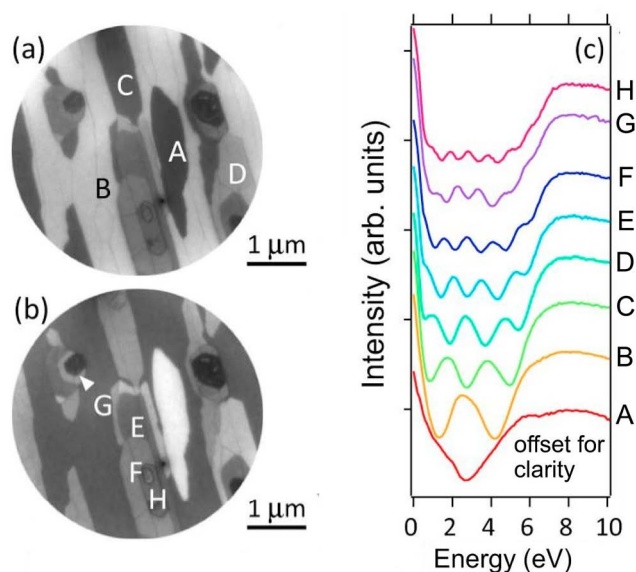


Figure 1.3: LEEM images of multilayer graphene grown on 4H-SiC recorded at 2.5 eV (a) and 4.5 eV (b) electron energy. Different brightness indicates different layer counts of graphene. The reflection spectra (c) recorded at the areas indicated in the image allow for determining the number of graphene layers by counting the number of minima between 0 to 6 eV (not counting the buffer layer). Reprinted from H. Hibino et al. [12].

As an example, two LEEM images (recorded at different electron energies by Hibino et al. [12]) of multilayer graphene grown on 4H silicon carbide (4H-SiC) are shown in Figure 1.3a/b. We see different areas of different brightness, where brighter means a higher electron reflectivity

at that energy. The LEEM reflection spectra, i.e., the reflectivity as a function of energy, of areas A-H are shown in Figure 1.3c. The spectrum of area A has one minimum in the 0-6 eV energy range. It has been shown [13,14] that this single minimum is characteristic of one layer of graphene on top of a graphene-like buffer layer (an electrically insulating layer that is partially bound to the underlying SiC). For each additional graphene layer, the minimum splits, such that the graphene layer number (not including the buffer layer) can be counted by counting the low-energy reflection minima. Above five minima (area E) it becomes unclear how to count the minima, as the lowest oscillations move below the vacuum level (zero energy) and oscillations above 6 eV move to the flank of the next feature in the spectrum. Still, the central minimum in area E becomes a maximum in F and again a minimum in G, and so on. We will model the reflection and transmission spectra of freestanding graphene with a model inspired by optical interference in Chapter 3.

## 1.3 Electron-Matter interactions

For electrons interacting with matter, the quantum-mechanical wave nature of the electron must be considered, with the de Broglie wavelength of the electron  $\lambda = h/\sqrt{2m_e E}$  (with the electron mass  $m_e$ ). For a rule of thumb estimate, this reduces to  $\lambda [\text{\AA}] \approx \sqrt{150/E[\text{eV}]}$ . Thus, the wavelength of few-eV electrons is comparable to lattice constants in crystals/van der Waals materials, which are typically in the order of Angstroms. The basic, elastic interaction of electrons with a van der Waals material can be understood from the quantum well model, known from quantum mechanics textbooks, as explored next [15,16].

### 1.3.1 Elastic electron scattering: the electron wave

The textbook example is the one-dimensional potential  $V$  shown in Figure 1.4a that takes a constant negative value  $V_0$  in a finite well from 0 to  $d$  (in the material with thickness  $d$ ) and is 0 otherwise (corresponding to the vacuum energy). To solve the scattering problem, i.e. find the amplitude of the reflected and transmitted electron wave at an energy  $E$ , we solve the stationary Schrödinger equation for the one-dimensional case

$$\left( -\frac{\hbar^2}{2m} \frac{d^2}{dx^2} + V(x) \right) \Psi(x) = E \Psi(x) \quad (1)$$

where  $\Psi(x)$  is the wave function and  $m$  is the electron mass.

For electrons with an energy above the vacuum level the Schrödinger equation of the quantum-well problem always has a solution (in fact two: the right-moving and left-moving electrons), called the unbound states<sup>1</sup>.

We solve the (stationary) Schrödinger equation with an ansatz where the incident electron wave is normalized to one, i.e.,  $\Psi_{\rightarrow, \text{vac}} = \exp(ikx)$ , and there are no incoming electrons from the

---

<sup>1</sup> One can show that the reflection and transmission probability is the same for electrons incident from the left as for electrons incident from the right [16].

right vacuum side (see Fig. 1.2). This will result in outgoing waves from both sides of the well, one representing reflection and one representing transmission. The resulting electron densities  $|\Psi^2|$ , which include possible interferences, at four chosen energies are shown in panel (b), with the energies indicated in the reflection spectrum in (c).

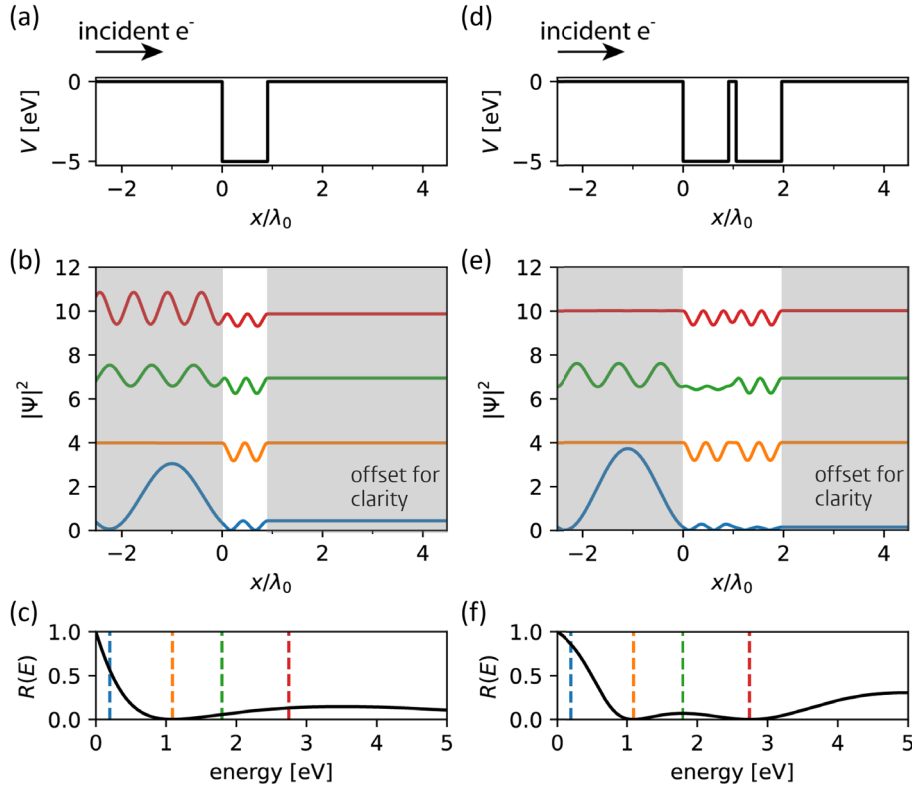


Figure 1.4: Quantum mechanical calculation of scattering of electrons from a finite quantum well (a) and a finite double well (d) with depth  $V_0 = -5$  eV. The electrons are incident from the vacuum ( $V = 0$ ) with an energy  $E$  above the vacuum level, like in a LEEM experiment. Panels b/e show the electron probability density for the respective cases at selected energies (marked in panels c/f). The calculated reflection spectra show one minimum for the single well and a second minimum forming for the double well in the plotted low-energy range. The spatial axis in (a, b, d, e) is given in units of the  $\lambda_0 = h/\sqrt{2m_e(0 - V_0)}$ , corresponding to the wavelength inside the well at  $E = 0$  incident energy. The probability density curves (b,e) are offset for clarity by 0, 3, 6, and 9, and the incoming electron wave amplitude is normalized to  $\hat{\Psi} = 1$ .

To the left of the sample, the incident and reflected wave interfere and produce oscillations in  $|\Psi|^2$ . The yellow curve in (b) does not show the oscillations on the vacuum side, as the reflection amplitude is zero at that energy. As we are not considering absorption, the full electron flux is transmitted at that energy. We will call the unbound states with enhanced transmission the transmission states, or states for short.

Figure 1.4d shows a double potential well, i.e., two wells like in (a) separated by a thin barrier. In addition to the reflection minimum of the single well (marked in yellow), a new minimum (marked in red) around 2.7 eV forms in the reflection spectrum (see Fig. 1.4f). In both minima the reflected intensity is zero, thus there is no interference of the wavefunctions in the vacuum

(Fig. 1.4e). While the 1.1 eV state (yellow) has a maximum of probability density at the barrier, the 2.7 eV state (red) has a minimum there. We used the quantum well example to introduce ‘transmission states’ and show how adding a layer can affect the reflection (and transmission) spectrum. For a generalization to multiple wells using the scattering matrix method we refer to [17]. Arranging the wells into a periodic lattice and solving the Schrödinger equation will yield a band structure (c.f. [16,18]). As long as we only consider a few layers of 2D materials, thus only a discrete set of wavevectors fitting the layer spacing, the transmission states are discrete points in the out-of-plane band structure.

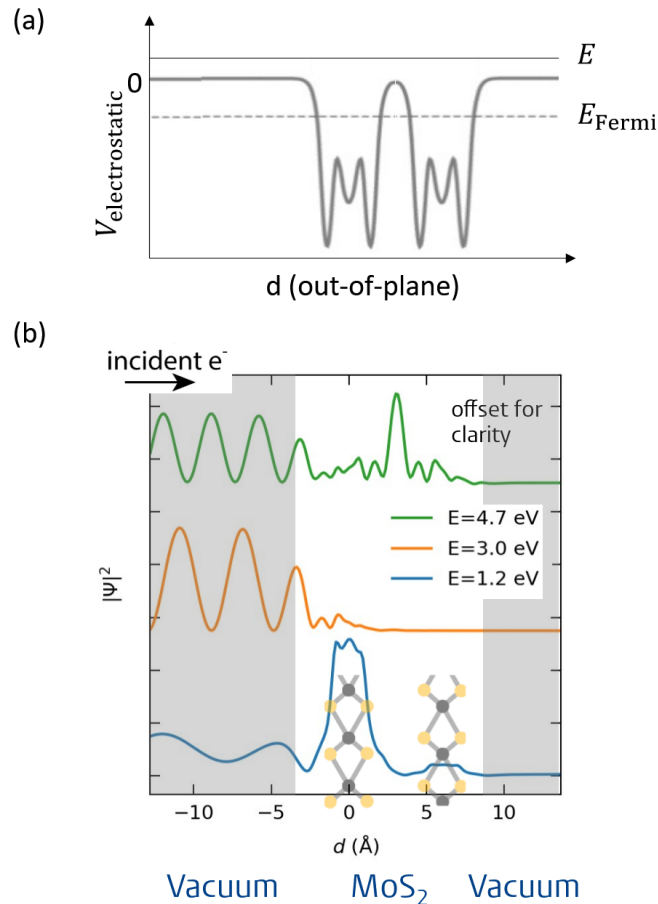


Figure 1.5: (a) Sketch of the electrostatic potential of bilayer MoS<sub>2</sub> projected onto the out-of-plane axis. The incident electron energy  $E$  is above the vacuum level (0) and the Fermi level ( $E_{\text{Fermi}}$ ). The electron density (b) is shown at 3 electron energies, illustrating a state centered in the layer (1.2 eV) and a state (4.7 eV), centered between the layers (‘interlayer state’). For an energy of 3.0 eV, there is no state available, and the signal is strongly attenuated within the material, leading to a relatively high reflectivity. The electron wave functions in MoS<sub>2</sub> were calculated in three dimensions (by E.E. Krasovskii, see Chapter 5) and then projected onto the out-of-plane axis. Panel a adapted from [19].

In reality, the potential well has to be replaced by the three-dimensional electrostatic potential in the material of interest to calculate the transmission and reflection probability of electrons. The electrostatic potential for bilayer MoS<sub>2</sub> and the solved electron density at three select energies are shown in Figure 1.5a and b, respectively. Both plots show the dependence on the out-of-plane dimension and are averaged along the two in-plane dimensions. All electron densities show characteristic oscillations on the left, as the electron wave incident from the left

interferes with its reflection. As all scattering is treated as elastic, the reflected and transmitted flux sum to the incident flux.

Remarkably, the electron density (Fig. 1.5b) at  $E = 1.2$  eV is centered in the MoS<sub>2</sub> layers, whereas the electron density at  $E = 4.7$  eV is centered in between the two layers. The states at  $E = 1.2$  eV and  $E = 4.7$  eV have a relatively high transmitted flux, while the electron density at  $E = 3.0$  eV is shown as an example of maximal reflection (thus minimal transmission). In terms of band structure (above the vacuum level), the high transmission states correspond to the existence of a (dispersive) band in the travel direction of the electrons (out-of-plane direction,  $\overline{\Gamma\Gamma}$  direction). We note that the band structure below the vacuum level, in particular at the Fermi level, cannot be imaged with electrons coming from and going to vacuum.

### 1.3.2 Elastic and Inelastic Mean Free Path

In addition to elastic scattering, the electrons will also undergo inelastic scattering processes, e.g., with phonons and plasmons. This will be discernible in our experiments, as we will filter in electron energy and angle. Electrons that lose energy to a value below the vacuum level are even absorbed in the material. In a macroscopic view, the characteristic length that an electron travels before being scattered is given by the energy-dependent mean free path (MFP)  $\lambda$ . Thus, the electron transmission probability through material of thickness  $d$  is generally given by  $p_T(E) = \exp(-d/\lambda(E))$ . Both inelastic and elastic scattering processes, with their respective mean free path lengths  $\lambda_{\text{inel.}}$  and  $\lambda_{\text{el.}}$ , contribute to the MFP with  $\lambda^{-1} = \lambda_{\text{inel.}}^{-1} + \lambda_{\text{el.}}^{-1}$ .

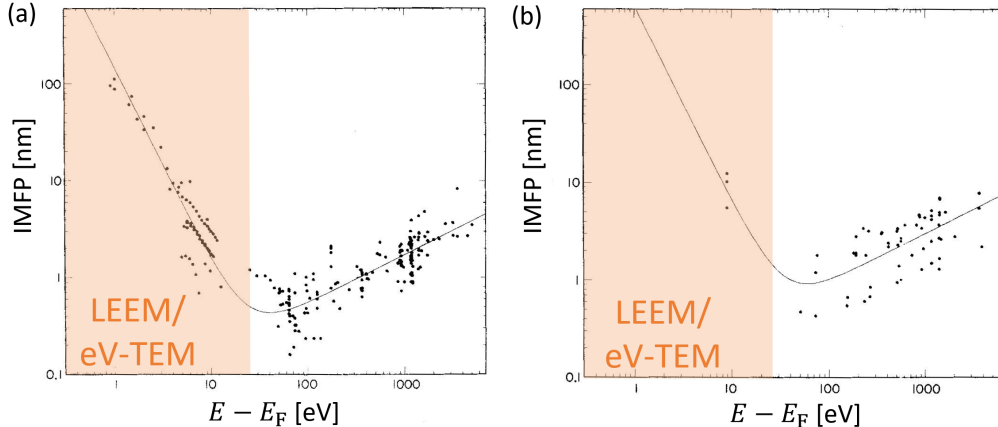


Figure 1.6: Inelastic electron mean free paths of elements (a) and inorganic compounds (b) compiled by Seah and Dench [20]. The data fit a general U-shape, called the ‘universal curve’, with a minimum at 30-40 eV (above the Fermi level). However, few data points are present (especially for inorganic compounds) in the low energy range where LEEM and eV-TEM operate. Data and fits from [20].

Although the MFP is a material property, the compilation of MFPs of different materials by Seah and Dench (reprinted in Fig. 1.5) shows that  $\lambda_{\text{inel.}}(E)$  follow the same curve remarkably well for different materials. This curve, generally called the ‘universal curve’, was fitted to the datapoints of elements (Fig. 1.5a) and inorganic compounds (Fig. 1.5b). The curve describes a U-shape with a minimum at about 30-40 eV above the Fermi level. Conventional transmission electron microscopes (TEM) operate at high energies (100-1000 keV), where the mean free

path is large, and the electrons can penetrate micron-scale samples. Intuitively, the electron MFP increases for higher energies, as the faster electrons have less time to interact with the sample [21].

The MFP also increases towards very low energies because some energy losses, e.g., due to plasmons, require a minimal energy transfer. The lower the electron energy, the fewer of these losses can be excited and the larger the MFP becomes again. This has allowed our group to introduce transmission electron microscopy at low energies – eV-TEM [11,22–24]. The energies discussed in low energy electron microscopy are typically around or below the ‘universal curve’ minimum.

The MFP gives an estimate of the probing depth of reflected low-energy electrons and the intensity of transmitted electrons. Vice versa, measuring the transmitted and reflected electron spectra will allow us to determine the inelastic and elastic mean free paths. We will fill in the inelastic MFP curves for the abovementioned 2D materials (Fig. 1.1), as the low-energy side of the MFP curve for inorganic compounds (Fig. 1.5b, not elements) rests on only a few data points.

Strictly speaking, the universal curve only applies to isotropic materials, although one can still expect the MFP to increase towards the lowest energies, as fewer loss mechanisms become excitable. We will treat two-dimensional materials at perpendicular incidence, which are clearly anisotropic. Based on the elastic scattering calculations above, we should expect to see oscillations in the (total) MFP in cases with little inelastic scattering. We will use LEEM and eV-TEM in combination to determine the MFP in much more detail than before, compare to photoemission experiments and test the universality of the ‘universal curve’ in Chapters 3-5.

## 1.4 Chirality

An object is chiral when it lacks mirror symmetry, i.e., it cannot be superimposed onto its mirror image by translation and rotation. The eponymous example is the hand (from Greek *kheir*,  $\chi\epsilon\iota\rho$  = hand): While our hands are mirror images of each other, they cannot be moved or rotated in a way such that they are exactly equal. We note that chirality is defined in the context of spatial dimensionality. If we draw the outline of a left hand and a right hand on a piece of paper, they cannot be overlaid in two dimensions. However, if we cut out the outline of the hands, we can use the third dimension to flip one hand upside down and overlay them.

A specific case of chirality are helical structures, like the helical staircases on either side of our office in Leiden shown in Figure 1.7a. Other examples of helices in our everyday life are screws, springs, fusilli pasta, and the double helix of DNA. When looking along the axis of a helix (down the staircase in Fig. 1.7a), moving forward can either describe a clockwise rotation or an anti-clockwise rotation. If it is a clockwise motion, we call the helix right-handed (like a regular screw), and left-handed otherwise. Flipping a helix upside down does not change its handedness, as the handedness is an inherent property and a special case of chirality.

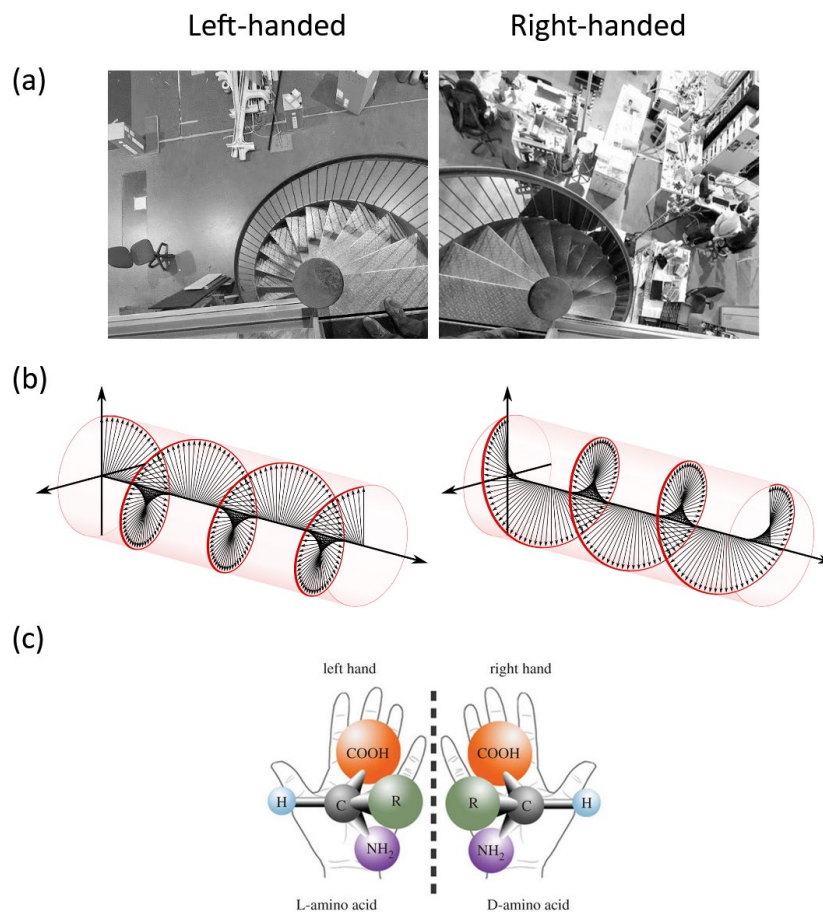


Figure 1.7: Examples of chirality, with the left-handed version on the left and the right-handed version on the right. The staircases (a) on either side of our office (Kamerlingh Onnes Laboratorium, Leiden University) are helical, with opposite handedness. For circularly polarized light (b), the electric field vector (of a wave frozen in time, optics textbook convention) describes a helix around the propagation direction. Molecules (c) that are chiral (but not necessarily helical) are named after their effect on light polarization: left-turning (levorotary, L) or right-turning (dextrorotary, D). The illustration (b) is licensed under the wikipedia creative commons license and reprinted from [25]. We acknowledge Inaki et al. [26] for publishing the figure in (c) in an open access article.

Also, the electric and magnetic fields of circularly polarized light describe a helix shown in Figure 1.7b. The naming convention (according to optics textbooks) for left-handed and right-handed circularly polarized light follows the same logic as for the other helices. The helix is described by the E-vectors of the circularly polarized light when the light wave is frozen in time (shown in Fig. 1.7b). In other words, looking from the point of the receiver, the electric field vector of right-handed light ascribes an anti-clockwise motion in a fixed plane over time.

In chiral molecules, it may not be obvious to assign which of the mirrored versions (enantiomers) is left- or right-handed. The handedness of molecules was first reported by Biot [27], who shone linear polarized light on liquids/solutions and observed a rotation of the polarization axis. Pasteur realized that the rotation of light is connected to the geometric structure of the molecules [28]. While identical in chemical composition, the two different enantiomers (like shown in Fig. 1.7c) with the atoms arranged in a mirrored way, rotate the



light the opposite way. Chiral molecules are named after the direction they rotate the linear polarization, like the amino acid shown in Figure 1.7c in its dextrorotatory (right-turning, D, sometimes denoted R or +) and levorotatory (left-turning, L, sometimes denoted S or -) form.

Chiral molecules are common in nature and play important roles in biological processes. The medical interest is large, as many drugs have effects and side-effects depending on their handedness. For example, ibuprofen is sold in a racemic mixture, although the dextrorotatory (D) isomer is the more biologically active [29]. The enantio-pure form is marketed as dexibuprofen or ibuprofen express. In other cases, the opposite enantiomer of a drug may be toxic, like (S)-Thalidomide that is produced in the body from (R)-Thalidomide [30]. Here, the active agent was marketed as Softenon/Contergan, with terrible consequences. Many children born to women taking this drug during pregnancy had severe birth defects.

Strikingly, most helical molecules in living beings are right-handed, an unexpected breaking of symmetry known as the homochirality of life [31,32]. Some proposed solutions to this puzzle hinge on deterministic externally induced mechanisms, e.g., due to cosmic rays or the rotation of the earth. Others explain homochirality as the result of probabilistic processes. Then autocatalysis, the catalysis of the same molecule with the same chirality, leads to an amplification [33] of an initially small, random imbalance.

### 1.4.1 Chirality-Induced Spin Selectivity (CISS)

Chirality-induced spin selectivity (CISS) was first observed in electrons photoemitted from a film of chiral molecules. The CISS effect describes an asymmetry of the spin population, or spin polarization, induced for electrons passing through chiral molecules. The effect is extraordinarily large and lacks a good understanding.

In 1999, Ray et al. [34] shone circularly polarized UV light on layers of stearoyl lysine and measured the photoemission yield. Their data is shown in Figure 1.8a. They reported a large difference in photoemissivity between left- and right-circularly polarized light for the film consisting of five layers of L-stearoyl lysine, which they attributed to a spin-filtering effect in the molecular film. As the spin-population photoemitted from the underlying gold depends on the handedness of the light [35], different transmissivities for each spin would lead to an intensity difference in detected electron flux. For five monolayers, consisting of 99% L-stearoyl lysine and 1% R-stearoyl lysine, they reported the absence of spin-selectivity (Fig. 1.8b), suggesting that spin-selectivity is indeed a collective phenomenon in the layer.

In a later photoemission experiment, Göhler et al. [36] directly measured the spin polarization of the photoelectrons emitted from monolayers of DNA, as shown in Figure 1.8c-e. The degree of spin-polarization  $P$  is defined as  $P = (I_p - I_{ap}) / (I_p + I_{ap})$  with  $I_{p/ap}$  being the count of electrons with spin parallel/anti-parallel to their direction of travel, respectively. Göhler et al. found a degree of polarization of up to  $P = -57\%$  (i.e., preferring spin anti-parallel to the direction of travel, see Fig. 1.8d) depending on the length of the DNA strands. The reported spin polarization of photoemitted electrons depends slightly on the polarization of the light, with  $|P|$  increasing from right circularly polarized light (Fig. 1.8c), over linearly polarized light (Fig. 1.8d) to left circularly polarized light (Fig. 1.8e). They attribute this dependence on light



polarization to the asymmetric spin-polarization (due to spin orbit coupling) of the electron population emitted from the underlying gold, which is then filtered by the chiral molecular layer. Independent of the light polarization, the majority of the spins is oriented anti-parallel to the direction of travel. For a compilation of spin polarizations measured in different chiral molecules see [37].

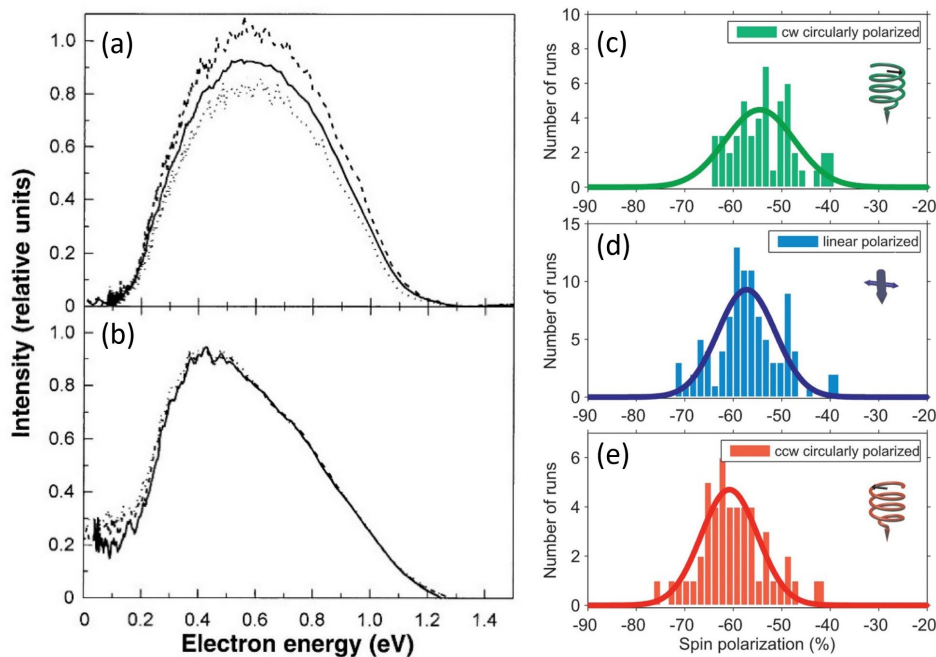


Figure 1.8: Photoemission experiments on chiral molecular layers. Ray et al. [34] measured a difference of photoemission intensity between right-handed circularly polarized light (dashed lines) and left-handed circularly polarized light (dotted lines) in layers of pure L-stearoyl lysine (a), whereas there was no such difference in the non-enantiopure layers (b). Later, Göhler et al. [36] measured the degree of spin polarization (parallel to the electron travel direction) of electrons photoemitted from DNA (c-e). The polarization of the light (indicated in c-e) changes the degree of spin-polarization, but the spin population is still polarized anti-parallel to the direction of travel in all cases. Reprinted from [34] (a,b) and [36] (c-e) with permission from AAAS.

In support of its discovery in photoemission experiments, CISS-related effects have also been reported in scanning tunneling microscopy (STM)/conductive atomic force microscopy (conductive AFM) experiments [38–40], spin-transport devices [41] and catalysis experiments [42–44]. While the scanning probe experiments can measure spin-dependent current-voltage spectra, it is often unclear whether they probe a single chiral molecule or a collective phenomenon of hundreds of molecules. Typically, STM/conductive AFM measurements of current-voltage (IV) curves show a high variance from site to site. This variability is attributed to both the contact of the STM/AFM tip to the molecule and the orientation/environment of the molecule itself. Hence, IV curves in these techniques are measured on hundreds of sites, to check if the average of these spectra shows the asymmetries typical of CISS [38]. Moreover, for all conductance experiments measuring the local

current/voltage, time reversal symmetry forbids a CISS effect at least in linear response, i.e., at low bias [45].

Effects related to CISS have also been shown in catalysis with help of chiral molecules. Chiral molecules (namely L/D-tryptophan, L-A3 and L-A11) attached to Fe<sub>3</sub>O<sub>4</sub> nanoparticles were shown to suppress the generation of H<sub>2</sub>O<sub>2</sub> byproduct in water splitting [42], in contrast to achiral molecules. The reported efficiency gain in catalysis by chiral molecules may be an explanation for the ubiquity of chiral molecules, and the homochirality, in biological processes.

The CISS effect is also of fundamental scientific interest, as there is no theory fully explaining it yet. The variety of experiments reporting spin-polarization establishes that the CISS effect is present (and large) over a broad range of energies. Transport measurements probe the energies around the Fermi level, chemical reactions mostly depend on the alterations of the highest occupied molecular orbital/lowest unoccupied molecular orbital (HOMO/LUMO), and photoemission experiments probe energies above the vacuum level, thus up to 6 eV higher than the Fermi level. An all-encompassing theory explaining the CISS effect should work over this entire energy range.

The degree of spin polarization found in experiments cannot be quantitatively explained by spin orbit coupling alone because of the low mass of the atoms involved. In a simple model of helically arranged scattering centers, amplification of the spin-orbit terms due to constructive interference of the partial waves was proposed, but its quantitative effect on experiments is unclear [46]. Recent studies attempt to explain the CISS effect as intrinsically related to disorder that diminishes at low temperatures [47]. For a comprehensive review of experimental and theoretical studies and remaining open questions we refer to [48].

While photoemission experiments appear to be the most consistent way to measure CISS, only large-area ( $\approx 1 \text{ cm}^2$ ) averages of photoemission spin selectivity have been reported so far. The scanning probe experiments reported so far, however, show that there is a large site-dependent variability in the spin-polarization [38]. In fact, it is reasonable that the spin-polarization depends on the direct environment of the molecule, e.g. through ordering and (re-)orientation of the surrounding molecules, when we see CISS as a collective phenomenon of the layer, like Ray et al. concluded [34].

Hence, we will set out to use the imaging capabilities of the ESCHER (Electronic, Structural, and Chemical Nanoimaging in Real Time) setup, described in the next chapter, to acquire a two-dimensional map of the polarization-dependent photoelectron intensity. Our method should allow us to spot local differences and hence relate a possible CISS effect to local defects and/or other variations in the molecular layer structure. As we have no means of measuring spin directly in our ESCHER setup, we instead control the handedness of light and image the resulting photoemission intensity. The left/right circular polarization of the light leads to a non-zero spin polarization for the electrons photoemitted from the substrate. According to the studies by Ray et al. and Göhler et al. [36] we should expect an electron intensity difference between right and left circular light on the order of 10% after electrons pass through the molecular layer.

## 1.5 Outline of this thesis

In this thesis we will study elastic and inelastic interactions of electrons with van der Waals materials as well as the interaction of electron spins with organic molecules. In all cases, the energy of the probing electrons will be higher than the electron vacuum level. The latter energy, which we will generally refer to as the ‘zero’ energy in this thesis, lies above the Fermi level, the difference between both characteristic energies being the material’s work function.

The electron microscopy techniques used throughout this thesis are introduced in **Chapter 2**. Low energy electron microscopy (LEEM) and electron Volt-transmission electron microscopy (eV-TEM) will be utilized to measure the reflection and transmission of electrons in van der Waals materials. Photoemission electron microscopy (PEEM), especially with polarized light, will be used to investigate the CISS effect.

In **Chapter 3** we discuss the transmission and reflection of electrons on few-layer graphene. The elastic scattering processes, leading to resonances in the spectra discussed above, can be explained in a toy model based on interference [22]. However, there has been a debate on how to extract inelastic and elastic MFPs correctly from the low-energy reflection and transmission [49]. We extend the toy model to include inelastic contributions, and thus reconcile the elastic and inelastic view, and directly extract inelastic and elastic MFPs from that model.

The transmission and reflection from a heterostructure of hBN stacked on graphene is investigated in **Chapter 4**. The heterostructure breaks the up-down symmetry with respect to the direction of travel of the electrons. Thus, the effect of symmetry breaking on electron transmission and reflection is investigated and compared to *ab-initio* calculations and a modified toy model.

In **Chapter 5** we investigate few-layer molybdenum disulfide ( $\text{MoS}_2$ ), which has a more complicated out-of-plane structure than graphene (see Fig. 1.1). Connected to that geometric difference, we find distinct high-electron-transmissivity windows connected to the band structure. We compare the mean free paths obtained by our technique with those reported in previous photoemission studies.

**Chapter 6** is dedicated to the first steps in imaging polarization-dependent photoemission from chiral molecular layers using PEEM. We first report on photoemission measurements of plasmonic gold structures with linear polarized light. Then, we consider a film of chiral molecules (R-2,2'-bis(diphenylphosphino)-1,1'-binaphthyl, R-BINAP) for which we measure its photoemissivity upon illumination with left- and right-elliptically polarized light.

## References

- [1] A. Falin, Q. Cai, E.J.G. Santos, D. Scullion, D. Qian, R. Zhang, Z. Yang, S. Huang, K. Watanabe, T. Taniguchi, M.R. Barnett, Y. Chen, R.S. Ruoff, L.H. Li, Mechanical properties of atomically thin boron nitride and the role of interlayer interactions, *Nat. Commun.* 8 (2017) 1–9. <https://doi.org/10.1038/ncomms15815>.
- [2] Y. Yang, Z. Song, G. Lu, Q. Zhang, B. Zhang, B. Ni, C. Wang, X. Li, L. Gu, X. Xie, H. Gao, J. Lou, Intrinsic toughening and stable crack propagation in hexagonal boron nitride, *Nature* 594 (2021) 57–61. <https://doi.org/10.1038/s41586-021-03488-1>.
- [3] K. Cao, S. Feng, Y. Han, L. Gao, T. Hue Ly, Z. Xu, Y. Lu, Elastic straining of free-standing monolayer graphene, *Nat. Commun.* 11 (2020) 284. <https://doi.org/10.1038/s41467-019-14130-0>.
- [4] P.R. Wallace, The Band Theory of Graphite, *Phys. Rev.* 71 (1947) 622–634. <https://doi.org/10.1103/PhysRev.71.622>.
- [5] H. Min, B. Sahu, S.K. Banerjee, A.H. MacDonald, Ab initio theory of gate induced gaps in graphene bilayers, *Phys. Rev. B - Condens. Matter Mater. Phys.* 75 (2007) 1–7. <https://doi.org/10.1103/PhysRevB.75.155115>.
- [6] Y. Cao, V. Fatemi, S. Fang, K. Watanabe, T. Taniguchi, E. Kaxiras, P. Jarillo-Herrero, Unconventional superconductivity in magic-angle graphene superlattices, *Nature* 556 (2018) 43–50. <https://doi.org/10.1038/nature26160>.
- [7] S. Lisi, X. Lu, T. Benschop, T.A. de Jong, P. Stepanov, J.R. Duran, F. Margot, I. Cucchi, E. Cappelli, A. Hunter, A. Tamai, V. Kandyba, A. Giampietri, A. Barinov, J. Jobst, V. Stalman, M. Leeuwenhoek, K. Watanabe, T. Taniguchi, L. Rademaker, S.J. van der Molen, M.P. Allan, D.K. Efetov, F. Baumberger, Observation of flat bands in twisted bilayer graphene, *Nat. Phys.* 17 (2021) 189–193. <https://doi.org/10.1038/s41567-020-01041-x>.
- [8] E. Suárez Morell, J.D. Correa, P. Vargas, M. Pacheco, Z. Barticevic, Flat bands in slightly twisted bilayer graphene: Tight-binding calculations, *Phys. Rev. B* 82 (2010) 121407. <https://doi.org/10.1103/PhysRevB.82.121407>.
- [9] K.S. Novoselov, A.K. Geim, S. V. Morozov, D. Jiang, Y. Zhang, S. V. Dubonos, I.V. Grigorieva, A.A. Firsov, Electric Field Effect in Atomically Thin Carbon Films, *Science* (80-.). 306 (2004) 666–669. <https://doi.org/10.1126/science.1102896>.
- [10] J. Klein, M. Lorke, M. Florian, F. Sigger, L. Sigl, S. Rey, J. Wierzbowski, J. Cerne, K. Müller, E. Mitterreiter, P. Zimmermann, T. Taniguchi, K. Watanabe, U. Wurstbauer, M. Kaniber, M. Knap, R. Schmidt, J.J. Finley, A.W. Holleitner, Site-selectively generated photon emitters in monolayer MoS<sub>2</sub> via local helium ion irradiation, *Nat. Commun.* 10 (2019) 1–8. <https://doi.org/10.1038/s41467-019-10632-z>.
- [11] D. Geelen, A. Thete, O. Schaff, A. Kaiser, S.J. van der Molen, R. Tromp, eV-TEM: Transmission electron microscopy in a low energy cathode lens instrument, *Ultramicroscopy* 159 (2015) 482–487. <https://doi.org/10.1016/j.ultramic.2015.06.014>.

- [12] H. Hibino, S. Wang, C.M. Orofeo, H. Kageshima, Growth and low-energy electron microscopy characterizations of graphene and hexagonal boron nitride, *Prog. Cryst. Growth Charact. Mater.* 62 (2016) 155–176. <https://doi.org/10.1016/j.pcrysgrow.2016.04.008>.
- [13] H. Hibino, H. Kageshima, F. Maeda, M. Nagase, Y. Kobayashi, Y. Kobayashi, H. Yamaguchi, Thickness Determination of Graphene Layers Formed on SiC Using Low-Energy Electron Microscopy, *E-Journal Surf. Sci. Nanotechnol.* 6 (2008) 107–110. <https://doi.org/10.1380/ejsnt.2008.107>.
- [14] J. Jobst, J. Kautz, D. Geelen, R.M. Tromp, S.J. van der Molen, Nanoscale measurements of unoccupied band dispersion in few-layer graphene, *Nat. Commun.* 6 (2015) 8926. <https://doi.org/10.1038/ncomms9926>.
- [15] D.J. Griffiths, Time-Independent Schrödinger Equation, in: *Introd. to Quantum Mech.* ISBN 0131911759, 2nd ed., 2004.
- [16] K. Konishi, G. Paffuti, The Schrödinger equation, in: *Quantum Mech.*, Oxford University Press Oxford, 2009: pp. 49–88. <https://doi.org/10.1093/oso/9780199560264.003.0003>.
- [17] B. Stec, C. Jędrzejek, Resonance scattering by a double square-well potential, *Eur. J. Phys.* 11 (1990) 75–81. <https://doi.org/10.1088/0143-0807/11/2/002>.
- [18] V.U. Nazarov, E.E. Krasovskii, V.M. Silkin, Scattering resonances in two-dimensional crystals with application to graphene, *Phys. Rev. B - Condens. Matter Mater. Phys.* 87 (2013) 1–5. <https://doi.org/10.1103/PhysRevB.87.041405>.
- [19] K.D. Pham, H. V. Phuc, N.N. Hieu, B.D. Hoi, C. V. Nguyen, Electronic properties of GaSe/MoS<sub>2</sub> and GaS/MoSe<sub>2</sub> heterojunctions from first principles calculations, *AIP Adv.* 8 (2018). <https://doi.org/10.1063/1.5033348>.
- [20] M.P. Seah, W.A. Dench, Quantitative electron spectroscopy of surfaces: A standard data base for electron inelastic mean free paths in solids, *Surf. Interface Anal.* 1 (1979) 2–11. <https://doi.org/10.1002/sia.740010103>.
- [21] W.S.M. Werner, Questioning a Universal Law for Electron Attenuation, *Physics (College. Park. Md.)* 12 (2019) 93. <https://doi.org/10.1103/Physics.12.93>.
- [22] D. Geelen, J. Jobst, E.E. Krasovskii, S.J. van der Molen, R.M. Tromp, Nonuniversal Transverse Electron Mean Free Path through Few-layer Graphene, *Phys. Rev. Lett.* 123 (2019) 086802. <https://doi.org/10.1103/PhysRevLett.123.086802>.
- [23] P.S. Neu, D. Geelen, A. Thete, R.M. Tromp, S.J. van der Molen, Complementary LEEM and eV-TEM for imaging and spectroscopy, *Ultramicroscopy* 222 (2021) 113199. <https://doi.org/10.1016/j.ultramic.2020.113199>.
- [24] P.S. Neu, M. Šiškins, E.E. Krasovskii, R.M. Tromp, S.J. van der Molen, Electron transmission and mean free path in molybdenum disulfide at electron-volt energies, *Phys. Rev. B* 107 (2023) 075427. <https://doi.org/10.1103/PhysRevB.107.075427>.
- [25] Wikipedia: Circular polarization, (n.d.). [https://en.wikipedia.org/wiki/Circular\\_polarization](https://en.wikipedia.org/wiki/Circular_polarization) (accessed January 5, 2024).

- [26] M. Inaki, J. Liu, K. Matsuno, Cell chirality: Its origin and roles in left-right asymmetric development, *Philos. Trans. R. Soc. B Biol. Sci.* 371 (2016). <https://doi.org/10.1098/rstb.2015.0403>.
- [27] J.-B. Biot, Phénomènes de polarisation successive, observés dans des fluides homogènes, *Bull. Soc. Philomath* 190 (1815) 1815.
- [28] H.D. Flack, Louis Pasteur's discovery of molecular chirality and spontaneous resolution in 1848, together with a complete review of his crystallographic and chemical work, *Acta Crystallogr. Sect. A Found. Crystallogr.* 65 (2009) 371–389. <https://doi.org/10.1107/S0108767309024088>.
- [29] D. Lowe, Right Hand, Left Hand, Either Hand, (n.d.). <https://www.science.org/content/blog-post/right-hand-left-hand-either-hand> (accessed January 4, 2024).
- [30] T. Eriksson, S. Björkman, B. Roth, Å. Fyge, P. Höglund, Stereospecific determination, chiral inversion in vitro and pharmacokinetics in humans of the enantiomers of thalidomide, *Chirality* 7 (1995) 44–52. <https://doi.org/10.1002/chir.530070109>.
- [31] J.L. Bada, Origins of homochirality, *Nature* 374 (1995) 594–595. <https://doi.org/10.1038/374594a0>.
- [32] S.F. Ozturk, D.D. Sasselov, J.D. Sutherland, The central dogma of biological homochirality: How does chiral information propagate in a prebiotic network?, *J. Chem. Phys.* 159 (2023). <https://doi.org/10.1063/5.0156527>.
- [33] F.C. Frank, On spontaneous asymmetric synthesis, *Biochim. Biophys. Acta* 11 (1953) 459–463. [https://doi.org/10.1016/0006-3002\(53\)90082-1](https://doi.org/10.1016/0006-3002(53)90082-1).
- [34] K. Ray, S.P. Ananthavel, D.H. Waldeck, R. Naaman, Asymmetric scattering of polarized electrons by organized organic films of chiral molecules, *Science* (80-. ). 283 (1999) 814–816. <https://doi.org/10.1126/science.283.5403.814>.
- [35] F. Meier, D. Pescia, Band-Structure Investigation of Gold by Spin-Polarized Photoemission, *Phys. Rev. Lett.* 47 (1981) 374–377. <https://doi.org/10.1103/PhysRevLett.47.374>.
- [36] B. Göhler, V. Hamelbeck, T.Z. Markus, M. Kettner, G.F. Hanne, Z. Vager, R. Naaman, H. Zacharias, Spin selectivity in electron transmission through self-assembled monolayers of double-stranded DNA - Supplementary Information, *Science* (80-. ). 331 (2011) 894–897. <https://doi.org/10.1126/science.1199339>.
- [37] C. Clever, E. Wierzbinski, B.P. Bloom, Y. Lu, H.M. Grimm, S.R. Rao, W.S. Horne, D.H. Waldeck, Benchmarking Chiral Induced Spin Selectivity Measurements - Towards Meaningful Comparisons of Chiral Biomolecule Spin Polarizations, *Isr. J. Chem.* 62 (2022) 1–14. <https://doi.org/10.1002/ijch.202200045>.
- [38] Z. Xie, T.Z. Markus, S.R. Cohen, Z. Vager, R. Gutierrez, R. Naaman, Spin specific electron conduction through DNA oligomers, *Nano Lett.* 11 (2011) 4652–4655. <https://doi.org/10.1021/nl2021637>.

- [39] M. Suda, Y. Thathong, V. Promarak, H. Kojima, M. Nakamura, T. Shiraogawa, M. Ehara, H.M. Yamamoto, Light-driven molecular switch for reconfigurable spin filters, *Nat. Commun.* 10 (2019) 2455. <https://doi.org/10.1038/s41467-019-10423-6>.
- [40] A.K. Mondal, M.D. Preuss, M.L. Ślęczkowski, T.K. Das, G. Vantomme, E.W. Meijer, R. Naaman, Spin Filtering in Supramolecular Polymers Assembled from Achiral Monomers Mediated by Chiral Solvents, *J. Am. Chem. Soc.* 143 (2021) 7189–7195. <https://doi.org/10.1021/jacs.1c02983>.
- [41] T. Liu, X. Wang, H. Wang, G. Shi, F. Gao, H. Feng, H. Deng, L. Hu, E. Lochner, P. Schlottmann, S. Von Molnár, Y. Li, J. Zhao, P. Xiong, Linear and nonlinear two-terminal spin-valve effect from chirality-induced spin selectivity, *ACS Nano* 14 (2020) 15983–15991. <https://doi.org/10.1021/acsnano.0c07438>.
- [42] W. Zhang, K. Banerjee-Ghosh, F. Tassinari, R. Naaman, Enhanced Electrochemical Water Splitting with Chiral Molecule-Coated Fe<sub>3</sub>O<sub>4</sub> Nanoparticles, *ACS Energy Lett.* 3 (2018) 2308–2313. <https://doi.org/10.1021/acsenergylett.8b01454>.
- [43] P.K. Bhartiya, M. Srivastava, D. Mishra, Chiral-induced enhanced electrocatalytic behaviour of cysteine coated bifunctional Au–Ni bilayer thin film device for water splitting application, *Int. J. Hydrogen Energy* 47 (2022) 42160–42170. <https://doi.org/10.1016/j.ijhydene.2021.08.219>.
- [44] K.B. Ghosh, W. Zhang, F. Tassinari, Y. Mastai, O. Lidor-Shalev, R. Naaman, P. Möllers, D. Nürenberg, H. Zacharias, J. Wei, E. Wierzbinski, D.H. Waldeck, Controlling Chemical Selectivity in Electrocatalysis with Chiral CuO-Coated Electrodes, *J. Phys. Chem. C* 123 (2019) 3024–3031. <https://doi.org/10.1021/acs.jpcc.8b12027>.
- [45] X. Yang, C.H. van der Wal, B.J. van Wees, Detecting Chirality in Two-Terminal Electronic Nanodevices, *Nano Lett.* 20 (2020) 6148–6154. <https://doi.org/10.1021/acs.nanolett.0c02417>.
- [46] J.M. van Ruitenbeek, R. Korytár, F. Evers, Chirality-controlled spin scattering through quantum interference, *J. Chem. Phys.* 159 (2023). <https://doi.org/10.1063/5.0156316>.
- [47] T.K. Das, F. Tassinari, R. Naaman, J. Fransson, Temperature-Dependent Chiral-Induced Spin Selectivity Effect: Experiments and Theory, *J. Phys. Chem. C* 126 (2022) 3257–3264. <https://doi.org/10.1021/acs.jpcc.1c10550>.
- [48] F. Evers, A. Aharony, N. Bar-Gill, O. Entin-Wohlman, P. Hedegård, O. Hod, P. Jelinek, G. Kamieniarz, M. Lemeshko, K. Michaeli, V. Mujica, R. Naaman, Y. Paltiel, S. Refaely-Abramson, O. Tal, J. Thijssen, M. Thoss, J.M. van Ruitenbeek, L. Venkataraman, D.H. Waldeck, B. Yan, L. Kronik, Theory of Chirality Induced Spin Selectivity: Progress and Challenges, *Adv. Mater.* 34 (2022) 1–11. <https://doi.org/10.1002/adma.202106629>.
- [49] L.H. Yang, B. Da, H. Yoshikawa, S. Tanuma, J. Hu, J.W. Liu, D.M. Tang, Z.J. Ding, Low-energy electron inelastic mean free path and elastic mean free path of graphene, *Appl. Phys. Lett.* 118 (2021) 053104. <https://doi.org/10.1063/5.0029133>.

# 2 LOW-ENERGY ELECTRONS: MICROSCOPY AND SPECTROSCOPY



## 2.1 Introduction

The work in this thesis is built on three electron microscopy techniques, namely low energy electron microscopy (LEEM), electron-volt transmission electron microscopy (eV-TEM) and photoemission electron microscopy (PEEM). In contrast to other types of electron microscopy, these three techniques are based on low-energy electrons with energies in the 0-50 eV range. When low-energy electrons are incident on a sample, their interaction with the sample reveals information about the electronic band structure of the sample as outlined in Chapter 1. As the mean free path (MFP) of low-energy electrons is short, they are most sensitive to the surface. In the case of low-energy electron transmission microscopy (eV-TEM), the electrons traverse the full thickness of the sample, but the sample can only be a few atoms thick as low-energy electrons do not penetrate bulk samples to a measurable amount. In photoemission microscopy (PEEM), electrons from an occupied band are excited to the vacuum by illumination with ultraviolet (UV) light, also yielding low-energy electrons.

Electron microscopy means mapping the electronic properties of a sample with spatial resolution. In comparison to optical microscopy, an electron microscope is not limited by the wavelength of light, but by the de Broglie wavelength of the electron, thus LEEM reaches a resolution of 1.4 nm [1]. Still, the construction of the electron microscope can be understood from the analogy to optical microscopes, with electric and magnetic fields taking the place of mirrors and lenses [2,3]. The discovery of this analogy started the field of electron-optics and paved the way for building electron microscopes [4,5]. Like in an optical microscope, the electron microscope is constructed to have intermediate planes that form an image, referred to as the image plane, and back focal planes, referred to as the diffraction- or momentum plane in electron optics. Unlike in optics, the electron lenses can be adjusted in focal length or switched off by changing the voltage/current. This way the operator can change the magnification or switch between real-space and momentum space.

## 2.2 The ESCHER setup

The electron sources and contrast mechanisms in the different methods employed (LEEM, eV-TEM, PEEM) in this thesis are various but share one feature: In all cases, the collected electrons have a small, well-defined energy in the order of 0-50 eV. This enables the use of the same electron-optics in all three techniques for imaging, filtering, and projecting the electrons, to form an image of the sample. Figure 2.1a shows the sketch of such an instrument, the ESCHER aberration-corrected Low-energy Electron Microscope used for the work in this thesis. The sketch shows the different imaging techniques used and the different electron sources for LEEM (black), eV-TEM (green), and PEEM (violet arrow, UV light). The path of the electrons after leaving the sample (shown in red) is the same for the different techniques. The whole setup is under ultra-high vacuum (UHV), with the lowest pressure below  $10^{-9}$  mbar in the sample chamber to avoid contamination of the sample surface.

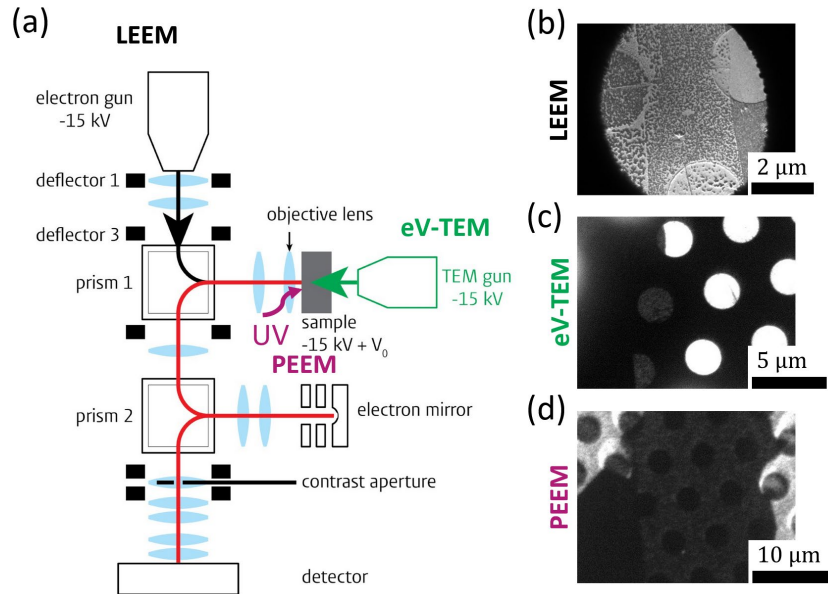


Figure 2.1: Different electron microscopy techniques in the ESCHER low energy electron microscopy setup. (a) Simplified sketch of the setup geometry with the electron sources in LEEM (black), eV-TEM (green) and the UV light for PEEM (violet). After interacting with the sample, all electrons take the same path (red) to the detector. Images of the same MoS<sub>2</sub> flake on a TEM grid recorded with LEEM (b), eV-TEM (c), and PEEM (d).

## 2.3 Low-energy Electron Microscopy (LEEM)

Foremost, the ESCHER setup was built as a Low-energy Electron Microscope aiming for improved real-space resolution. In LEEM mode, the electrons are emitted from a field emission gun at a potential of -15 kV at the top of the instrument (black in Figure 2.1a). The path of the electron is adjusted by deflector 1 (mostly in-plane momentum) and deflector 3 (mostly real-space position). The electrons are then directed toward the sample by the Lorentz force generated by a magnetic field that is oriented out of the plane of the sketch. This element, called the (magnetic) prism, is necessary to split the incoming and reflected electron beam.

The electrons travel through the objective lens, which is an electromagnetic lens. Between the objective lens kept at ground potential and the sample kept at  $-15 \text{ kV} + V_0$  the electrons are decelerated to an energy of  $E_0 = V_0 \cdot e$ , with the energy tunable through the voltage  $V_0$ . We remind ourselves that electric fields are conservative, thus the energy of the electron when interacting with the sample is only determined by the potential difference between the initial gun potential and the sample potential. As explained in Chapter 1, the electrons interact with the sample and are partially reflected, yielding the contrast in LEEM. The contrast strongly depends on the electron energy.

By convention, the energy reference  $E_0 = 0 \text{ eV}$  is set to the point where the electrons just hit the sample, called the mirror mode transition. Thus, at  $E_0 = 0 \text{ eV}$  the vacuum levels of the electron gun and the sample are aligned (whereas setting the same voltages would align the Fermi levels). The excitation of the objective lens is used to focus the electrons.

At LEEM low energies of 0-50 eV the reflection is dominated by elastically backscattered electrons, as inelastic processes, e.g., excitations of phonons and plasmons, only increase with increasing energy. When imaging in momentum space, we see these backscattered electrons as the specular spot. The first-order diffraction spots, that reveal the (inverse) lattice structure of a crystalline material, are visible at higher energies (typically  $> 25$  eV), when the electron energy is sufficient to be converted to an in-plane momentum that matches the Bragg condition.

We note that, unlike in a scanning transmission electron microscope (STEM) or a scanning electron microscope (SEM), the electron beam (seen as the bright area in Figure 2.1b) hits an area of about  $7 \mu\text{m}$  diameter of the sample all at once, like the in-line illumination in an optical wide-field microscope as opposed to a confocal microscope. The image is later created by projecting the reflected part of this beam on a two-dimensional screen. This enables imaging in real-time without scanning the electron beam.

After reflection, the electrons are accelerated by the electric field between the sample and the objective lens and travel through the magnetic prism. As the electrons now travel in the opposite direction, the Lorentz force directs them to the bottom, where the electrostatic transfer lens is situated. As the name prism suggests, the magnetic field also disperses the electrons of different energies, providing a means to resolve and filter electron energies.

The second prism and the electrostatic mirror are specific to the aberration-corrected LEEM setup. While other LEEM setups do without this part, it improves the resolution by correcting spherical aberrations to third order and chromatic aberrations to second rank. The voltages on the three mirror plates are tuned alongside the sample voltage for best correction at  $V_0$ . The electrons reflect from the 15 keV equipotential line without ever physically hitting the metal mirror plates. Again, the reflected electrons travel through the second prism and are deflected to the bottom.

The contrast aperture (below the second prism, see Fig. 2.1a) is placed in a diffraction-plane of the instrument to allow for filtering by placing an aperture in the beam path. The contrast aperture is placed around the specular spot (bright field) while looking at the sample in momentum-space. Then one can switch to the real-space image created with only the electrons that passed the contrast aperture, i.e., the electrons filtered in momentum space. The following four lenses, forming the projector column, are used to switch between real- and momentum-space and to magnify the image before the electrons hit the detector. The detector consists of a channel plate with variable gain and a fluorescent screen, that lights up when hit by electrons. The optical image on the fluorescent screen is then filmed with a CCD camera.

To record a LEEM IV (intensity as a function of voltage) spectrum, the electron energy  $E_0$  is varied (typically in steps of 0.1 eV), and an image is recorded at every energy. As the intensity of a spectrum can vary over multiple orders of magnitude, the gain of the channel plate is automatically adjusted for adequate exposure. From this stack of images, the spectra of different sample areas are extracted and normalized by the calibrated channel plate gain curve [6]. We also record images at an energy where all electrons are reflected before reaching the sample (mirror mode,  $E_0 < 0$ ) to normalize the reflection spectrum to the incident electron flux.

## 2.4 Electron Volt-Transmission Electron Microscopy (eV-TEM)

In eV-TEM, the electrons are emitted from a second electron gun added on the other side of the sample [7]. The electrons reach the sample at a tunable energy  $E_0$ , are partially transmitted, and then take the same path as the LEEM electrons would after reflection. Switching either the LEEM electron gun or the eV-TEM gun on, allows for consecutive imaging of the same sample area with both techniques, as both techniques use the same electron optical path for imaging the reflected and transmitted electrons, respectively. We will use eV-TEM in conjunction with LEEM to extract the elastic and inelastic MFP and identify states in the band structure. The LEEM image of a MoS<sub>2</sub> flake and the same area imaged in eV-TEM are shown in Figures 2.1b and c. The transmission spectra can be normalized to the flux passing an uncovered hole in the TEM grid at high energy.

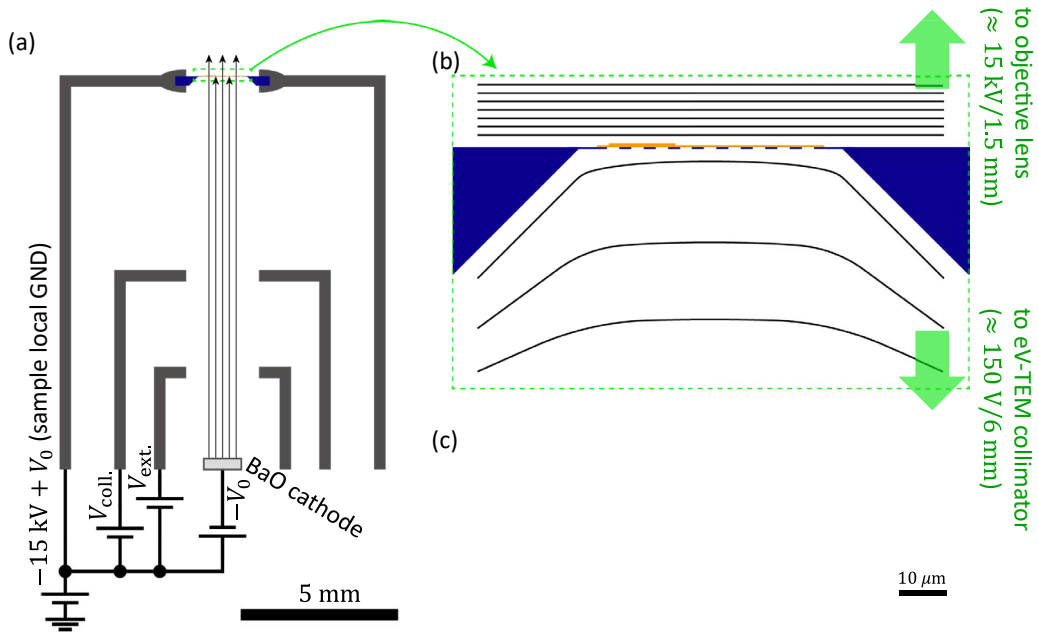


Figure 2.2: Geometry and electrical setup of the eV-TEM electron gun. (a) shows a cut through the cylindrically symmetric apertures used to guide the electrons emitted from a heated barium oxide (BaO) cathode to the sample. The equipotential lines (black lines in b) are curved close to the sample on a TEM grid, placed on top of the eV-TEM gun. The samples for eV-TEM are prepared on a silicon nitride TEM grid with a grid of holes (2.5 μm diameter) shown in c (purchased from Ted Pella, who also provided the SEM images in c).

The eV-TEM gun, which is integrated into the sample holder, is shown in more detail in Figure 2.2 together with its electrical setup. Figure 2.2a shows a cut through the electron gun, which is cylindrically symmetric around the electron beam axis. The electron gun consists of a barium oxide emitter, two apertures that act as electrostatic lenses, and the sample that is clamped onto the top. The eV-TEM gun is designed to fit in a modified sample holder [8], thus constrained to a diameter of about 1 cm and the use of 5 high-voltage electrical connections. The electron emitter is a barium oxide cathode (BaO, Kimball Physics), that thermally emits electrons when a current is passed through it and an extraction voltage  $V_{ext.} \approx 50 \text{ eV}$  is applied. The barium oxide emitter is kept at a voltage of  $-15 \text{ kV} - \Phi_{BaO}/e$  (the voltage equivalent to the work

function of BaO  $\Phi_{BaO}$ ), such that the electrons travel through the prisms at 15 keV like the electrons in LEEM mode.

After passing the extractor, the electron beam is collimated (i.e., reshaped to hit the sample as perpendicularly as possible) by the collimation voltage of  $V_{coll.} \approx 150$  eV and finally reaches the sample at an energy of  $e \cdot V_0$  with the sample voltage tuned to  $V_{sample} = -15$  kV +  $V_0$ . The electrons transmitted through the sample are then accelerated to the objective lens and enter the imaging electron-optics just like the LEEM electrons after reflection. In eV-TEM mode, the electron bundle illuminates the whole sample, such that large overview images can be recorded in real-time.

The power supplies that provide the voltages  $-V_0$ ,  $V_{ext.}$  and  $V_{coll.}$  and the heating current supply for the BaO cathode are referenced to the sample voltage  $V_{sample} = -15$  kV +  $V_0$  as shown in the circuit diagram in Figure 2.2a. This way the operation in LEEM mode remains unaffected when the eV-TEM gun is turned off and no additional high-voltage power supplies are needed for eV-TEM. In eV-TEM mode, one has to take care that both the sample voltage and the cathode voltage are adjusted in parallel, to keep the absolute potential of the BaO cathode – thus the energy of the eV-TEM in the prism – constant. The eV-TEM gun is turned off by setting the BaO cathode to a positive voltage, such that no eV-TEM electrons reach the sample, while keeping the cathode heated.

The eV-TEM samples, typically few-layer van der Waals materials, are prepared on a holey silicon nitride ( $Si_3N_4$ ) TEM grid (PELCO®) purchased from Ted Pella. The TEM grid consists of a round carrier chip (3 mm diameter, 200  $\mu$ m thick), that thins down to a 200 nm thin membrane (500  $\mu$ m x 500  $\mu$ m wide) in the center (see Fig. 2.2c) and has an array of holes (typically 2.5  $\mu$ m diameter) patterned into the membrane. While the 80 nm  $Si_3N_4$  membrane is transparent enough to high-energy TEM, it is not transparent for low-energy electrons. We coat the  $Si_3N_4$  TEM grid in 5 nm platinum/palladium from both sides with a sputter coater (Cressington 208HR) to make it conductive. Then the layered materials are transferred onto the top, flat surface of the TEM grid.

The TEM grid with a layered sample is sketched in Figure 2.2b. As the TEM grid is surrounded by large electric fields, the sample itself must be considered part of the electron optics. The equipotential lines around the sample are sketched in Figure 2.2b. As the sample is usually oriented with the flat side – not the recessed side – towards the objective lens, the equipotential lines on that side are as flat as when imagining a typical sample in LEEM mode, e.g., a silicon chip with graphene on top. On the back side of the TEM grid, the equipotential lines follow the recessed shape of the TEM grid, obstructing imaging with electrons at perpendicular incidence at the edge of the recessed membrane. However, as the membrane is 500  $\mu$ m wide and recessed with a 45-degree slope, and the electric field on the eV-TEM is comparably weak ( $\approx 150$  V/6 mm toward the collimator), the arising deflection of the electrons is weak on most of the grid. We will remark on the problems when flipping the TEM grid, thus putting the recessed side towards the objective lens where the voltage gradient is much stronger, in Chapter 4.

The energy resolution of the eV-TEM spectra is limited to  $\approx 0.8$  eV given by the energy spread of the thermally emitted electrons from the BaO cathode, while the cold field emitter of the

LEEM gun reaches an energy resolution of  $\approx 0.3$  eV. An improved electron gun, that uses a field emitter to reach the same energy resolution as in LEEM, was designed by Zhiyuan Cheng [9] as a M.Sc. student in our group but has not been produced yet.

## 2.5 Photoemission Electron Microscopy (PEEM) with polarized light

In photoemission electron microscopy ultraviolet light is shone on the sample and the electrons are emitted from the sample due to the photoelectric effect. The photon energy associated with the (deep) ultraviolet (UV) wavelength of the light must be sufficient to excite an electron from the highest occupied band to the (lowest band above the) vacuum level. The contrast is created by the different photoemissivity and work function in the material (and possible contamination). The electrons that overcome the work function barrier and leave the material are then accelerated toward the objective lens. As the photon energy used is typically just sufficient to reach the vacuum, the photoemitted electrons have a low energy of a few eV (and an even lower energy spread) and can thus be imaged by the same electron optics used for LEEM. The chirality induced spin selectivity effect is reported to manifest itself in a photoemission intensity depending on the polarization of the light (see Chapter 1). We add polarization control to PEEM to enable imaging this polarization-dependent contrast and thus spatially resolving the CISS effect.

Generally, the ESCHER setup is equipped with a mercury-vapor lamp filtered to emit a 254 nm wavelength (equivalent to 4.9 eV photon energy) for PEEM imaging [11]. While this photon energy is sufficient for photoemission from most materials, it may not be enough to overcome the work function of clean gold reported as 5.1 to 5.5 eV [12,13]. To reach this energy and match the setup used in previous photoemission experiments on chiral molecules, we installed a laser with 224 nm wavelength (equivalent to 5.5 eV photon energy). This deep UV (DUV) laser we use (PhotonSystems, HeAg70) is a pulsed laser. The pulse width is long (100  $\mu$ s) and the power per pulse is low enough (14  $\mu$ J and 160 mW peak power) to not heat the sample or cause space charge effects. The maximum repetition rate is 20 Hz. The laser pulses are synchronized to the CCD camera trigger, such that every exposure contains exactly one pulse.

The use of a collimated laser beam also allows for control of the polarization, as needed for the photoemission experiments on chiral molecules with circularly polarized light, discussed in Chapter 6. The polarization control setup used to create circularly polarized light is shown in Figure 2.3, together with a schematic sketch of the optical components. The setup is clamped on the outside of the vacuum chamber of the ESCHER setup to a fused silica viewport facing the sample. The laser beam is aligned to the sample and the middle of the viewport with an adjustable mirror (DUV mirror, 190-600 nm enhanced aluminum coating, not in the photo Figure 2.3a).

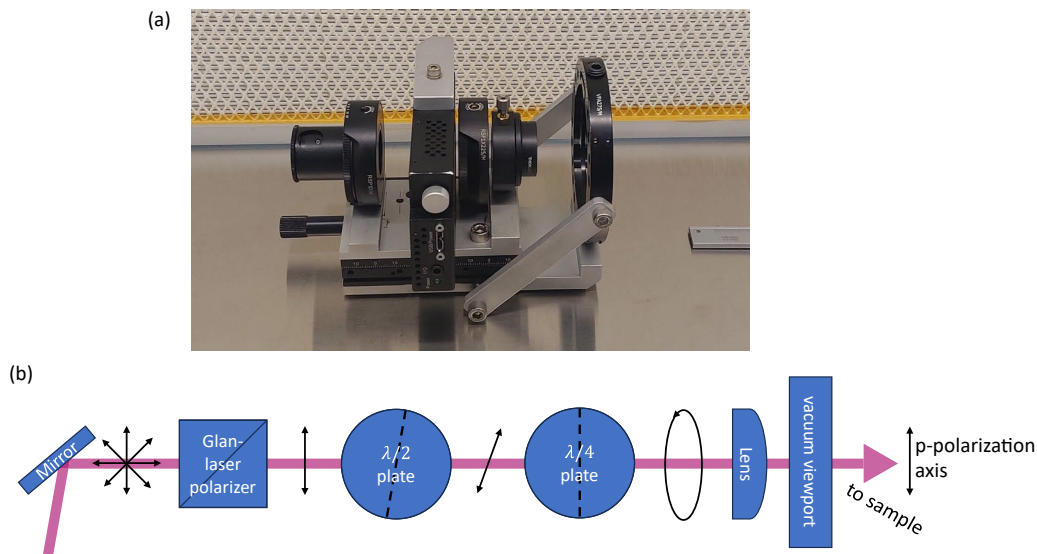


Figure 2.3: Polarization control setup for the polarization-dependent photoemission experiments. The polarizer, the motorized  $\lambda/2$  plate, the  $\lambda/4$  plate, and the lens are mounted on a bracket (photo a), that attaches to the sample vacuum chamber. The polarization of the light after each optical element is sketched with black arrows in b.

After reflecting from the mirror, the light passes the linear polarizer (a polarizing prism beam splitter, Glan Taylor prism). In the ESCHER setup, the laser beam is not perpendicularly incident on the sample, as the (electron-) objective lens is in that place. Therefore, two inequivalent linear polarization directions are defined relative to the plane spanned by the laser beam incident on the sample and its reflection, named p-polarization (that is parallel to that plane) and s-polarization (that is perpendicular to that plane). The polarizer is aligned to the s-polarization direction, where the absorption of light (and therefore the photoemission) is minimal. Then the linearly polarized light passes a  $\lambda/2$  retardation plate, which changes the direction of the linear polarization. This  $\lambda/2$  plate is mounted on a computer-controlled motorized stage. This setup has been used for experiments with linear polarized light of varying orientations.

For experiments with circularly polarized light, a  $\lambda/4$  plate is added after the  $\lambda/2$  plate. The fast axis of the  $\lambda/4$  plate is aligned with the s-polarization direction, as the axes of the  $\lambda/4$  plate define the short and long axis of elliptically polarized light, which should be symmetric with the s-polarization direction. Finally, a plano-convex lens ( $f=175$  mm) is added, to focus the laser beam on the sample and thus increase the local light (and thus photoemission) intensity. While all the polarization control is mounted out-of-vacuum, the laser beam enters the vacuum through a fused silica viewport.

The typical experiment consists of acquiring images in one position of the motorized  $\lambda/4$  plate, rotating the  $\lambda/4$  plate to the angle mirrored along the s-polarization direction, and acquiring images again. As the intensity is low (shot noise and laser intensity pulse noise is the main source of error), this process is repeated 100 or 200 times. Then the difference between the images in each position gives insight into the (breaking of) symmetry.

## References

- [1] S.M. Schramm, Image Formation in LEEM and PEEM, in: PhD Thesis Imaging with Aberration-Corrected Low Energy Electron Microsc., Casimir PhD series, Leiden, NL, 2013. <https://hdl.handle.net/1887/20843>.
- [2] H. Busch, Berechnung der Bahn von Kathodenstrahlen im axialsymmetrischen elektromagnetischen Felde, *Ann. Phys.* 386 (1926) 974–993. <https://doi.org/10.1002/andp.19263862507>.
- [3] E. Brüche, H. Johannson, Elektronenoptik und Elektronenmikroskop, *Naturwissenschaften* 20 (1932) 353–358. <https://doi.org/10.1007/BF01504926>.
- [4] M. Knoll, E. Ruska, Beitrag zur geometrischen Elektronenoptik. I, *Ann. Phys.* 404 (1932) 607–640. <https://doi.org/10.1002/andp.19324040506>.
- [5] E. Bauer, Introduction: History, in: *Surf. Microsc. with Low Energy Electrons*, Springer New York, New York, NY, 2014: pp. 1–19. [https://doi.org/10.1007/978-1-4939-0935-3\\_1](https://doi.org/10.1007/978-1-4939-0935-3_1).
- [6] T.A. de Jong, D.N.L. Kok, A.J.H. van der Torren, H. Schopmans, R.M. Tromp, S.J. van der Molen, J. Jobst, Quantitative analysis of spectroscopic low energy electron microscopy data: High-dynamic range imaging, drift correction and cluster analysis, *Ultramicroscopy* 213 (2020) 112913. <https://doi.org/10.1016/j.ultramic.2019.112913>.
- [7] D. Geelen, eV-TEM: Transmission Electron Microscopy with Few-eV Electrons, Doctoral dissertation, Leiden University, 2018. <http://hdl.handle.net/1887/63484>.
- [8] D. Geelen, A. Thete, O. Schaff, A. Kaiser, S.J. van der Molen, R. Tromp, eV-TEM: Transmission electron microscopy in a low energy cathode lens instrument, *Ultramicroscopy* 159 (2015) 482–487. <https://doi.org/10.1016/j.ultramic.2015.06.014>.
- [9] Z. Cheng, Designing a Novel eV-TEM Gun in COMSOL, 2022. <https://hdl.handle.net/1887/3453471>.
- [10] R.M. Tromp, J.B. Hannon, A.W. Ellis, W. Wan, A. Berghaus, O. Schaff, A new aberration-corrected, energy-filtered LEEM/PEEM instrument. I. Principles and design, *Ultramicroscopy* 110 (2010) 852–861. <https://doi.org/10.1016/j.ultramic.2010.03.005>.
- [11] R.M. Tromp, J.B. Hannon, W. Wan, A. Berghaus, O. Schaff, A new aberration-corrected, energy-filtered LEEM/PEEM instrument II. Operation and results, *Ultramicroscopy* 127 (2013) 25–39. <https://doi.org/10.1016/j.ultramic.2012.07.016>.
- [12] W.M. Haynes, *CRC Handbook of Chemistry and Physics*, CRC Press, 2014. <https://doi.org/10.1201/b17118>.
- [13] W.M.H. Sachtler, G.J.H. Dorgelo, A.A. Holscher, The work function of gold, *Surf. Sci.* 5 (1966) 221–229. [https://doi.org/10.1016/0039-6028\(66\)90083-5](https://doi.org/10.1016/0039-6028(66)90083-5).





# 3 EXTRACTING TRANSVERSE ELECTRON MEAN FREE PATHS IN GRAPHENE AT LOW ENERGY

## Abstract

The LEEM-IV spectra of few-layer graphene show characteristic minima at specific energies, which depend on the number of graphene layers. For the same samples, low-energy TEM (eV-TEM) spectra exhibit transmission maxima at energies corresponding to those of the reflection minima in LEEM. Both features can be understood from interferences of the electron wave function in a purely elastic model. Inelastic scattering processes in turn lead to a finite, energy-dependent inelastic Mean Free Path (MFP) and a lower finesse of the interference features. Here we develop a model that introduces both an elastic and inelastic scattering parameter on the wave-function level, thus reconciling the models considered previously. Fitting to published data, we extract the elastic and inelastic MFP self-consistently and compare these to recent reports.

### 3.1 Introduction

The (inelastic) electron Mean Free Path (MFP) is a material-specific quantity describing the mean distance of free travel by an electron until it scatters (inelastically). In the case of a bulk material and an electron incident from vacuum, one can to first approximation expect an exponential decay of the electron flux with increasing thickness. The MFP with respect to energy was generally found to follow a U-shape curve in a broad selection of materials [1]. This so-called universal curve [2] runs over a large energy range, up to  $10^6$  eV, and has a single minimum around 30-50 eV. However, recent studies of 2D materials, foremost graphene, have shown additional features to the energy-dependent MFP curve, especially at low energies where the electron wavelength is on the order of the lattice spacings [3–6]. An increasing interest in properties and applications of (heterostructures of) 2D materials, as well as in inelastic interaction of low-energy electrons with nanolayers, calls for a consistent description of scattering effects in these quantum systems.

Recently, experimental reflectivity and transmissivity data on 1-4 layers of graphene have been published by Geelen et al. [3]. In that study, low energy electron microscopy (LEEM) was used to obtain reflection spectra  $R(E)$ , while electron-Volt transmission electron microscopy (eV-TEM) was introduced to obtain transmission curves  $T(E)$  (see Fig. 3.1a). Here,  $E$  denotes the electron energy with respect to the vacuum energy, defined as  $E_{\text{vac}} = 0$ . For multilayers (two or more atomic layers) of graphene, both  $R(E)$  and  $T(E)$  curves revealed interference effects, thus calling for a wave-based scattering model. From the difference between unity and the sum of reflection and transmission, inelastic scattering effects were quantified. Thus, the authors determined the inelastic MFP (IMFP) as a function of energy, directly from reflectivity and transmissivity spectra. More recently, Yang et al. [7] argued against the methodology chosen by Geelen et al. to determine the IMFP and re-analyzed the experimental data using an alternative method. Specifically, they applied a correction factor to take into account the zig-zag path the electron travels between multiple reflections. Within their analysis, they conclude that a  $\pi + \sigma$  plasmon in multilayer graphene is discernible in Geelen et al.'s data. This  $\pi + \sigma$  plasmon cannot be excited in the monolayer [8].

The jellium-like model used by Yang et al. has clear advantages with respect to the method Geelen et al. used. Specifically, the statistical average of the path travelled by an electron until it randomly scatters inelastically was developed in their model. Fundamental to the jellium-like model, however, is that it cannot account for the interference effects [9] that are characteristic of the multilayer graphene system.

Here we introduce an improved method to reconcile these two previous models. Our approach is to keep the notion of discrete graphene layers intact while incorporating an inelastic loss factor that relates to the zig-zag path travelled by the electron between graphene layers. By fitting this model to the data published in reference [3], we extract the inelastic MFP and a reflection coefficient of the electron wave function in a one-step process. We also discuss whether the  $\pi + \sigma$  plasmon can indeed be extracted from the data available.

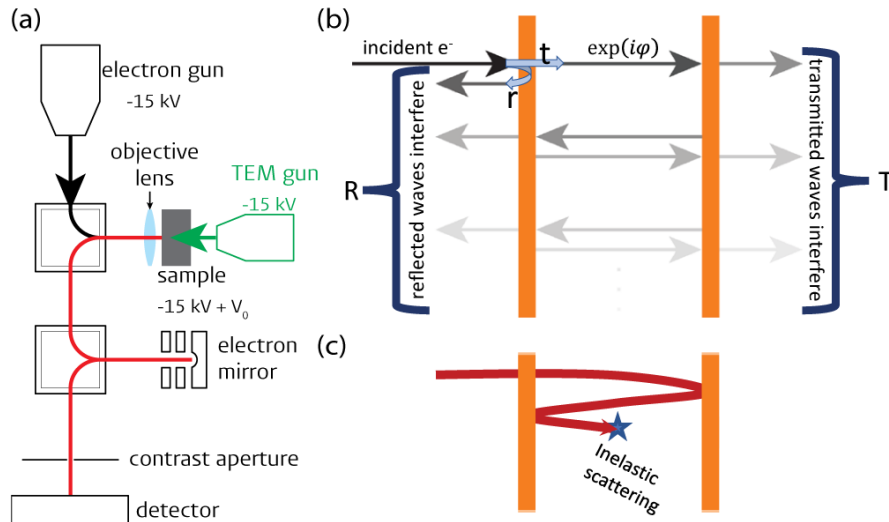


Figure 3.1: (a) sketches the LEEM setup, with the path of the incident electrons in LEEM mode (black) and in eV-TEM mode (green). After reflection/transmission from the sample the electrons follow the red path to the detector. (b) Illustration of the electron paths through two layers of graphene upon multiple partial reflections and transmissions. Between the layers, the electron wave gains a phase  $\varphi$ . (c) One classical electron trajectory (red path). After travelling some distance (on average: the inelastic Mean Free Path (IMFP)), an inelastic scattering process happens. Experimentally, this means that the electron is not detected in reflection nor transmission. Analysis of the IMFP is required to take into account such ‘zig-zag paths’ [7], which may be significantly longer than the thickness of the material.

### 3.2 Interference model with losses

To obtain some intuition for the problem, we will first consider single-layer graphene. Along the propagation direction of the electron, perpendicular to the atomic plane, the scattering problem then resembles a well-known quantum-mechanics exercise: calculating the (unbound) states of a one-dimensional potential well [10]. The extension of this calculation to multiple wells equivalent to multiple graphene layers can then be done by a transfer matrix approach [11]. Further simplifying this model, one can compare each graphene layer to a partially transparent mirror in an optical Fabry-Pérot experiment [12], leading to a series of resonances as a function of wavelength and hence energy. Fig. 3.1b illustrates the partial reflection (transmission) of the electron wave incident upon a graphene layer (orange plane) with reflection and transmission coefficients  $r$  and  $t$ . As there is no cutoff to the number of partial reflections, the reflected/transmitted flux is the absolute square of an infinite sum of interfering waves. Conservation of flux at the layer requires  $r^2 + t^2 = 1$ , with  $r, t < 1$ . Note that in the experiment by Geelen et al. (see sketch Fig. 3.1a) the electron beams incident on the graphene from either side were aligned perpendicularly to the sample and a contrast aperture was inserted to block electrons that lost energy or were scattered off-axis.

Generally, interference effects will depend on electron energy via the de Broglie electron wavelength. At wavelengths for which interferences are constructive in the forward direction, transmission maxima will be found. Thus, the so-called interference ‘toy-model’ introduced by

Geelen et al. provides a basic explanation for the presence of transmission peaks and (accompanying) reflection minima in the experimental curves, which occur around 3 eV and 18 eV (see Fig. 3.3).

For our discussion, we first need to consider this toy-model in more detail. The phase propagation over a distance equal to the layer spacing  $a$  is given by:

$$\varphi = a \cdot \sqrt{\frac{2m_e}{\hbar^2} (E + \Phi)}, \quad \text{eq. 1}$$

where  $E$  is the incident electron energy (with respect to the vacuum level) and  $\Phi = 4.6$  eV (which is close to the work function),  $m_e$  the free electron mass and  $\hbar$  the reduced Planck constant [13]. The quantum mechanical reflectivity and transmissivity coefficients of  $n$  layers (see supplemental material in [3]) yield the following recursive formulas:

$$t_n = \left[ \frac{t \cdot t_{n-1} e^{i\varphi}}{1 + r \cdot r_{n-1} e^{2i\varphi}} \right] \quad \text{eq. 2a}$$

$$r_n = \left[ r + \frac{t^2 \cdot r_{n-1} e^{2i\varphi}}{1 + r \cdot r_{n-1} e^{2i\varphi}} \right] \quad \text{eq. 2b}$$

with  $r$  and  $t$  the wave reflection and transmission coefficients for a single layer within the structure. Obviously, for the case of single layer graphene,  $r_1 = r$  and  $t_1 = t$ , respectively. The measured electron intensities for  $n$  layers of graphene are finally obtained by taking the absolute square of the wave function,  $T_n = |t_n|^2$  and  $R_n = |r_n|^2$ .

However, the formulas used by Geelen et al. to extract the total and inelastic MFP (eq. 1 and 2 in [3]) were not linked to this toy-model. Rather, the authors chose a more macroscopic picture. As Yang et al. criticize, eq. 1 and 2 in [3] combined imply that both the transmitted and reflected electrons travel a distance equal to the sample thickness  $d$  through the material, which is a reasonable assumption for the transmitted electrons but not for the reflected electrons. Furthermore, we point out that equation 2 in [3], reading  $T + R = \exp(-d/\lambda_{\text{inel}})$  cannot hold for bulk, as it implies that no electrons are transmitted nor reflected, while LEEM experiments show that there is reflection from bulk samples (in fact several nanometers of thickness can be considered as bulk: after that the reflectivity barely changes, possibly being as large as 50%, e.g., in graphene on silicon carbide [13]).

Yang et al. also emphasize that the path travelled by an electron may be much larger than the material thickness, as the partial reflection and transmission leads to zig-zag paths (see Fig. 3.1c for an example path). They propose a correction factor (Fig. 1c in [7]) that depends on the experimentally obtained elastic MFP, thus the number of internal reflections. This correction factor is developed in a V-trajectory, where the block of graphene is treated as ‘jellium’-like material, so scattering is equally possible anywhere inside the material. However, in such a jellium material no interference effects can occur, which is a severe limitation to their model.

The aim of this study is to reconcile both approaches. For this, we start with Geelen et al.’s toy model, and extend it to account for inelastic losses. This has the advantage that interferences are possible, while inelastic processes – which, e.g., lead to a loss of finesse and thus a broadening of the peaks in the interference system - are considered more accurately. We introduce an inelastic loss factor  $\beta$  for every reflection or transmission event. While the losses

upon reflection and transmission may in principle be different, fitting  $\beta$  and  $r$  already allows for this freedom (without introducing redundant parameters). By using only one factor  $\beta$ ,  $(1 - \beta)^2$  can be interpreted as the loss in electron flux per unit cell length  $a$  travelled (see Fig. 3.2). Still the elastic backscattering events only take place at the discrete graphene layers, keeping the interference condition intact. Effectively this means replacing  $r$  and  $t$  by  $\beta r$  and  $\beta t$  [ $r_{n-1}$  and  $t_{n-1}$  remain unchanged, as the factor  $\beta$  is already included inside them in the previous iteration] in equations 2a and 2b, so the modified recursion formulas including  $\beta$  are:

$$t_n = \left[ \frac{\beta t \cdot t_{n-1} e^{i\varphi}}{1 + \beta r \cdot r_{n-1} e^{2i\varphi}} \right] \quad \text{eq. 3a}$$

$$r_n = \left[ \beta r + \frac{\beta^2 t^2 r_{n-1} e^{2i\varphi}}{1 + \beta r \cdot r_{n-1} e^{2i\varphi}} \right] \quad \text{eq. 3b}$$

with  $r_1 = \beta r$  and  $t_1 = \beta t$ . We will use the recursive formulas eq. 3a/b to extract the wave reflection coefficient  $r$  and the loss factor  $\beta$  for each energy and layer count  $n$ .

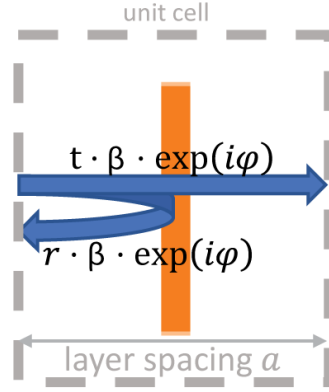


Figure 3.2: Illustration of the improved interference model. Each graphene layer (orange) partially transmits (reflects) the electron wave function with fraction  $t$  (fraction  $r$ ). Over a layer distance  $a$  the phase propagates by  $\varphi$  and the amplitude is damped by the loss factor  $\beta$ . For multilayer graphene, this ‘unit cell’ is repeated.

### 3.3 Results

The reflection and transmission spectra  $R_n(E)$  and  $T_n(E)$  for each energy were calculated from eq. 3a/b (absolute squared) and fitted to the experimental data from Geelen et al. (see Fig. 3.3a/b) using a least square fitting routine with  $r$  and  $\beta$  as the only fitting parameters. The resulting fit has zero degrees of freedom, as there are only two unknowns,  $r(E)$  and  $\beta(E)$ , at each energy and the two electron intensities  $R_n(E)$  and  $T_n(E)$  have been measured. Thus, the fit actually is the result of numerically solving these two equations ( $R(E)$  and  $T(E)$ ) with two unknowns ( $r(E)$  and  $\beta(E)$ ). The fitting code, that invokes the *scipy.optimize.leastsq* routine in the SciPy [14] package, is provided as a python notebook file in the supplemental material [15]. The initial guess of  $r(E)$  and  $\beta(E)$  was estimated from the analytical solution of the one-layer case. After a maximum of 100 iterations, the fit has converged for all datasets except for the 4-layer dataset above 23 eV. These non-converged fits have been disregarded, as the pair of  $R$

and  $T$  values at that energy falls outside the solution space of our model, even with zero degrees of freedom. We attribute this to the low intensity of the (transmitted) electrons, where the noise is comparable to the detector dark count and note that the same applies for the model of Yang et al. at the same datapoints (as seen in the absent data points for the four layer inelastic and elastic MFP in Fig. 2a and Fig. 3 of [7], respectively).

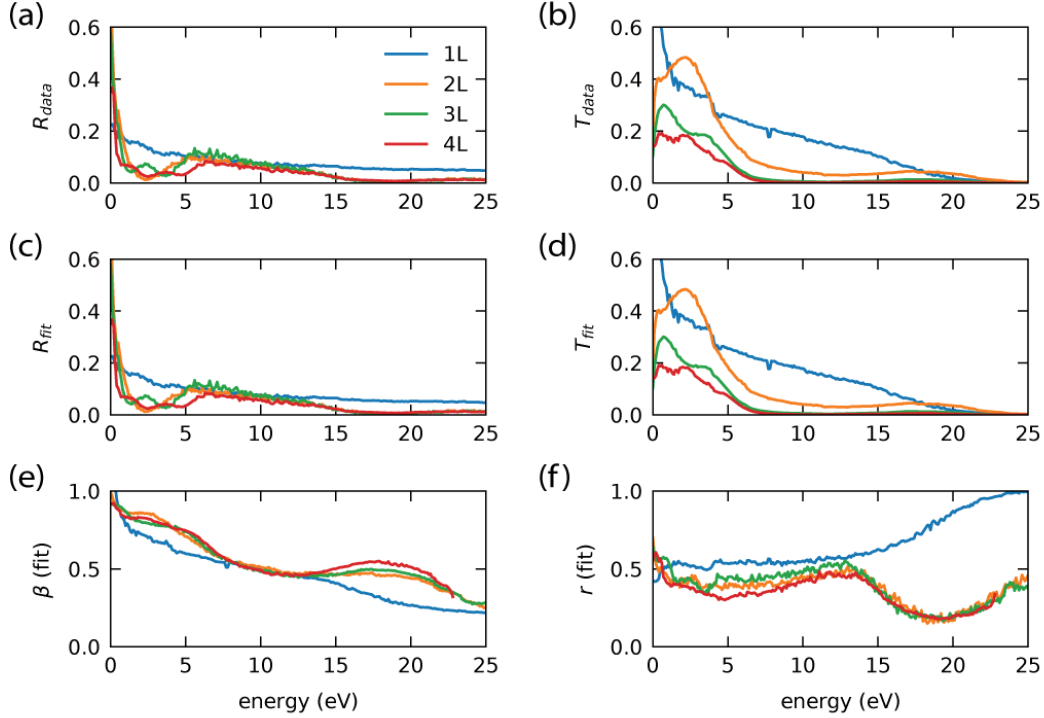


Figure 3.3: Reflectivity (a) and transmissivity (b) data reproduced from Geelen et al. [3]. Best fit of the reflection/transmission equations (panel c, d) to the reflection/transmission data set (panel a,b). The energy-dependent loss parameter  $\beta$  (panel e) and wave reflectivity  $r$  (panel f) were obtained by fitting the improved model (eq. 3) to the transmission and reflection data. This fit, with zero degrees of freedom, was performed for each layer count independently. The fit reproduces the dataset very well, except for the 4-layer data above 23 eV (omitted from plots above 23 eV in panels e and f).

The best fit in  $R$  and  $T$  is shown in Fig. 3.3 c/d, and the fit parameters obtained are shown in Fig. 3.3e/f. The extracted loss factor  $\beta$  (Fig. 3.3e) decreases from nearly 1, i.e., no inelastic loss, at 0 eV to about 0.25 (i.e. 75% loss) for all layer counts. However, the multilayer  $\beta$  spectra follow a distinctly different line from the rather flat monolayer curve, deviating to higher values (less loss) between 2-8 eV and 12-25 eV. The wave reflectivity amplitude  $r$  (Fig. 3.3f) is rather constant for all layer counts up to 13 eV, ranging from  $r = 0.3$  to  $r = 0.55$ . The interference peaks around 3 eV do not show up in the extracted  $r$ . At energies above 13 eV, the monolayer curve diverges from the multilayer curves, with the monolayer curve monotonically increasing to 1, while the multilayer  $r(E)$  curves sharply drop to 0.15 around 18 eV and then increase to 0.4 at 25 eV.

For comparison to previously derived MFPs, we can now calculate the inelastic MFP directly from  $\beta$ , and the elastic MFP from  $t$ . By the relation between wave function and probability

density, the inelastic loss factor in electron flux is  $|\beta|^2 = \beta^2$ . As the inelastic loss takes place once within each interlayer spacing  $a$ , the inelastic MFP  $\lambda_{\text{inel}}$  is obtained from

$$\exp(-a/\lambda_{\text{inel}}) = \beta^2 \Leftrightarrow \lambda_{\text{inel}}/a = \frac{-1}{2 \cdot \ln \beta}. \quad \text{eq. 4}$$

With the same reasoning for the transmissivity  $t$ , the elastic MFP  $\lambda_{\text{el}}$  is obtained from

$$\exp(-a/\lambda_{\text{el}}) = t^2 = 1 - r^2 \Leftrightarrow \lambda_{\text{el}}/a = \frac{-1}{2 \cdot \ln t}. \quad \text{eq. 5}$$

The total MFP then follows from

$$a/\lambda_{\text{tot}} = a/\lambda_{\text{inel}} + a/\lambda_{\text{el}} = -2 \ln \beta - 2 \ln t = -2 \ln (\beta t) \quad \text{eq. 6}$$

which is consistent with interpreting  $(\beta t)^2$  as the total flux transmitted through a single layer after elastic and inelastic scattering.

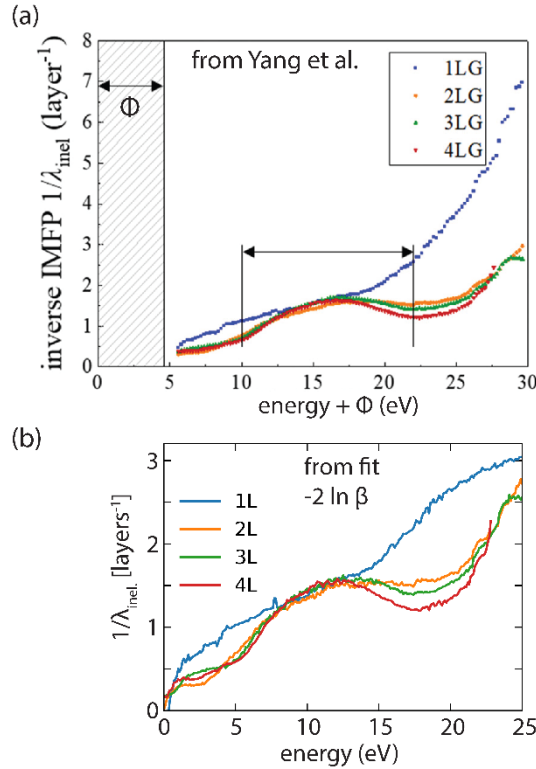


Figure 3.4: Comparison of the inverse IMFP as extracted by (a): Yang et al. (plot adapted from [7]) and (b): present analysis. The energy scales are aligned as Yang et al. use the Fermi level as the reference, which is shifted by the work function from the vacuum level.

The calculation of the inelastic MFP was the focus of the work of Yang et al. [7]. The inverse inelastic MFP they obtained is shown in Fig. 3.4a, alongside the inverse inelastic MFP obtained in the present study (Fig. 3.4b, from the fitted  $\beta$ ). For the multilayers of graphene, the curves obtained in both studies are basically identical. Also, the monolayer curves of both studies resemble each other up to 15 eV. However, they differ at higher energies. While the curve calculated by Yang et al. increases rapidly, the curve obtained here re-joins the multilayer curves again at  $\sim 25$  eV. Thus, the increase of the inverse inelastic MFP in multilayers from 5-15 eV (with respect to  $E_{\text{vac}} = 0$ ) looks less unique in our analysis than in the one by Yang et al., where it was attributed to the excitation of the  $\pi + \sigma$  plasmon. In our analysis the maximum



in inverse inelastic MFP is rather caused by the surrounding local minima. The position of these local minima coincides with the maxima in transmissivity in the multilayer data (Fig. 3.3b). The fact that these local minima show up in the multilayer and not in the monolayer data suggests that they are actually caused by interference of the wave function. While the construction of the model should account for all interference effects, broadening of spectral features in the experiment can move interference effects into the fitting parameters. Also, a scattering effect that is non-linear with the electron flux ‘trapped’ in the cavity would show up in the fitting parameter  $\beta$ . That is, in the semi-classical picture of Figure 3.2, we assume a constant damping factor  $\beta$  for each subsequent reflection between two neighboring layers (Figure 3.1). The peaks in  $\beta$  in the 2-7 and 15-22 eV energy windows (where the transmission resonances occur) indicate that inelastic excitations in subsequent reflections/transmissions may in fact be suppressed.

While the  $\pi + \sigma$  plasmon in multilayer graphene has been calculated [16] and observed [17,18] around 15 eV, it is unclear how it would affect the inelastic MFP-dependence on the energy of the incident electrons. Whereas EELS spectra, e.g. [19,20], show electron intensity as a function of the *energy loss of the scattered electron*, e.g., the loss to a plasmon, the inelastic MFP is a function of *the energy of the incident electron*. In other words, the electrons that are lost from the perpendicularly reflected and transmitted beam at a given energy, make up the total EELS spectrum (integrated over all energy losses) plus electrons scattered elastically over a sufficiently large angle to no longer pass through the contrast aperture. Thus, one might expect to observe a plasmon excitation as a step in the inverse inelastic MFP, at the lowest incident energy that is sufficient to excite that plasmon. At higher incident energies the plasmon can still be excited; actually, the scattering cross section generally grows with energy. To see a local maximum in inverse inelastic MFP, one must argue that the excitation of the plasmon is resonantly enhanced. We are not aware of calculations/studies that support this (at the lowest possible energy for excitation of this plasmon). The fact that the IMFP curve for the monolayer matches the curves for the multilayer IMFPs at the energies where the  $\pi + \sigma$  plasmon should decrease the multilayer IMFP exactly in both Yang et al.’s and in our new analysis further refutes the interpretation as a plasmon loss.

We conclude that the features in the inelastic MFP curve of the multilayers cannot with any certainty be attributed to the  $\pi + \sigma$  plasmon, and must more likely be attributed to non-linear effects due to constructive/destructive interference of the electron waves alternating with incident electron energy. However, the general trend and magnitude of the inelastic MFP curve is robust in the different analyses, running from close to no loss at 0 eV to  $\lambda_{\text{tot}} \approx 1/3$  [layers] at 25 eV.

The total MFP includes elastic and inelastic scattering. The graph obtained by Geelen et al. (calculated from  $T = \exp(-d/\lambda_{\text{tot}})$ , eq. 1 in [3]) is shown in Fig. 3.5a, alongside our new analysis (from the fitted  $t$  and  $\beta$  following eq. 6) in Fig. 3.5b. Both analysis methods yield similar values for  $\lambda_{\text{tot}}$  in the order of a few layer thicknesses. The interference peaks around 3 eV are more visible in the analysis of Geelen et al., but they still show up in our analysis (where they are mostly absorbed in the improved model). As a result, the total MFP in our analysis is

rather flat up to 4 eV for the multilayers, ranging from 1.5 to 2 layer thicknesses. At energies above 10 eV and in the monolayer case the two analysis methods yield the same numbers.

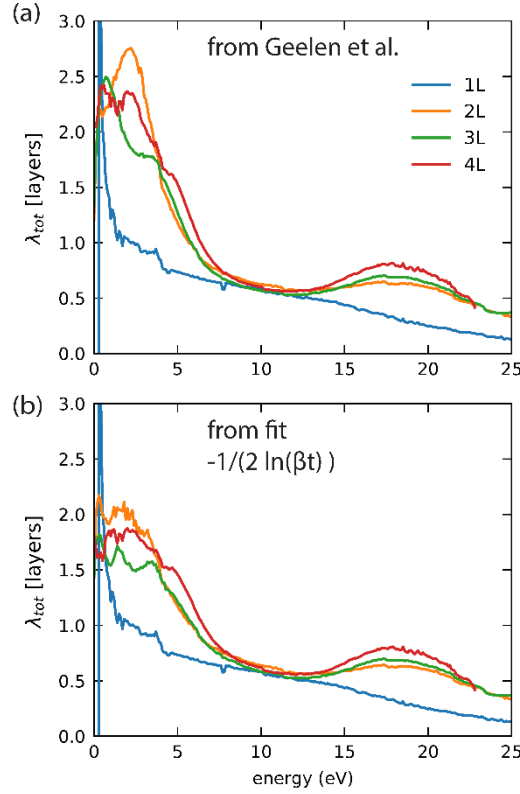


Figure 3.5: Total MFP obtained by Geelen et al. [3] (a) compared to the outcome of the fit (b). In the present study the loss factor  $\beta$  and the transmissivity factor  $t$  were fitted, yielding the flux transmitted through one layer  $(\beta t)^2$ . The total MFP in (b) shows less variation at low energy, as the elastic interference peaks are absorbed into the fitted model.

The elastic MFP is the most striking result in the analysis of Geelen et al. [3] (reproduced in Fig. 3.6a), sharply rising at the transmission resonances. Note that in Geelen et al.'s definition the elastic MFP is not a material property of an individual layer, but rather a macroscopic way of describing the interferences in  $n$  layers of graphene. To check consistency with Geelen et al.'s model, we calculate the elastic MFP according to  $\lambda_{\text{el}}^{-1} = \lambda_{\text{tot}}^{-1} - \lambda_{\text{inel}}^{-1}$  from the total MFP of Geelen et al. (which closely resembles the total MFP obtained in the present study, see Fig. 3.5) and the inelastic MFP obtained from fitting  $\beta$  (which resembles its counterpart in Yang et al.'s study, at least for the multilayer). The result is shown in Fig. 3.6b. In this analysis the maxima of elastic MFP around 3 eV and 18 eV are much broader than in Geelen et al.'s analysis and the curves for different layer counts fall closer together, indicating that they describe a material property less dependent on layer count.

Finally, the elastic MFP in Fig. 3.6c directly follows from the fit parameter  $t$ , according to eq. 5. In the elastic MFP obtained from  $t$ , the multilayer  $\lambda_{\text{el}}(E)$  shows a maximum of 30-40 layers around 18 eV and a rather smaller increase around 5 eV. The fact that no sharp maxima appear around the first transmission resonance around 3 eV indicates that the interferences are fully accounted for in the improved model.

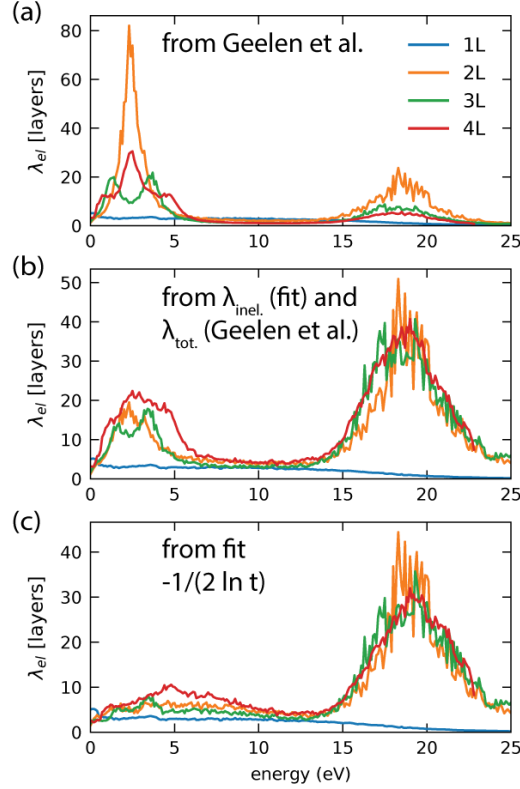


Figure 3.6: The energy dependence of the elastic MFP obtained (a) by Geelen et al. [3], (b) by combining the total MFP from Geelen et al. with the inelastic MFP obtained in this study ( $\lambda_{el}^{-1} = \lambda_{tot}^{-1} - \lambda_{inel}^{-1}$ ), and (c) directly from the fitting parameter  $t$ .

While Geelen et al.'s elastic MFP (Fig. 3.6a) peaks highest at the first resonance (3 eV), the other calculations find the highest maximum at the second (18 eV) resonance. This is caused by the rather macroscopic definition used by Geelen et al., compared to the definition from the wave transmissivity  $t$  used here. Whichever definition one follows in a semi-classical model, the enhanced elastic MFP is a measure for enhanced transmission.

### 3.4 Conclusions

We have applied an improved version of Geelen et al.'s wave-optical model for electron scattering that reproduces both the elastic features linked to interference of the electron wave, and the inelastic features linked to inelastic losses. In the improved model the loss factor  $\beta$  is applied once at every interaction with a discrete graphene layer, thus describing the multiple-scattering zig-zag path travelled. We obtain the energy-dependent inelastic MFP, which over large ranges closely resembles the analysis of Yang et al. but which does converge at energies around 0 eV, 12 eV and 25 eV for the different layer counts. Furthermore, the maximum in the inverse inelastic MFP (minimum in  $\beta$ ) around 12 eV is ascribed to the neighboring interference minima rather than to the excitation of the  $\pi + \sigma$  plasmon, as done by Yang et al.. This is confirmed by the fact that the inelastic MFP at the  $\pi + \sigma$  plasmon excitation is the same for the monolayer and the multilayers. We stress again that all models that define a MFP are semi-classical approximations.

While the definition of elastic MFP is debatable, as it strongly depends on the semi-classical approximations made, the elastic MFP clearly increases to multiple layers in the resonances where elastic transmission increases, depending on layer count. Increased transmission goes hand-in-hand with reduced inelastic loss. A full explanation of this correlation must await a more realistic fully quantum mechanical treatment of electron scattering in multilayer graphene, including inelastic effects.

## Acknowledgements

We acknowledge Marcel Hesselberth for indispensable technical support and Tobias A. de Jong for valuable discussions and code review.

## Funding

This research was supported by the Dutch Research Council (PN, NWO Vrije Programma TNW18.071).

## Appendix

The relevant python code can be found in the supporting information provided with the publication [15].

## References

- [1] S. Tanuma, T. Shiratori, T. Kimura, K. Goto, S. Ichimura, C.J. Powell, Experimental determination of electron inelastic mean free paths in 13 elemental solids in the 50 to 5000 eV energy range by elastic-peak electron spectroscopy, *Surf. Interface Anal.* 37 (2005) 833–845. <https://doi.org/10.1002/sia.2102>.
- [2] M.P. Seah, W.A. Dench, Quantitative electron spectroscopy of surfaces: A standard data base for electron inelastic mean free paths in solids, *Surf. Interface Anal.* 1 (1979) 2–11. <https://doi.org/10.1002/sia.740010103>.
- [3] D. Geelen, J. Jobst, E.E. Krasovskii, S.J. van der Molen, R.M. Tromp, Nonuniversal Transverse Electron Mean Free Path through Few-layer Graphene, *Phys. Rev. Lett.* 123 (2019) 086802. <https://doi.org/10.1103/PhysRevLett.123.086802>.
- [4] B. Da, J. Liu, M. Yamamoto, Y. Ueda, K. Watanabe, N.T. Cuong, S. Li, K. Tsukagoshi, H. Yoshikawa, H. Iwai, S. Tanuma, H. Guo, Z. Gao, X. Sun, Z. Ding, Virtual substrate method for nanomaterials characterization, *Nat. Commun.* 8 (2017) 15629. <https://doi.org/10.1038/ncomms15629>.
- [5] H.T. Nguyen-Truong, B. Da, L. Yang, Low-energy electron inelastic mean free path for monolayer graphene Low-energy electron inelastic mean free path for monolayer graphene, 033103 (2020). <https://doi.org/10.1063/5.0016284>.
- [6] Z. Dai, Z. Gao, S.S. Pershoguba, N. Tiwale, A. Subramanian, Q. Zhang, C. Eads, S.A. Tenney, R.M. Osgood, C.Y. Nam, J. Zang, A.T.C. Johnson, J.T. Sadowski, Quantum-Well Bound States in Graphene Heterostructure Interfaces, *Phys. Rev. Lett.* 127 (2021) 86805. <https://doi.org/10.1103/PhysRevLett.127.086805>.
- [7] L.H. Yang, B. Da, H. Yoshikawa, S. Tanuma, J. Hu, J.W. Liu, D.M. Tang, Z.J. Ding, Low-energy electron inelastic mean free path and elastic mean free path of graphene, *Appl. Phys. Lett.* 118 (2021) 053104. <https://doi.org/10.1063/5.0029133>.
- [8] T. Eberlein, U. Bangert, R.R. Nair, R. Jones, M. Gass, A.L. Bleloch, K.S. Novoselov, A. Geim, P.R. Briddon, Plasmon spectroscopy of free-standing graphene films, *Phys. Rev. B - Condens. Matter Mater. Phys.* 77 (2008) 1–4. <https://doi.org/10.1103/PhysRevB.77.233406>.
- [9] N. Barrett, E.E. Krasovskii, J.M. Themlin, V.N. Strocov, Elastic scattering effects in the electron mean free path in a graphite overlayer studied by photoelectron spectroscopy and LEED, *Phys. Rev. B - Condens. Matter Mater. Phys.* 71 (2005) 1–9. <https://doi.org/10.1103/PhysRevB.71.035427>.
- [10] D.J. Griffiths, Time-Independent Schrödinger Equation, in: *Introd. to Quantum Mech.* ISBN 0131911759, 2nd ed., 2004.
- [11] B. Stec, C. Jędrzejek, Resonance scattering by a double square-well potential, *Eur. J. Phys.* 11 (1990) 75–81. <https://doi.org/10.1088/0143-0807/11/2/002>.
- [12] N. Ismail, C.C. Kores, D. Gekus, M. Pollnau, Fabry-Pérot resonator: spectral line shapes, generic and related Airy distributions, linewidths, finesses, and performance at low or

frequency-dependent reflectivity, *Opt. Express* 24 (2016) 16366. <https://doi.org/10.1364/OE.24.016366>.

[13] H. Hibino, H. Kageshima, F. Maeda, M. Nagase, Y. Kobayashi, Y. Kobayashi, H. Yamaguchi, Thickness Determination of Graphene Layers Formed on SiC Using Low-Energy Electron Microscopy, *E-Journal Surf. Sci. Nanotechnol.* 6 (2008) 107–110. <https://doi.org/10.1380/ejsnt.2008.107>.

[14] P. Virtanen, R. Gommers, T.E. Oliphant, M. Haberland, T. Reddy, D. Cournapeau, E. Burovski, P. Peterson, W. Weckesser, J. Bright, S.J. van der Walt, M. Brett, J. Wilson, K.J. Millman, N. Mayorov, A.R.J. Nelson, E. Jones, R. Kern, E. Larson, C.J. Carey, Í. Polat, Y. Feng, E.W. Moore, J. VanderPlas, D. Laxalde, J. Perktold, R. Cimrman, I. Henriksen, E.A. Quintero, C.R. Harris, A.M. Archibald, A.H. Ribeiro, F. Pedregosa, P. van Mulbregt, A. Vijaykumar, A. Pietro Bardelli, A. Rothberg, A. Hilboll, A. Kloeckner, A. Scopatz, A. Lee, A. Rokem, C.N. Woods, C. Fulton, C. Masson, C. Häggström, C. Fitzgerald, D.A. Nicholson, D.R. Hagen, D. V. Pasechnik, E. Olivetti, E. Martin, E. Wieser, F. Silva, F. Lenders, F. Wilhelm, G. Young, G.A. Price, G.L. Ingold, G.E. Allen, G.R. Lee, H. Audren, I. Probst, J.P. Dietrich, J. Silterra, J.T. Webber, J. Slavič, J. Nothman, J. Buchner, J. Kulick, J.L. Schönberger, J.V. de Miranda Cardoso, J. Reimer, J. Harrington, J.L.C. Rodríguez, J. Nunez-Iglesias, J. Kuczynski, K. Tritz, M. Thoma, M. Newville, M. Kümmerer, M. Bolingbroke, M. Tartre, M. Pak, N.J. Smith, N. Nowaczyk, N. Shebanov, O. Pavlyk, P.A. Brodtkorb, P. Lee, R.T. McGibbon, R. Feldbauer, S. Lewis, S. Tygier, S. Sievert, S. Vigna, S. Peterson, S. More, T. Pudlik, T. Oshima, T.J. Pingel, T.P. Robitaille, T. Spura, T.R. Jones, T. Cera, T. Leslie, T. Zito, T. Krauss, U. Upadhyay, Y.O. Halchenko, Y. Vázquez-Baeza, *SciPy 1.0: fundamental algorithms for scientific computing in Python*, *Nat. Methods* 17 (2020) 261–272. <https://doi.org/10.1038/s41592-019-0686-2>.

[15] P.S. Neu, D. Geelen, R.M. Tromp, S.J. van der Molen, Extracting transverse electron mean free paths in graphene at low energy, *Ultramicroscopy* 253 (2023) 113800. <https://doi.org/10.1016/j.ultramic.2023.113800>.

[16] V.U. Nazarov, Electronic excitations in quasi-2D crystals: what theoretical quantities are relevant to experiment?, *New J. Phys.* 17 (2015) 073018. <https://doi.org/10.1088/1367-2630/17/7/073018>.

[17] W.S.M. Werner, A. Bellissimo, R. Leber, A. Ashraf, S. Segui, Reflection electron energy loss spectrum of single layer graphene measured on a graphite substrate, *Surf. Sci.* 635 (2015) L1–L3. <https://doi.org/10.1016/j.susc.2014.12.016>.

[18] I. Konvalina, B. Daniel, M. Zouhar, A. Paták, I. Müllerová, L. Frank, J. Piños, L. Průcha, T. Radlička, W.S.M. Werner, E.M. Mikmeková, Low-Energy Electron Inelastic Mean Free Path of Graphene Measured by a Time-of-Flight Spectrometer, *Nanomaterials* 11 (2021) 2435. <https://doi.org/10.3390/nano11092435>.

[19] J. Lu, K.P. Loh, H. Huang, W. Chen, A.T.S. Wee, Plasmon dispersion on epitaxial graphene studied using high-resolution electron energy-loss spectroscopy, *Phys. Rev. B - Condens. Matter Mater. Phys.* 80 (2009) 2–5. <https://doi.org/10.1103/PhysRevB.80.113410>.

[20] S.C. Liou, C.S. Shie, C.H. Chen, R. Breitwieser, W.W. Pai, G.Y. Guo, M.W. Chu,  $\Pi$ -Plasmon Dispersion in Free-Standing Graphene By Momentum-Resolved Electron Energy-Loss Spectroscopy, *Phys. Rev. B - Condens. Matter Mater. Phys.* 91 (2015) 1–7. <https://doi.org/10.1103/PhysRevB.91.045418>.

# 4 SYMMETRIES OF ELECTRON INTERACTIONS WITH hBN- GRAPHENE HETEROSTACKS

---

Parts of this chapter are to be published as: P.S. Neu, E.E. Krasovskii, R.M. Tromp, S.J. van der Molen, *Bi-directional LEEM and eV-TEM spectra of a graphene-hBN heterostack*.



## 4.1 Introduction

Stacking two different van der Waals (vdW) materials produces a heterostructure that breaks the out-of-plane symmetry of the sample [1]. The graphene-hBN heterostack is commonly used in experiments, where hBN provides an insulating flat surface for the graphene with a minimal lattice mismatch [2,3]. Placing the graphene on or between hBN is known to yield better transport characteristics (e.g., higher electron mobility [4–6] and superconductivity in twisted bilayer graphene [7]) than on other common substrates like silicon or silicon nitride. It is generally assumed that the coupling of hBN to the graphene can be neglected at the Fermi level, as hBN is a large band gap insulator [8,9].

Like graphene, hBN is a vdW material with a hexagonal lattice, with each boron (B) atom bonding to three nitrogen (N) atoms in plane and vice versa. Unlike in transition metal dichalcogenides (TMDs), the B and the N atoms in hBN lie in the same plane. Following the interference toy model we applied for graphene layers [10], one can hence expect interlayer states in multilayer hBN, and even in a graphene-hBN heterostack.

Jobst et al. [11] have previously investigated hBN interlayer states using LEEM. They showed splitting of the hBN interlayer states for two to five layers of hBN on silicon, similar to the case of two to five layers of graphene. Furthermore, they presented calculations explaining that few-layer graphene on *bulk* hBN retains its characteristic splitting of the interlayer state, while few-layer graphene on few-layer hBN should show a mixed interlayer state.

Hibino et al. [12] have reported on mono- and bilayer graphene on top of mono- and bilayer hBN on a Cobalt (Co) surface. They measured LEEM-IV spectra showing a characteristic interlayer state minimum even for one layer graphene on one layer hBN, and a splitting of the minimum upon adding more layers of graphene and/or hBN.

In this chapter, we discuss measurements on a hBN-on-graphene heterostructure sample that is suspended over the 2- $\mu\text{m}$  holes of a TEM grid. We present LEEM- and eV-TEM-IV spectra of this free-standing heterostructure and compare these to the previously published reports. The combination of transmission and reflection data allows us to determine elastic and inelastic path lengths for the electrons, as a function of their energy. The fact that the sample is prepared on a TEM grid also allows us to investigate the role of symmetry. We can flip the sample and measure LEEM and eV-TEM spectra on the reversed order of layers.

## 4.2 Results

### 4.2.1 Geometry and images

The hBN-on-graphene heterostack is prepared by the polymer-free transfer method [13] using hBN and graphene grown on copper (Cu) by chemical vapor deposition (CVD) (purchased from Graphene Laboratories [14] and Graphenea [15], respectively). The graphene on Cu is floated on an ammonium persulfate (APS) solution until the Cu is etched away and the graphene is picked up with the hBN-on-copper substrate. The resulting graphene-hBN-Cu stack is then flipped and the copper is again etched away by the APS solution. The floating hBN-graphene

stack is then picked up by a SiN holey TEM grid [16] brought in contact from the top. The sample fabrication is illustrated in more detail in the appendix Figure 4.A1.

In the usual orientation of the TEM grid, i.e., with the flat side towards the LEEM objective lens, the resulting order of layers as seen from the LEEM objective lens-side is: hBN (on top of) / graphene (on top of a holey) / SiN TEM grid. The graphene and the hBN layers are sandwiched together with the sides that had been in contact with copper before facing outwards.

Previous inspection of the CVD-grown materials by LEEM has shown that there are multilayer areas of elongated folds or tears in the graphene and triangular multilayer areas in the hBN.

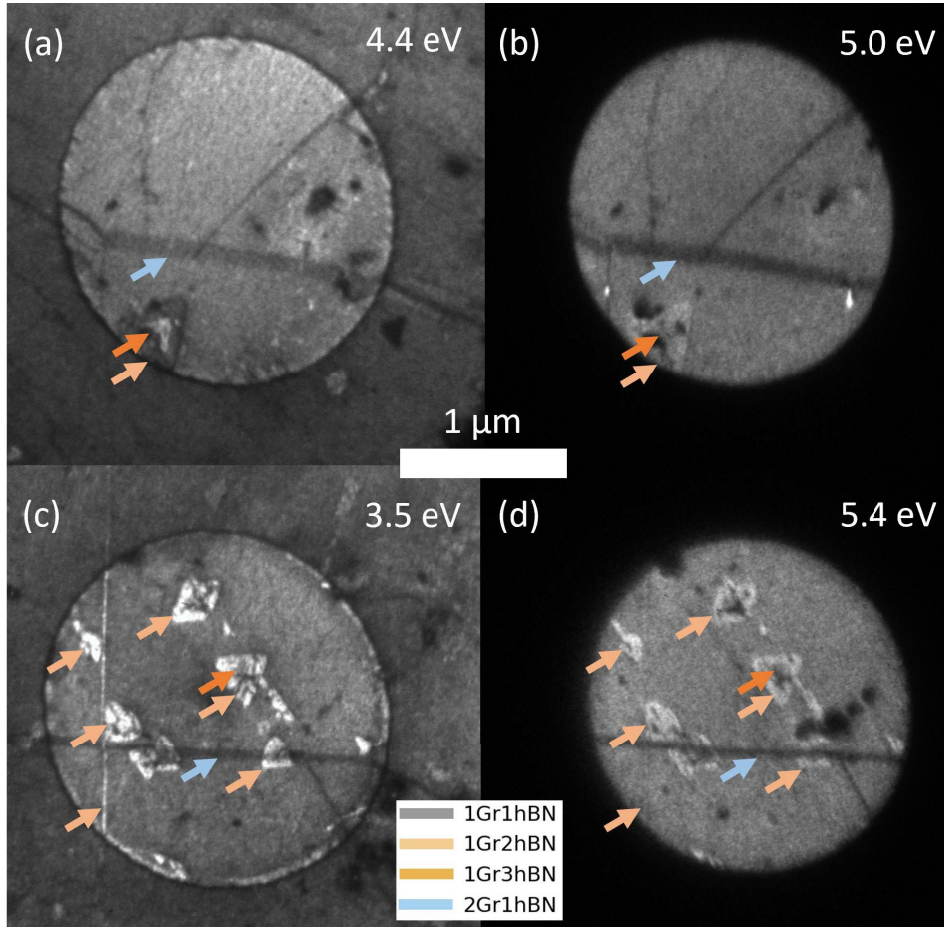


Figure 4.1: LEEM images (a, c) and eV-TEM images (b,d) of the hBN-on-graphene heterostack. While most areas are covered with one layer of hBN on top of one layer of graphene, some triangles of additional layers of hBN and lines of additional graphene layers show. The Pt/Pd-coated SiN support grid is impenetrable for the electrons and roughens the layered material on top of it, compared to the free-standing areas. The arrows point to areas with an additional layer of graphene (2Gr1hBN) and additional layers of hBN (1Gr2hBN and 1Gr3hBN). The other areas are one layer of hBN on one layer of graphene (1Gr1hBN).

The LEEM and eV-TEM images of the heterostructure on top of a TEM grid hole (see Figure 4.1) show multilayer areas that have characteristic shapes for either graphene or hBN. Firstly, there are long stripes pointed out by the blue arrows in Figure 4.1, that have the same shape as stripes previously seen in graphene-only samples and are thus ascribed to folds and tears in the graphene. (We will confirm the layer count below by comparing the spectra to the previous

publication of Hibino et al. [12].) Secondly, the triangles marked by orange arrows are characteristic for hBN grown by CVD. Previous inspection of the hBN on copper, as used for the transfer, revealed the presence of multilayer triangles. Furthermore, the continuity between these multilayer areas also shows that the majority of the sample is covered by a monolayer of graphene with a monolayer of hBN on top, denoted as 1Gr1hBN.

We note that the free-standing area is more reflective than the area supported by the Pt/Pd coated TEM grid throughout the energy range. This is similar to what we have previously seen for graphene samples and is attributed to a higher flatness of the free-standing area [17,18]. The images shown in Figure 4.1 are part of an energy scan up to 30 eV electron energy recorded with a contrast aperture (equivalent diameter  $\sim 0.3 \text{ \AA}^{-1}$  for LEEM and  $\sim 0.6 \text{ \AA}^{-1}$  for eV-TEM) placed around the specular spot.

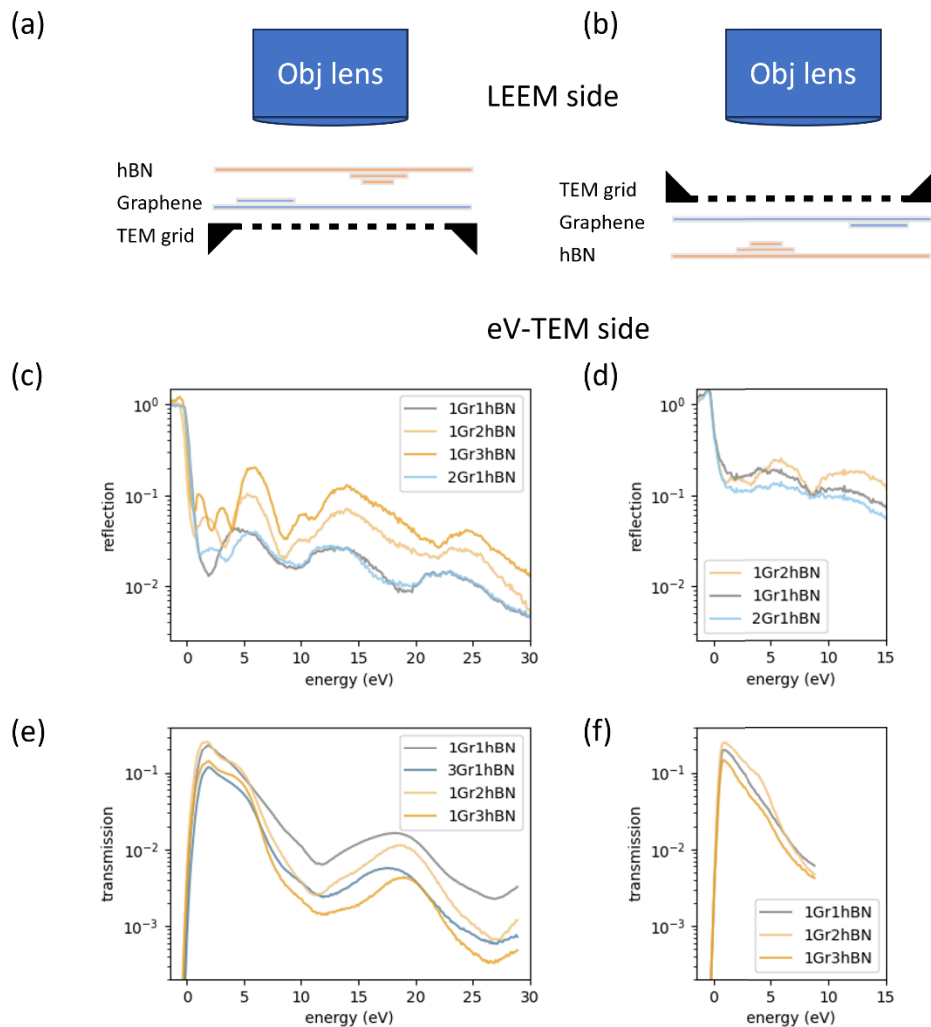


Figure 4.2: Sketch of the graphene-hBN heterostack sample with (a) the original orientation (reflection from the hBN side), with the reflection spectra (c) and transmission spectra (e) measured in this configuration. For the subsequent measurements the sample was flipped as shown in (b) (reflection from the graphene side) and the reflection/transmission spectra (d) and (f), respectively, were acquired in this flipped orientation.

The option of flipping the sample allows us to acquire four spectra on the same sample. These four spectra cover all possibilities of perpendicular electron transmission and reflection of the sample. In the left column of Figure 4.2, we show the spectra recorded in the usual configuration (with the hBN side towards the LEEM lens as sketched in Figure 4.2a), with the reflection spectra in Fig. 4.2c) and the transmission spectra in Fig. 4.2e). In the right column of Figure 4.2, the spectra recorded in the flipped configuration (with the graphene side towards the LEEM lens as sketched in panel b) are depicted, with reflection and transmission spectra in panel 2d) and 2f), respectively.

The spectra d) and f) acquired with the flipped geometry are cut off at 15 and 10 eV, respectively, as the spatial resolution, especially limited by astigmatism, does not allow for distinguishing between the areas of different layer count at higher energies. The imaging conditions are inherently worse in the flipped condition, as the holey silicon nitride (SiN) membrane is recessed into the SiN frame. Since the potential difference from the sample to the electron lens is much larger on the LEEM side (15 kV) than on the eV-TEM side ( $\sim 200$  V), the electric equipotential surfaces close to the TEM grid are much more curved, when the recessed (instead of the flat side) of the TEM-grid is facing the LEEM side. The curved equipotential surfaces, i.e., the in-plane electric field, deflect the electrons when imaging an area that is not the center of the TEM grid. The deflection can be compensated to some degree by tilting the sample (relative to the LEEM lens), adjusting the centering on the aberration correcting mirror, and – in the LEEM and not the eV-TEM case – adjusting the incidence angle of the electrons. However, these compensations are optimized at a low energy and get worse with increasing energy.

## 4.2.2 Spectra

When we concentrate on the spectra recorded in the original orientation first (Figure 4.2 c/e), some general trends are visible upon adding more layers of graphene and hBN. We will name them here, before discussing them in more detail:

1. Increased reflectivity and decreased transmissivity with an increasing number of layers.
2. Splitting of the band at 0-5 eV with every added layer and graphene/hBN dependent shift.
3. Development of the hBN-specific minima that correspond to a band at 8-11 eV upon adding hBN layers.
4. Graphene/hBN dependent shift of the  $\sim 20$  eV band.

First, the reflectivity is increasing with an increasing number of layers, whereas the transmissivity is decreasing. This is expected in a framework of elastic and inelastic mean free paths (MFPs). The transmissivity has to generally decrease with layer count, as electrons are scattered inelastically with a certain probability in each layer. With a constant inelastic mean free path ( $\lambda_{\text{IMFP}}$ ), the flux of electrons not intercepted by inelastic scattering decreased exponentially, as  $T \propto \exp(-d/\lambda_{\text{IMFP}})$ . The reflectivity increases with layer count (at least far from the bands), as the electrons can elastically reflect from every layer with a certain probability. As we have argued in the toy model based on interference of the wave function (see Chapter 3), the reflected electron will undergo multiple elastic scattering processes in

between the layers, producing the interlayer states. But this is a higher order effect, so it is true that reflectivity generally increases with layer count.

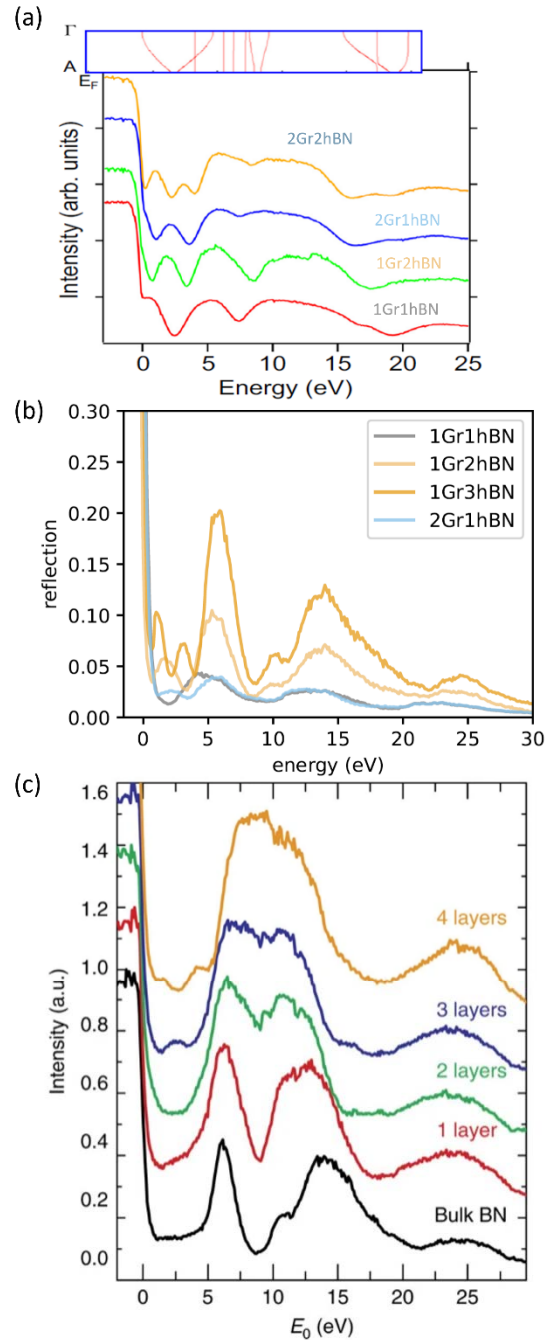


Figure 4.3: Comparison of LEEM spectra of (b) our hBN-on-graphene to previously reported non-free-standing graphene by (a) Hibino et al. [12] and (c) Jobst et al. [11]. Hibino et al measured graphene (CVD grown on Cu and transferred) on top of hBN grown on Co. Jobst et al. measured few-layer exfoliated graphene on top of bulk hBN. The inset in (a) shows the band structure of a periodically continued graphene-hBN heterostack (along the out-of-plane direction).

Still, it is notable, that the increase in reflectivity in Figure 4.2c is small for an added layer of graphene, i.e., the 2Gr1hBN curve, and comparably large for added layers of hBN, i.e., the

1Gr2hBN curve. The same small effect has been seen in the graphene-only samples in Chapter 3.

Second, the splitting of the low energy interlayer state is visible in both LEEM and eV-TEM. In the LEEM spectra, the energy resolution is sufficient for counting of the total number of layers. The number of minima only depends on the number of layers, not whether these are graphene or hBN layers. Like in graphene, there are  $n - 1$  minima for  $n$  layers. Nevertheless, the energies of the interlayer states shift depending on whether more graphene or hBN is added, as we will discuss later with help of Figure 4.4.

In the eV-TEM spectra the splitting of the interlayer state leads to a striking situation, where the transmissivity of the 1Gr2hBN stack oscillates around the transmissivity of the 1Gr1hBN stack, i.e., the transmissivity increases at 2 eV and 5 eV upon adding a layer of hBN, although the electrons have to pass three layers as opposed to two in the 1Gr1hBN case. This example shows how important it is to distinguish between elastic and inelastic MFP. In a material that is dominated by inelastic scattering, a thicker sample would always have a lower transmissivity.

We highlight that the existence and splitting of the interlayer state is evidence for the cleanliness of the graphene-hBN interface. The surfaces that are brought in contact with the polymer-free transfer method are the top surfaces that were exposed to air and have not undergone specific cleaning steps. Thus, these interlayer states can also be expected in other vdW heterostructure devices.

Third, the hBN-specific band at 8-11 eV becomes more pronounced with an increased layer count of hBN. This band is known from the bulk hBN data and calculations, e.g., [11,12,19–21], and does not exist in graphene (compare [22,23]). In the LEEM spectrum, it is visible for the data with only one layer of hBN and splits in two distinguishable dips for more layers of hBN. [it is not discernible in the eV-TEM spectrum].

Fourth, the band around 20 eV, that manifests itself in the data as a minimum in reflectivity and a maximum in transmissivity, shifts to lower energy for more graphene-like heterostacks and to higher energy for more hBN-like heterostacks. The state is seen in both (bulk) graphene and (bulk) hBN. In our interference toy model, it is the result of the second order interference (whereas the 0-5 eV split band results from the first order interference), and thus an interlayer state. No layer-dependent splitting of the state is visible, which is attributed to increased inelastic scattering at higher energies. We will discuss this shift in more detail when comparing to the data of Hibino et al. [12] in Figures 4.3 and 4.4.

The reflection spectra (in the original orientation) are reprinted in Figure 4.3b, alongside the spectra published by Hibino et al. [12] and Jobst et al. [11], in Figures 4.3a and 4.3c, respectively, on an aligned energy scale. While our sample consists of hBN on graphene, the other publications report on graphene on hBN. Thus, the hBN-specific minimum in their spectra is cloaked by the addition of more graphene on top [24]. Also, in the LEEM spectrum in Figure

4.2 d the cloaking effect is visible. It is clear that, if the total MFP of the probing electron is in the order of a few layers, the top layer will have the largest contribution to the reflectivity, whereas the layers past the MFP barely contribute to the reflectivity.

Furthermore, all the spectra in Figure 4.3 show the second order interference state, that shifts with addition of graphene or hBN, and the first order interference state. The 0-5 eV band from Hibino et al. shows the same number of splittings as our data, only depending on the number layers. In the data of Jobst et al., the splitting of the state only depends on the number of graphene layers, with  $n - 1$  minima for  $n$  graphene layers. While this appears contradictory, they show in their Figure 4.4b [11], how the interference pattern between graphene and hBN develops into a pattern of only the few layer graphene, upon increasing the hBN layer count from 5 to 22 and applying a Gaussian broadening to mimic the energy resolution of the setup.

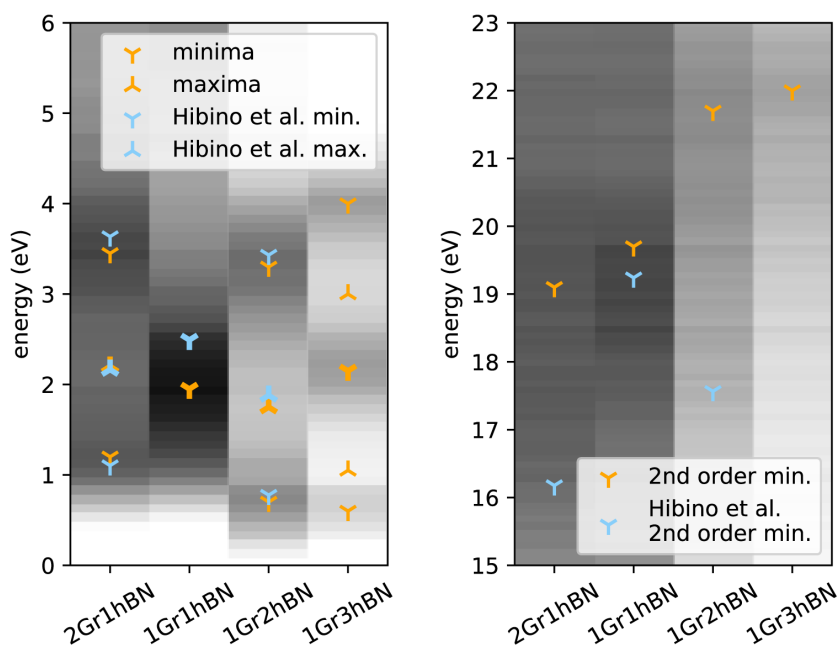


Figure 4.4: Energy shift of the reflectivity minima and maxima of different graphene/hBN combinations as found in our data and by Hibino et al. [12]. The measured spectra of each layer count (see Figure 4.2c) are shown in the grayscale in the background. A splitting and shift are seen in the low-energy interlayer state (a, 0-5 eV). The central minimum/maximum is printed bold for orientation. The second interlayer state (b, around 20 eV) also shifts depending on the hBN/graphene likeness of the heterostack.

To discuss the shift of the minima/maxima upon addition of graphene or hBN, we plot the minima and maxima energies in Figure 4.4, for our data and the data by Hibino et al. The energy of the interlayer states shifts depending on whether more graphene or hBN is added to the 1Gr1hBN heterostack.

For the 0-5 eV band (see Figure 4.4a) in our data, the maximum of the 1Gr2hBN spectrum is shifted to  $\sim 0.3$  eV lower than the minimum of the 1Gr1hBN spectrum, whereas the 2Gr1hBN spectrum is shifted to  $\sim 0.2$  eV higher energy. Also, the mirror mode transition is shifted to lower energy in the more hBN-like stacks (see Figure 4.3b), indicating a lowering of the work

function, as the Fermi levels are aligned. In the data of Hibino et al. (see Figure 4.3a), the 1Gr2hBN interlayer and 2Gr1hBN states resemble our states, shifting to lower energy for more hBN (Figure 4.4a). However, the 1Gr1hBN minimum does not lay on that line, suggesting that the Co substrate shifts the states compared to our free-standing sample. In LEEM, the effect of the Co substrate on the spectra will decay with increasing thickness of the samples.

The band around 20 eV, with the minima plotted in Figure 4.4b, shifts to lower energy for more graphene-like heterostacks and to higher energy for more hBN-like heterostacks. This trend is also visible in the spectra from Jobst et al. [11], that are reprinted in Figure 4.3c, for more layers of graphene added on top of bulk hBN. In the spectra by Hibino et al. [12] (reprinted in Figure 4.3a) however, the band moves to lower energy irrespective of whether graphene or hBN is added. We attribute this to the fact that the Gr/hBN minimum in Hibino et al.'s data is already higher than in our data ( $\sim 21$  eV), probably caused by the Co substrate in their experiment. Also, as Hibino et al. are considering graphene on hBN, one can expect that the graphene top layer dominates the LEEM spectrum. However, like in the 0-5 eV band, that 1Gr1hBN data seems to be the outlier, with the 2Gr1hBN band at higher energy than the 1Gr2hBN band, as in our data.

### 4.2.3 Calculated spectra and electron density distributions

As the experimental spectra are acquired on free-standing areas, they are free of substrate effects and especially suited for comparison to calculations. The electron density and the resulting reflectivity were calculated by our collaborator Eugene E. Krasovskii by constructing the Bloch eigenfunctions from matching augmented plane waves for a periodic continuation of the respective heterostack [25,26]. The calculated reflection spectra for the 1Gr1hBN, 1Gr2hBN, and 2Gr1hBN stacks are shown in Figure 4.5.  $R(E)$  is the reflected intensity in the specular spot, thus directly comparable to the LEEM data. By comparison to experiment, the work function was fitted to be  $\Phi = E_{\text{vac.}} - E_{\text{F}} \approx 4.3$  eV. We note that no loss is applied, implying that – as long as no diffracted beams are formed – all electrons are either reflected or transmitted. The calculated reflection spectra of the flipped heterostacks coincided with the original orientation except for numerical errors, thus they are not shown in Figure 4.5. We will discuss how losses break this symmetry later (see section 4.2.5).

The projected electron densities in Figure 4.6 actually differ for the two different orientations of a stack. The color in each plot shows the electron density, thus the absolute square of the electron wave function (Bloch eigenfunction) at a given energy. As the calculation is done in three dimensions, the electron density is projected onto the out-of-plane dimension. The horizontal axis shows the out-of-plane dimension, with the electrons incident from the right, and the position of each layer marked. The transmission states show up as maxima on the left side of the sample, characteristic maxima inside the sample, and minima on the right side, the reflection side, of the sample.

We will discuss the spectra (Fig. 4.5) and the electron density (Fig. 4.6) in conjunction, following the order of features as discussed previously for the experiments.

Firstly, the lowest energy reflectivity minimum that is related to the first interference state shows an energy shift depending on the added material. Like in our experiment, the state seen



for 1Gr1hBN splits and shifts to lower energy upon the addition of a layer of hBN or splits and shifts to higher energy upon the addition of a layer of graphene. The electron density of the state is centered in between the layers, as is expected for the interference state, but also has some electron density in the layer, with more in the hBN than in the graphene layer.

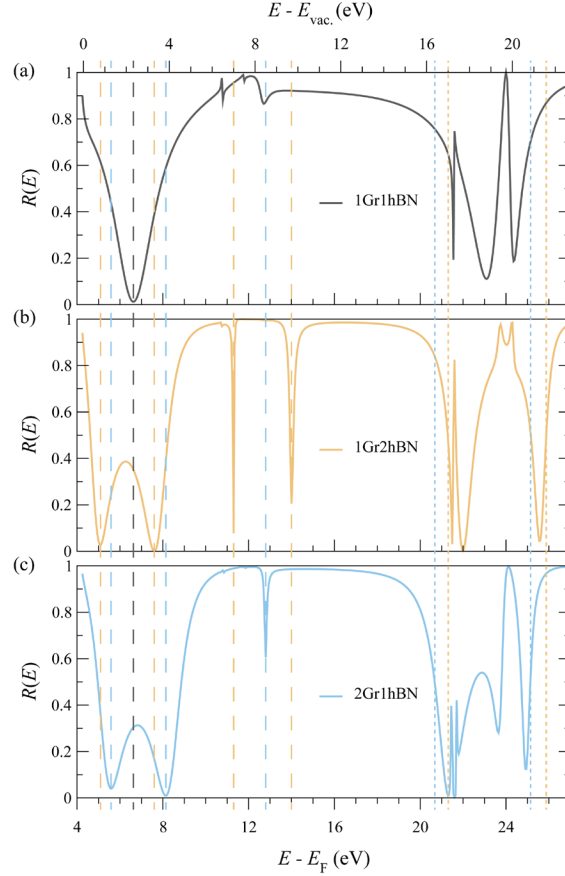


Figure 4.5: Calculated reflectivity of the bilayer and the two different trilayer stacks in the specular spot without loss. The low energy reflectivity minima are marked with dashed lines in the corresponding colors to compare their energies. For the bands above 20 eV (with respect to  $E_F$ ) the dotted lines indicate the energies of 50% reflectivity, as we can only resolve a general broad minimum at that high energy in experiment. The energy shifts of the low energy minima, the splitting of the  $\sim 13$  eV minimum, and the general shift of the broad high energy minimum are also seen in experiment, compare Fig. 4.2c and Fig. 4.4. Calculations by E.E. Krasovskii.

Secondly, the hBN-specific state around  $E = 9$  eV with respect to  $E_{\text{vac.}}$  ( $\approx E_F + 13$  eV) shows up as one minimum in the 1Gr1hBN and 2Gr1hBN spectra, i.e., the spectra that have one hBN layer, and as two minima in the 1Gr2hBN spectrum. Other experiments [11,12,19] and calculations [12,20,27] on multilayer hBN also show two reflection minima. In all the heterostacks the electron density associated with these states is not centered in the layers, but shows as three maxima in between the layers, resembling a  $3p_z$  orbital. Independent of the orientation, the majority of the electron density is shifted towards the hBN layers, indicating that these states are hBN-specific.

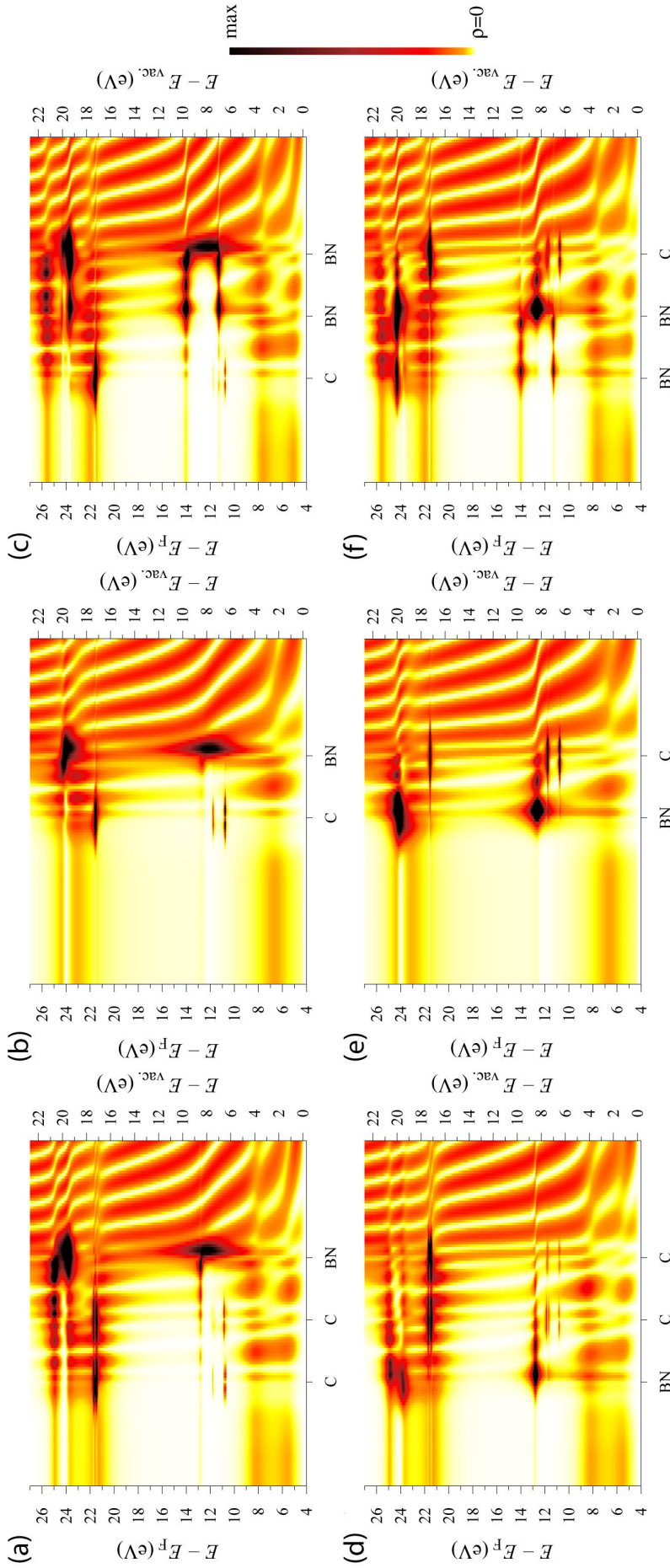


Figure 4.6: Projected electron density  $\rho$  in the LEED state for the 2Gr1hBN (a,d), 1Gr1hBN (b,e) and 1Gr2hBN (c,f) stacks. The horizontal axis is the out-of-plane dimension with the positions of the hBN layers (BN) and graphene layers (C) marked. The energy scale refers to the Fermi energy  $E_F$ , while the experimental spectra are given with respect to the vacuum level  $E_{\text{vac}} = E_F + \Phi$ , with the work function  $\Phi \approx 4.3$  eV. The electron wave is incident on the sample from the right side, thus the interference of the incident and reflected wave is visible on the right of the sample, with the wavelength shortening with increasing energy. The top row shows stacks with the hBN side facing the electron source, the bottom row shows stacks with the graphene side facing the electron source. Flipping the stack did not affect the calculated reflectivity. Calculations by E.E. Krasovskii.

The splitting of the hBN-specific state is different from the splitting of the first interference state at 3 eV. This is seen in the energy width of the minima, which is much narrower than for the interference states, and the fact that the minima do not split further for more than two layers of hBN. The calculated band structure of the graphene/hBN superstructure by Hibino et al. [12] (1Gr1hBN, Figure 4.3a) already shows the state at 11 eV, but it does not affect electron reflectivity as it has practically zero dispersion, so the electrons cannot couple into the state. For multilayer hBN, the bands are dispersive, and thus show up in the electron reflection spectra as minima.

Thirdly, the calculations show that the broad reflection minimum at 17 to 22 eV ( $\approx E_F + 21$  to 26 eV) consists of multiple minima that shift and split depending on the composition of the heterostack. The individual minima and maxima are not resolved in the experiment as inelastic scattering is large at these high energies. The range of these combined bands is indicated in the Figure 4.5 by dotted lines in the respective color at 50% reflectivity. Inelastic scattering shortens the lifetime of the state and thus broadens it in energy. The sharpest minimum followed by a maximum at  $\sim 21.5$  eV, which are too narrow to be measured, is caused by the formation of the first-order diffraction beams.

The shift of this broadened band, as marked by the dotted lines at 50% reflectivity, follows the same systematics as in the experiment: it shifts to lower energy for the addition of graphene and to higher energy for the addition of hBN. However, the shift between the 2Gr1hBN and the 1Gr2hBN stack is only 0.8 eV, compared to  $\sim 3$  eV in the experiment (c.f. Fig. 4.3b). We attribute this to inelastic scattering, which is not included in the calculation, and the resulting short inelastic mean free path (IMFP). In LEEM, the probing depth is limited to the order of the IMFP (which we will see is less than 1 layer at this high energy), thus the spectrum will be dominated by the material the electrons are first incident on – in this case the hBN. The LEEM spectrum at this energy thus resembles the bulk hBN spectrum (see Fig. 4.3) more than the lossless calculation.

This reasoning of finite probing depth is supported by the electron density plots (Fig. 4.6). The lower energy state ( $E_F + 21.5$  eV) making up this broad reflection minimum is centered in the graphene layers, while the higher energy states ( $E_F + 23.5$  to 26 eV) are dominant around the hBN layers, independent of heterostack composition and side of electron incidence. Including inelastic losses, we can thus expect to probe more of the states closer to the incidence side of the LEEM electrons. The graphene-dominated states are centered in the layer, with two side-lobes in between two layers, while the highest energy ( $E_F + 25$  to 26 eV) hBN-dominated state has 4 density maxima in between the layers, like non-overlapping  $3p_z$  orbitals around each layer. In the trilayer stacks (Fig. 4.6a,c,d,f) the lower hBN-dominated/heavy state ( $E_F + 24.2$  eV in Fig. 4.6f and  $E_F + 23.7$  eV in the other trilayers) is centered in the outermost hBN layer and avoids the graphene layers.

#### 4.2.4 Elastic and inelastic mean free paths

A quantitative understanding of the elastic and inelastic MFP can be gained from fitting the toy model to the data. For this, the effective mass in the dispersion relation was first adapted to match the first-order interlayer state between the model and the reflection data. To give an

intuition for the spectra produced by the interference toy model, we plot the reflection and transmission spectra calculated for constant reflectivity  $r^2=0.2$  and a loss factor  $\beta$  exponentially decreasing with wavevector  $k$  (see Fig. 4.7a-b, including caption). The hBN-specific state around 10 eV is not accounted for in this simple model, as it is not an interference state and already exists in the monolayer [21] (see Fig. 4.6).

The calculation of MFPs is done for the experimental spectra taken in the original orientation of the sample, for the areas with a monolayer of graphene below and one, two, and three layers of hBN on top. For comparison, also the monolayer graphene data from Chapter 3 is included. Fitting the parameters  $r$  and  $\beta$ , in the toy model to the reflectivity and transmissivity at each energy and layer count yields the parameters shown in Figures 4.7 c and d. In this fit, we apply the same  $r$  and  $\beta$  for graphene and hBN. As the fit has zero degrees of freedom, the best fit matches the data. Later, we will change the toy model to include different parameters for different layers.

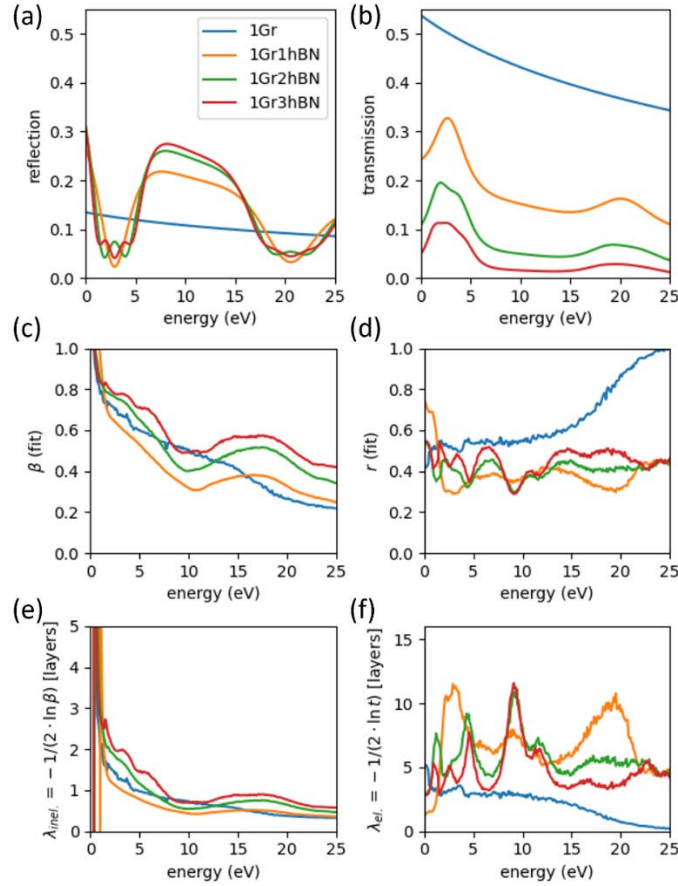


Figure 4.7: The reflection (a) and transmission (b) spectra for the toy model used at fixed  $r^2 = 0.2$  and exponentially decreasing  $\beta$  do not account for the hBN-specific band around 10 eV. Fit parameters  $\beta$  (c) and  $r$  (d) obtained by fitting the model (for each energy independently) to the hBN-on-graphene heterostack data, in analogy to the analysis in chapter 3. The inelastic MFP (e) and elastic MFP (f) are obtained from the fit parameters.

The inelastic and elastic MFPs (Figure 4.7 e and f) are calculated from the fit parameters via  $1/\lambda_{inel.} = -2 \ln \beta$  and  $1/\lambda_{el.} = -2 \ln t$  with  $t^2 = 1 - r^2$ . Generally, the inelastic MFP is

found to decrease with energy from approximately 3 layers at 1 eV to 0.5-1 layers at 25 eV, with a broad minimum around 10 eV (except for monolayer graphene). Alike other features discussed before, this minimum shifts to lower energy with increasing number of hBN layers (best visible in the plot of  $\beta$ ). While the low-energy interferences are invisible in the 1Gr1hBN and 1Gr2hBN inelastic MFPs, meaning that the interferences are well accounted for in the toy model, the 1Gr3hBN inelastic MFP does show remnants of the three-fold split minimum. In fact, the minima are sharper in the data than in the toy model. As the spacing of the split minima is connected to the broadness of the band in the A- $\Gamma$  direction, this means our toy dispersion relation  $E(k)$  is not rising steep enough in this region.

The elastic MFPs of all the graphene-hBN heterostacks are larger than the one of monolayer graphene throughout the 2-25 eV energy range, with maxima of about 10 layer counts (Fig. 4.7f). Like in the 1Gr3hBN inelastic MFP curve, some remnants of the interference minima below 5 eV mismatching the toy model are visible in the elastic MFP curve.

In Fig. 4.7f), the hBN-specific band shows up as a maximum in the elastic MFP of all the heterostacks. For 2 and 3 layers of hBN on graphene two distinct, sharp maxima (that match well between the two curves) at 8 eV ( $\sim 12$  layer counts high) and 12 eV ( $\sim 7$  layer counts high) are visible. For the 2 and 3 layers of hBN on graphene the peak at 8 eV is the global maximum. It can be expected that this feature corresponding to the hBN specific band shows up as a maximum in MFP, as it is not accounted for in the toy model. In fact, the associated reflection maximum falls into the maximum region of the toy model visualized in Figure 4.7a. Still, our method correctly assigned it to an elastic feature, as it should, being a band structure feature rather than an inelastic feature. In a modified toy model, one could retrieve the 10 eV hBN-specific band as a beating pattern between a boron and a nitrogen layer of different electron-optical density, i.e., different effective electron mass. That way, the increased inelastic MFP at that energy would be absorbed into the model.

#### 4.2.5 Symmetry upon flipping the sample

Finally, we turn to the (transmission) data gathered on the flipped sample. Although the geometry presents some problems to the electron-optical alignment as discussed before, we can discuss the effect of reversing the direction of travel of the electrons through the sample. Firstly, we highlight that reversing the direction of the incoming electrons, as sketched in Figure 4.8, is not exactly the same as time-reversal. When we reverse time in the scattering experiment, it would look like the reflected electron beam and the transmitted electron beam are travelling towards the sample and interfere to create the incoming electron beam. This would not see a reflected beam on the other side of the sample, as it is the case for reversing the sample.

For the case without inelastic scattering or loss, however, the transmitted and reflected electron flux in the flipped sample should follow time-reversal symmetry. The solution of the [time-independent] Schrödinger equation for the right-incident electron beam can be constructed from a linear combination of the stationary state solution of the left-incident electron beam and its complex conjugate. An instructive calculation found in [28,29] shows, that the wave-function transmissivity is the same and the reflectivity only differs by a phase-factor upon flipping the incoming electron direction, for an arbitrary potential going to vacuum level at a finite distance

from the sample. I.e., we expect that the real-valued transmissivity  $T$  and reflectivity  $R$  of electrons is the same for the flipped sample.

In practice, we will have to consider inelastic scattering as well. In that case, an asymmetric sample with thickness larger than or comparable to the MFP will not show the same reflectivity on both sides. Think of a silicon chip with a typical thickness of  $\sim 1$  mm with graphene deposited on one side. On that side, we would expect to measure a graphene signal in LEEM, whilst only a Si signal is expected at the other side.

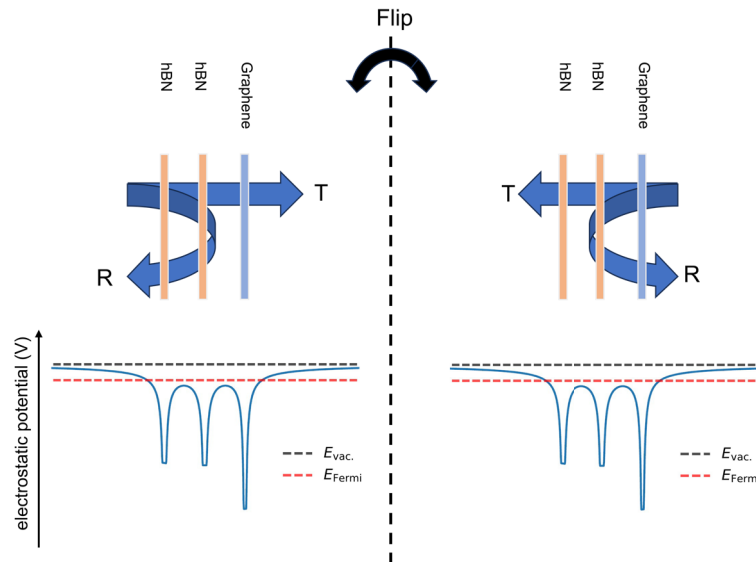


Figure 4.8: Illustration of the electrostatic potential the electron experiences upon reflection/transmission. Flipping the sample is the same as reversing the direction of the incoming electrons. The question is: Does the reflected/transmitted electron flux depend on the direction of travel of the electron?

To get a proper intuition for the problem, we again use the interference toy model introduced in Chapter 3. This model can easily be modified to allow for different reflectivity  $r$  (and the connected transmissivity  $t$ ), loss factor  $\beta$  and phase propagation  $\varphi$  (caused by thickness or effective electron mass) in the hBN and graphene layers. The transmission and reflection resulting from changes in (combinations of) these parameters are shown in Figures 4.9 and 4.10 and discussed below.

Firstly, we set the parameters for reflectivity  $r$ , the connected transmissivity  $t$ , and loss factor  $\beta$  are to different values for hBN and graphene layers, while the phase propagation is kept the same for both hBN and graphene. For the graphene layer we choose the same values as in Figure 4.7 a/b, but for hBN, we choose  $r_{\text{hBN}}^2 = 2 \cdot r_{\text{Gr}}^2$  and  $\beta_{\text{hBN}} = \sqrt{\beta_{\text{Gr}}}$ , i.e., a doubled electron reflectivity and a doubled inelastic MFP. In Figure 4.9 we show the resulting curves. Clearly, upon reversing the order of layers, the transmission spectra stay the same, as expected. However, while the reflection spectra show the same qualitative features related to interlayer resonances, there is a clear difference between both symmetries. The features measured with graphene at the LEEM-lens side (top side) are much sharper than for the flipped configuration.



The reason for that is that the electron interaction with the underlying layers is diminished by the higher  $r$  and  $\beta$  in the hBN layer.

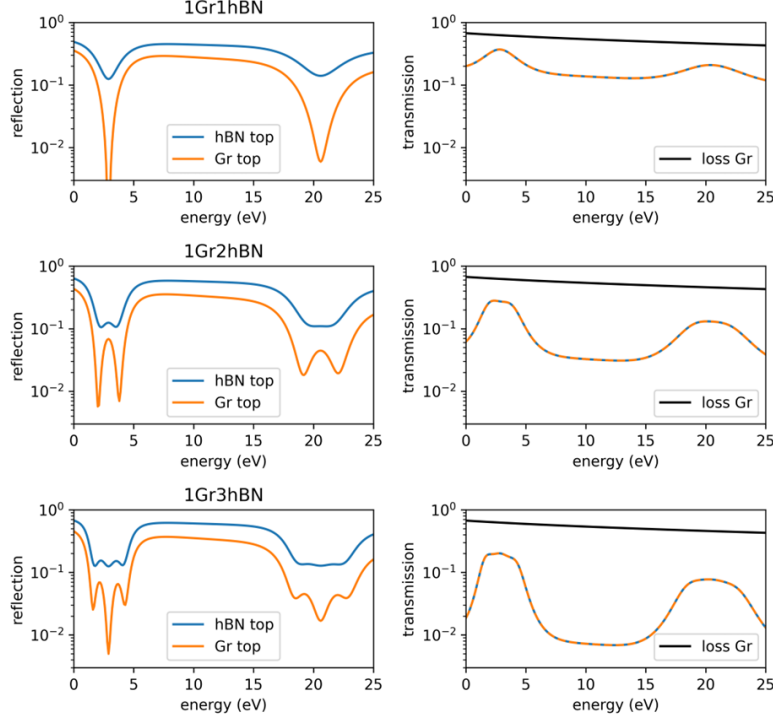


Figure 4.9: Calculated toy-model reflection and transmission spectra for multiple hBN layers on top of one graphene layer (blue) and the flipped stack (orange). Calculation where graphene and hBN are assumed to have different inelastic MFP and reflectivity, while the phase propagation over a unit cell is kept the same. The reflected spectrum changes upon flipping the sample, while the transmitted spectrum is invariant (dashed lines). The chosen energy dependent intensity loss factor  $\beta^2$  for graphene is plotted in black.

Next, we also change the phase propagation  $\varphi$ , while keeping all other parameters ( $r$  and  $\beta$ ) the same as in Figure 4.9. In Figure 4.10, the phase propagation  $\varphi_{hBN}$  in hBN is altered from the phase propagation in the graphene layers by calculating  $\varphi_{hBN}$  for a hBN layer spacing that is 1% thinner than that of graphene. This emulates the difference of out-of-plane lattice vector, that is  $\sim 1\%$  between hBN and graphene [30]. These modifications do result in different transmission curves upon flipping the sample, as shown in Fig. 4.10. In fact, the transmission maxima are shifted now, albeit only by a small amount. The reflection minima however move significantly by  $\sim 1$  eV. Also, the series of minima for 1Gr2hBN and 1Gr3hBN are not symmetric any longer (cf. Fig. 4.9), with the lower-energy minima diving lower in the case of Gr topped stacks. This may be expected, as the split minima are more hBN-like or more graphene-like, and we set the IMFP in hBN to be twice the value in graphene. As a larger IMFP increases the number of elastic reflections (comparable to an increased finesse in an optical cavity), a larger IMFP will lead to sharper interference features. E.g., for 2Gr1hBN (in the original hBN-on-top configuration), the central reflectivity maximum is formed by the minimum of the underlying 2Gr (i.e., zero in wave function) not destructively interfering with the wave reflected from the top 1hBN. Equivalently, one can think of it as the result of the top 1Gr1hBN layer minimum not interfering with the reflection from the bottom 1Gr layer. Then

the minima on either side of that maximum are more influenced by either the interference of the wave reflected from the 2Gr interfering with the wave reflected from the 1hBN or the wave reflected from the final Gr layer and 1Gr1hBN on top.

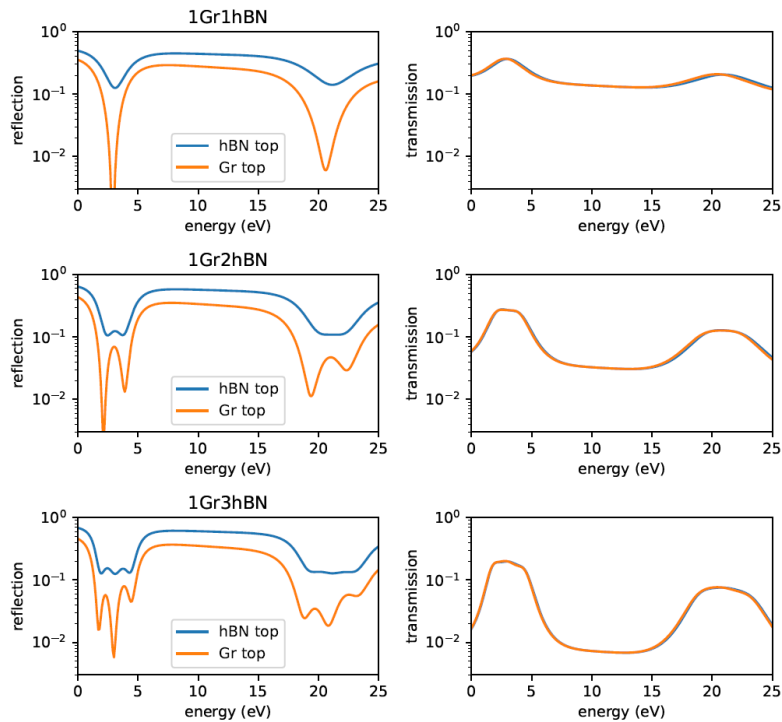


Figure 4.10: Calculated toy-model reflection and transmission spectra for multiple hBN layers on top of one graphene layer (blue) and the flipped stack (orange). In addition to the loss and reflectivity changed in Figure 4.7, the phase propagation is calculated for a 1% thinner hBN unit cell. The transmission spectra show a slight shift in flipping the sample and the split reflection minima lose their symmetry.

Having considered these models for transmission and reflection of flipped samples, and concluding that flipping the sample should have little influence on the transmission, we revisit the experimental transmission data in Figure 4.2 d/f. While the transmitted electron flux is in the same range for both orientations, the flipped sample is more transmissive in the thicker 1Gr2hBN area than in the thinner 1Gr1hBN area over the large 1 to 6 eV energy range. This unexpected peculiarity is present throughout the flipped sample, as shown in the real space images in Figure 4.11. This increased transmissivity cannot be explained in any of the previous modifications of the toy model.

Hence, our data are most probably influenced by the experimental setup used and specifically by the supporting TEM grid chosen. The graphene-hBN sample is suspended over the  $2\ \mu\text{m}$  holes on a 70 nm thick SiN membrane, that is flat on the top but recessed  $200\ \mu\text{m}$  into the frame from the bottom side [16]. The measurement setup has a much stronger electric field of  $\sim 10\ \text{kV/mm}$  on the LEEM side than on the eV-TEM side, with  $\sim 50\ \text{V/mm}$ , leading to highly distorted equipotential lines in the flipped sample, where the recessed holes point to the LEEM side. While we expect that the field strengths are not sufficient to significantly gate the sample (which is barely possible in vacuum), we expect distortions of the electron paths, focusing the



(incoming) electron bundle. Furthermore, we know that due to the described challenges to alignment in the flipped sample, the electrons were not measured at straight incidence and exit angle. In a band structure picture, this means the measurements display a contour/cut along a path in  $E - k_{\parallel}$  space that is not the  $k_{\parallel} = 0$  cut, i.e., not the cut along the  $\Gamma$  symmetry axis. In case that cut is (partially) following the parabolic-like band dispersion, this can explain the broad energy range with high transmissivity.

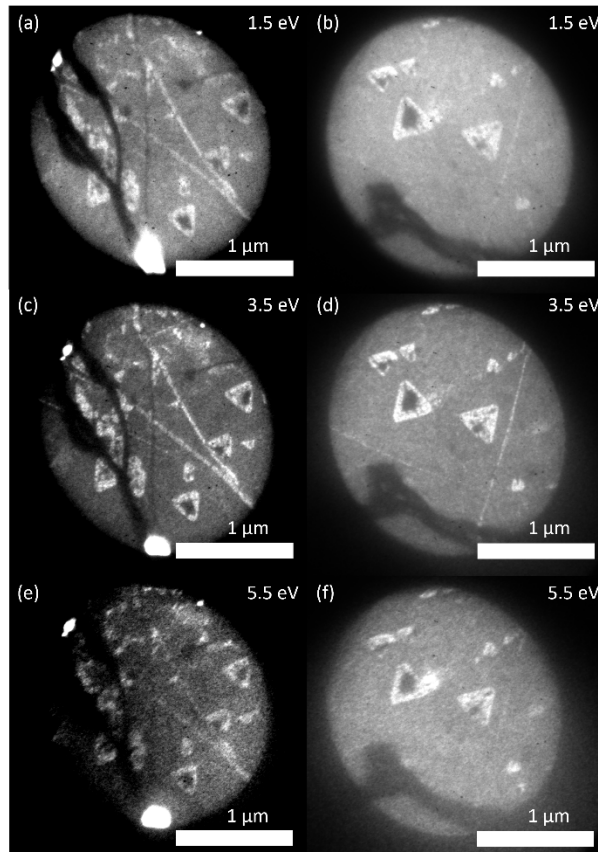


Figure 4.11: eV-TEM images of two areas of the flipped sample. The triangles with an additional hBN layer are more transmissive than the thinner 1Gr1hBN areas surrounding them over an unexpectedly broad energy range (also see Figure 4.2 f). Symmetry considerations for the graphene-hBN stack do not allow for this difference in transmissivity upon flipping the sample, so the difference must be sought in the geometry of the sample, including the TEM grid, and the resulting asymmetric electric fields.

Finally, practical implications of the sample preparation are likely to increase the transmissivity in the hBN-triangle areas. The additional layer increases the stiffness and likely the flatness in the triangle area. A flatter surface is expected to have higher coherence of the reflected and transmitted wave function, thus improving the interference conditions.

### 4.3 Conclusion

To conclude, we have shown how the low electron energy reflectivity and transmissivity spectra of a freestanding graphene-hBN heterostructure depend on both the layer count and the order

of the layers. As these areas are independent of substrate influences, they are especially suited for comparison to theory. The interlayer states splitting around 1-4 eV show that there is a direct interaction of the graphene and hBN layers that is predicted in our interference toy model. Hence, contamination between both layers must be minimal.

While the bands of hBN at energies below 5 eV (and above the vacuum level) can be explained in analogy to graphene, one cannot neglect the hBN-specific band around 10 eV that builds up with increasing hBN layer count. If one does not incorporate it in the interference toy model, the band shows up as an increase in elastic MFP in the fitted MFPs.

While the differences between reflection from the graphene and the hBN side of the heterostack are captured in the toy model, the differences in the transmission curves measured are stronger than explainable in the toy model. While the electron transmission and reflection coefficients in fully elastic scattering from a potential are invariant under flipping the electron direction, the introduction of loss in the toy model allows for asymmetry, albeit small in transmission for realistic reflection and loss coefficients.

Our research shows, that there is likely interaction with the hBN substrate in many prepared vdW samples, at least at the energies we probe. The graphene-hBN heterostacks measured may in turn serve as high-transmissivity substrates for eV-TEM investigation of layers that grow better on hBN than graphene, e.g., pentacene [31], or be used to encapsulate a sample in between. Improvements to the measurement, especially in the flipped-sample geometry, may come from additional alignment degrees of freedom of the eV-TEM gun. Adding a deflector to control the incidence angle of the eV-TEM electron bundle would allow for angle-resolved transmitted-electron spectra measurements, complementary to ARRES and ARPES.

## Appendix

### Sample fabrication

The sample is prepared by applying the polymer-free transfer method [13] to graphene and hBN. The steps are illustrated in Figure 4.A1.

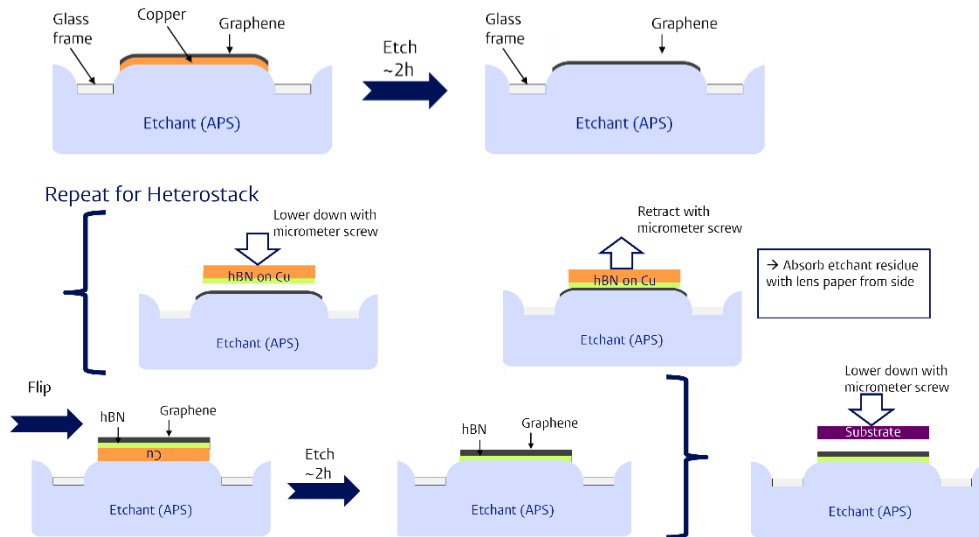


Figure 4.A1: Sample fabrication for a hBN on graphene heterostructure on a TEM grid (substrate).

The first step is the same as for the graphene on TEM grid samples.

0. Gently place a square glass frame (6 mm x 6 mm inner square) on top of the 0.5 M ammonium persulfate (APS) solution. The frame is only floating due to surface tension, thus curving the etchant surface.
1. Cut a 5 mm x 5 mm square of flat graphene on copper (round scalpel blade) and place it on top of the APS inside the glass frame.
2. Wait until the copper is fully etched away (approx. 2 h). Only the edge of the floating graphene is visible by eye, if it is not crumbled.
3. Cut a 5 mm x 5 mm square of flat hBN on copper. Fix it to a vertical micrometer screw and lower it down onto the floating graphene. After making contact, retract the screw and blot away excess APS solution droplets from the side.
4. Flip the hBN on copper, with the picked-up graphene, and float the copperside inside the glass frame.
5. Wait another 2 hours, until the copper is etched away fully.
6. Lower down the holey SiN TEM grid (sputter-coated with 5 nm Pt/Pd from each side) by a micrometer screw, until it is in contact with the floating hBN/graphene stack. Move the micrometer screw with the TEM grid attached to the side and retract it until the surface tension of the APS breaks. The connection to the TEM grid should break towards the side, to not stress the free-standing graphene-hBN membranes. Blot away excess APS droplets from the side of the TEM grid chip.

## Flipped sample

To flip the sample, it is taken out of the ESCHER setup vacuum and re-mounted in its holder. To find back the same area on the sample, it is most convenient to use eV-TEM, as the eV-TEM electron beam illuminates most of the TEM grid (compared to a few micrometers in the LEEM bundle).

The eV-TEM images at a large field of view in the usual and flipped configuration are shown in Figure 4.A2. The brightest features are holes that are not covered with graphene or hBN, thus do not impede the electrons. Especially the vertical row of uncovered holes is recognizable when identifying the same area. Other features are connected by orange arrows in Figure 4.A2. Note that the flipping the TEM grid upside down results in a mirrored image.

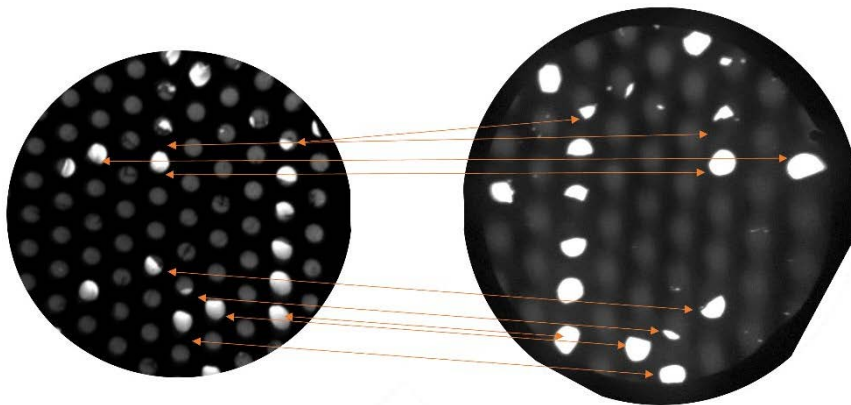


Figure 4.A2: Large-scale eV-TEM images of the same sample area in the original (a) and flipped (b) orientation. Some select features are highlighted in both images, to show the symmetry. Like when flipping an overhead projector transparency upside down, the outlines are mirrored.

## Free-standing hBN

In addition to the graphene-hBN heterostructure, we also prepared a sample with only hBN [15] on a TEM grid. A LEEM image of that sample is shown in Figure 4.A3. The hBN areas that are supported by the Pt/Pd coated TEM grid are possible to image, as they can drain the LEEM electrons that are absorbed. As hBN is an insulator, the free standing hBN areas accumulate charges as soon as the LEEM electron bundle illuminates them.

In Figure 4.A3 the sample was moved to the right in two steps, thus the part on the right has been exposed to the electron beam for longer. Whereas the free-standing part on the left can still be imaged in LEEM, the central part has charged up so far, that the incident electrons at 14.4 eV are repelled before they reach the sample. Thus, the holes in the center appear to be in mirror mode. The hBN on the middle hole is starting to rip.

The hBN on the holes on the right, that has been exposed to the LEEM electron bundle for the longest, has ripped, under the force of the accumulated charge in the LEEM magnetic field. For an estimate of the mechanical breaking strength of hBN see [32].

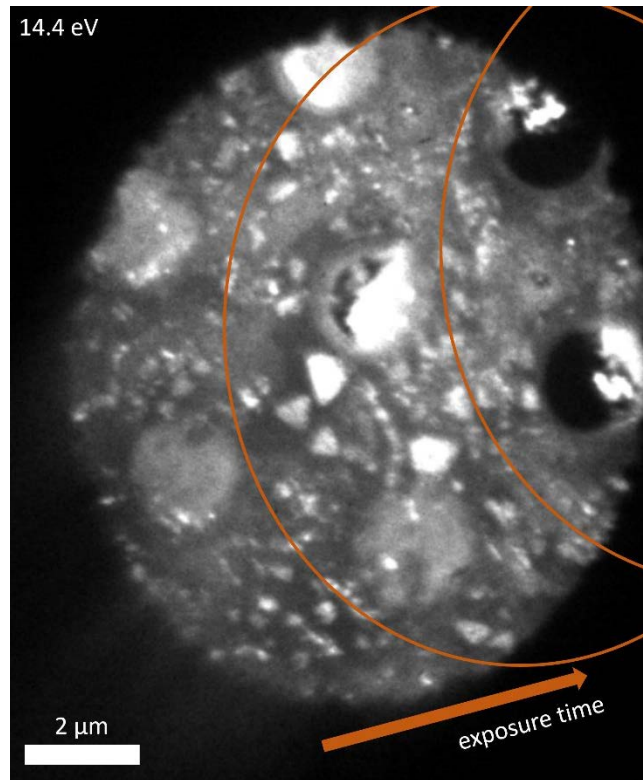


Figure 4.A3: LEEM image of hBN (mostly monolayer grown on Cu) on top of a Pt/Pd coated TEM grid. On the free-standing areas the electrons cannot be drained, as hBN is an insulator, an effect known as charging. After a few seconds of exposure to the electron beam, the free-standing hBN deforms and finally rips. The sample was moved under the beam from right to left, meaning that the free-standing hBN on the left has been exposed the longest and is starting to rip.

## References

- [1] A.K. Geim, I. V Grigorieva, Van der Waals heterostructures., *Nature* 499 (2013) 419–25. <https://doi.org/10.1038/nature12385>.
- [2] A. Ramasubramaniam, D. Naveh, E. Towe, Tunable band gaps in bilayer transition-metal dichalcogenides, *Phys. Rev. B - Condens. Matter Mater. Phys.* 84 (2011) 1070–1075. <https://doi.org/10.1103/PhysRevB.84.205325>.
- [3] J. Wang, F. Ma, W. Liang, M. Sun, Electrical properties and applications of graphene, hexagonal boron nitride (h-BN), and graphene/h-BN heterostructures, *Mater. Today Phys.* 2 (2017) 6–34. <https://doi.org/10.1016/j.mtphys.2017.07.001>.
- [4] C.R. Dean, A.F. Young, I. Meric, C. Lee, L. Wang, S. Sorgenfrei, K. Watanabe, T. Taniguchi, P. Kim, K.L. Shepard, J. Hone, Boron nitride substrates for high-quality graphene electronics, *Nat. Nanotechnol.* 5 (2010) 722–726. <https://doi.org/10.1038/nnano.2010.172>.
- [5] L. Wang, I. Meric, P.Y. Huang, Q. Gao, Y. Gao, H. Tran, T. Taniguchi, K. Watanabe, L.M. Campos, D.A. Muller, J. Guo, P. Kim, J. Hone, K.L. Shepard, C.R. Dean, One-Dimensional Electrical Contact to a Two-Dimensional Material, *Science* (80-. ). 342 (2013) 614–617. <https://doi.org/10.1126/science.1244358>.
- [6] L. Martini, V. Mišeikis, D. Esteban, J. Azpeitia, S. Pezzini, P. Paletti, M.W. Ochapski, D. Convertino, M.G. Hernandez, I. Jimenez, C. Coletti, Scalable High-Mobility Graphene/hBN Heterostructures, *ACS Appl. Mater. Interfaces* 15 (2023) 37794–37801. <https://doi.org/10.1021/acsami.3c06120>.
- [7] Y. Cao, V. Fatemi, S. Fang, K. Watanabe, T. Taniguchi, E. Kaxiras, P. Jarillo-Herrero, Unconventional superconductivity in magic-angle graphene superlattices, *Nature* 556 (2018) 43–50. <https://doi.org/10.1038/nature26160>.
- [8] R.M. Torres-Rojas, D.A. Contreras-Solorio, L. Hernández, A. Enciso, Band gap variation in bi, tri and few-layered 2D graphene/hBN heterostructures, *Solid State Commun.* 341 (2022) 114553. <https://doi.org/10.1016/j.ssc.2021.114553>.
- [9] J. Jung, A.M. Dasilva, A.H. Macdonald, S. Adam, Origin of band gaps in graphene on hexagonal boron nitride, *Nat. Commun.* 6 (2015) 1–11. <https://doi.org/10.1038/ncomms7308>.
- [10] P.S. Neu, D. Geelen, R.M. Tromp, S.J. van der Molen, Extracting transverse electron mean free paths in graphene at low energy, *Ultramicroscopy* 253 (2023) 113800. <https://doi.org/10.1016/j.ultramic.2023.113800>.
- [11] J. Jobst, A.J.H. van der Torren, E.E. Krasovskii, J. Balgley, C.R. Dean, R.M. Tromp, S.J. van der Molen, Quantifying electronic band interactions in van der Waals materials using angle-resolved reflected-electron spectroscopy, *Nat. Commun.* 7 (2016) 13621. <https://doi.org/10.1038/ncomms13621>.
- [12] H. Hibino, S. Wang, C.M. Orofeo, H. Kageshima, Growth and low-energy electron microscopy characterizations of graphene and hexagonal boron nitride, *Prog. Cryst. Growth Charact. Mater.* 62 (2016) 155–176. <https://doi.org/10.1016/j.pcrysgrow.2016.04.008>.

- [13] X. Zhang, C. Xu, Z. Zou, Z. Wu, S. Yin, Z. Zhang, J. Liu, Y. Xia, C. Te Lin, P. Zhao, H. Wang, A scalable polymer-free method for transferring graphene onto arbitrary surfaces, *Carbon* N. Y. 161 (2020) 479–485. <https://doi.org/10.1016/j.carbon.2020.01.111>.
- [14] Graphene Laboratories, Single layer h-BN (Boron Nitride) Film grown on Copper Foil, (2022). <https://www.graphene-supermarket.com/products/single-layer-h-bn-boron-nitride-film-grown-on-copper-foil-2-x-1> (accessed May 28, 2022).
- [15] Graphenea, Monolayer Graphene on Cu, (2020). <https://www.graphenea.com/collections/buy-graphene-films/products/monolayer-graphene-on-cu-4-inches?variant=276514394> (accessed November 7, 2023).
- [16] Ted Pella Inc., PELCO® Silicon Nitride Support Films for TEM, Prod. Overv. (2011). [https://www.tedpella.com/grids\\_html/silicon-nitride-hole.aspx](https://www.tedpella.com/grids_html/silicon-nitride-hole.aspx) (accessed November 2, 2023).
- [17] S. Chen, M. Horn Von Hoegen, P.A. Thiel, M.C. Tringides, Diffraction paradox: An unusually broad diffraction background marks high quality graphene, *Phys. Rev. B* 100 (2019) 1–6. <https://doi.org/10.1103/PhysRevB.100.155307>.
- [18] M.K.L. Man, S. Deckoff-Jones, A. Winchester, G. Shi, G. Gupta, A.D. Mohite, S. Kar, E. Kioupakis, S. Talapatra, K.M. Dani, Protecting the properties of monolayer MoS<sub>2</sub> on silicon based substrates with an atomically thin buffer, *Sci. Rep.* 6 (2016) 1–9. <https://doi.org/10.1038/srep20890>.
- [19] P.C. Mende, Q. Gao, A. Ismach, H. Chou, M. Widom, R. Ruoff, L. Colombo, R.M. Feenstra, Characterization of hexagonal boron nitride layers on nickel surfaces by low-energy electron microscopy, *Surf. Sci.* 659 (2017) 31–42. <https://doi.org/10.1016/j.susc.2017.02.004>.
- [20] L. Schué, L. Sponza, A. Plaud, H. Bensalah, K. Watanabe, T. Taniguchi, F. Ducastelle, A. Loiseau, J. Barjon, Bright Luminescence from Indirect and Strongly Bound Excitons in h-BN, *Phys. Rev. Lett.* 122 (2019). <https://doi.org/10.1103/PhysRevLett.122.067401>.
- [21] C. Herrmann, P. Omelchenko, K.L. Kavanagh, Growth of h-BN on copper (110) in a LEEM, *Surf. Sci.* 669 (2018) 133–139. <https://doi.org/10.1016/j.susc.2017.11.021>.
- [22] H. Hibino, H. Kageshima, F. Maeda, M. Nagase, Y. Kobayashi, Y. Kobayashi, H. Yamaguchi, Thickness Determination of Graphene Layers Formed on SiC Using Low-Energy Electron Microscopy, *E-Journal Surf. Sci. Nanotechnol.* 6 (2008) 107–110. <https://doi.org/10.1380/ejssnt.2008.107>.
- [23] D. Geelen, J. Jobst, E.E. Krasovskii, S.J. van der Molen, R.M. Tromp, Nonuniversal Transverse Electron Mean Free Path through Few-layer Graphene, *Phys. Rev. Lett.* 123 (2019) 086802. <https://doi.org/10.1103/PhysRevLett.123.086802>.
- [24] T.A. de Jong, T. Benschop, X. Chen, E.E. Krasovskii, M.J.A. de Dood, R.M. Tromp, M.P. Allan, S.J. van der Molen, Imaging moiré deformation and dynamics in twisted bilayer graphene, *Nat. Commun.* 13 (2022). <https://doi.org/10.1038/s41467-021-27646-1>.
- [25] E.E. Krasovskii, Augmented-plane-wave approach to scattering of Bloch electrons by an interface, *Phys. Rev. B* 70 (2004) 245322. <https://doi.org/10.1103/PhysRevB.70.245322>.

- [26] E. Krasovskii, Ab Initio Theory of Photoemission from Graphene, *Nanomaterials* 11 (2021) 1212. <https://doi.org/10.3390/nano11051212>.
- [27] Y. Malozovsky, C. Bamba, A. Stewart, L. Franklin, D. Bagayoko, Accurate Ground State Electronic and Related Properties of Hexagonal Boron Nitride (h-BN), *J. Mod. Phys.* 11 (2020) 928–943. <https://doi.org/10.4236/jmp.2020.116057>.
- [28] K. Konishi, G. Paffuti, The Schrödinger equation, in: *Quantum Mech.*, Oxford University Press Oxford, 2009: pp. 49–88. <https://doi.org/10.1093/oso/9780199560264.003.0003>.
- [29] G.D. Mahan, 10. Scattering Theory, in: *Quantum Mech. a Nutshell*, Princeton University Press, 2009: pp. 320–351. <https://doi.org/10.1515/9781400833382-011>.
- [30] J. Wang, F. Ma, M. Sun, Graphene, hexagonal boron nitride, and their heterostructures: properties and applications, *RSC Adv.* 7 (2017) 16801–16822. <https://doi.org/10.1039/C7RA00260B>.
- [31] A. Tebyani, Probing molecular layers with low-energy electrons, *Casimir PhD series*, 2024, <https://doi.org/1887/3721791>.
- [32] A. Falin, Q. Cai, E.J.G. Santos, D. Scullion, D. Qian, R. Zhang, Z. Yang, S. Huang, K. Watanabe, T. Taniguchi, M.R. Barnett, Y. Chen, R.S. Ruoff, L.H. Li, Mechanical properties of atomically thin boron nitride and the role of interlayer interactions, *Nat. Commun.* 8 (2017) 1–9. <https://doi.org/10.1038/ncomms15815>.





# 5 ELECTRON TRANSMISSION AND MEAN FREE PATH IN MOLYBDENUM DISULFIDE AT ELECTRON VOLT ENERGIES

## Abstract

In van der Waals (vdW) materials, the electron mean free path (MFP) is largely influenced by the discrete states in the unoccupied band structure. So far, the influence of these states has only been measured in graphene, while all measurements on other vdW materials lack energy resolution. Here, we present reflection and transmission spectra of freestanding, few-layered molybdenum disulfide ( $\text{MoS}_2$ ) samples in the 0-55 eV electron range. Our measurements reveal states of enhanced electron transmissivity above the vacuum level, that correspond to the (unoccupied) density of states. We also show a full quantum mechanical calculation that confirms a good understanding of the elastic scattering in  $\text{MoS}_2$ . A model is developed to extract the inelastic MFP spectrum, which is a measure of the inelastic scattering cross section. As  $\text{MoS}_2$  is a complicated system of different atomic planes, we expect that our methods generalize well to other van der Waals materials and heterostacks thereof.

---

P. S. Neu, M. Šiškins, E. E. Krasovskii, R. M. Tromp, and S. J. van der Molen, *Electron Transmission and Mean Free Path in Molybdenum Disulfide at Electron-Volt Energies*, Phys. Rev. B **107**, 075427 (2023).

## 5.1 Introduction

The electron mean free path (MFP) is a material-specific quantity, describing the decay length of an electron beam through a material at a specific electron energy. Especially the MFP of low-energy electrons is important, as it affects the probing depth and damage in scanning electron microscopy (SEM) as well as the exposure of resists in electron beam lithography. While the mean free path of electrons through bulk solids has been researched for more than a century, it has barely been studied in the comparably new class of van der Waals materials. Moreover, subtle energy-dependent features, intimately related to the unoccupied electron band structure, have generally been missed due to a lack of energy and momentum resolution.

For many different solids, the electron MFP has been measured over a large energy range and determined to roughly follow the same U-shape curve, the so-called universal curve [1], which has a minimum around 30 eV, but is otherwise featureless. Fewer reports are available for layered materials, especially in the low-energy range. For graphene, the most popular van der Waals material, the low-energy MFP has been reported to be in the order of a few layers based on Electron Energy Loss Spectroscopy (EELS) [2], measurements of the secondary electron spectrum generated in a SEM [3] and by photoemission [4]. Recently, our group has demonstrated a more direct method to extract the MFP from a combination of low energy electron microscopy (LEEM) and electron Volt-transmission electron microscopy (eV-TEM) [5,6]. In contrast to the ‘universal’ curve, our study on few-layer graphene showed multiple maxima and minima depending on layer count. These features are related to (unoccupied) interlayer electron bands that are typical of van der Waals materials. For the case of graphene, these can be understood within a relatively simple model of Fabry-Pérot-like electron interference between the consecutive layers, leading to well-defined electron transmission resonances [7–10].

In this contribution, we use this new methodology, i.e., the combination of LEEM and eV-TEM, to study MoS<sub>2</sub>, a member of a more complicated and diverse group of two-dimensional materials: the transition metal dichalcogenides (TMDs). The different TMDs are closely related in crystallographic structure, every layer consisting of a plane of transition metal atoms sandwiched between two chalcogen atom (S, Se, Te) planes. However, TMDs show significant variation in their electric properties. Molybdenum disulfide (MoS<sub>2</sub>) is a promising TMD, having a band gap in the visible to IR range, making it suitable for photovoltaic applications. Remarkably, the band gap is indirect for multilayer MoS<sub>2</sub>, whereas it becomes direct for monolayer MoS<sub>2</sub>. The chemical and semiconducting properties of MoS<sub>2</sub> make it a popular substrate for (high-energy) TEM analyses of catalysis [11, 13–16]. The only low-energy transmissivity measurements reported so far have been performed with the ‘virtual substrate’ method [26], i.e., by secondary electrons emitted from underlying substrates.

## 5.2 Experiment

Here we report and analyze electron reflectivity and transmissivity spectra of the 2H polytype of MoS<sub>2</sub> in the low energy (0 - 55 eV) range, obtained by LEEM and eV-TEM. We demonstrate that the energy dependent structure observed is convincingly explained from the distribution of unoccupied electron states above the vacuum energy. From the combination of these reflection

and transmission spectra, we deduce unique information on the elastic and inelastic scattering electron path lengths within MoS<sub>2</sub> vs. energy.

For our experiments, a thin flake of exfoliated MoS<sub>2</sub> (2H polytype) was transferred using the all-dry viscoelastic method [11] onto a silicon nitride TEM grid (PELCO® Holey Silicon Nitride, 2.5 μm holes (optical images in the supplemental information [12], Fig. 5.S1) that had been sputter-coated with 5 nm Pt/Pd to improve conductivity. The sample was gently annealed by laser heating (808 nm, 10.7 W, approx. 300° C) in the UHV sample chamber of the LEEM instrument. In aberration-corrected LEEM mode [13] we image the sample using low energy electrons specularly reflected from the sample (see sketch in Fig. 5.1c). For eV-TEM, we use a second electron source behind the sample to form transmission images of low energy electrons transmitted without scattering and/or energy loss [5,6]. As both methods are available in the same instrument, we can image the same sample area in both reflectivity and transmissivity, so that they can be readily and directly compared. To illustrate this, a transmission image (eV-TEM) of MoS<sub>2</sub> on the holey SiN is shown in Fig. 5.1a. In Fig. 5.1b, we show the same image, but with a reflection (LEEM) image pasted on top of the eV-TEM image, so as to demonstrate its position. To obtain detailed spectral information, we scan the energy of the electrons incident on the sample in the range from 0 to 55 eV in steps of 0.1 eV and record images in both transmission and reflection at each energy. The energy resolution of the spectra is limited by the energy spread of the respective electron guns, i.e., 0.3 eV for the cold field emission gun in LEEM and 0.8 eV for the thermal Barium Oxide emitter in eV-TEM. Note that in both LEEM and eV-TEM a contrast aperture in the diffraction plane has been inserted around the specular spot, so contributions of inelastically and/or diffusely scattered electrons and higher order diffraction spots are blocked.

### 5.3 Results

The eV-TEM image, Fig. 5.1a, shows three different layer counts in the flake. (Note that the 50 nm thick TEM grid support is fully blocking the low-energy electrons outside the holey structure). While the thinnest area of the flake is most transmissive, the area on the left edge is not transmissive enough to allow distinguishing the holes in the underlying grid. Throughout the whole energy range the thinnest part is most transmissive and the thickest part is least transmissive, which is as one may expect in a system dominated by inelastic scattering. The LEEM image in Fig. 5.1b shows some contamination of the sample, supposedly with residues from the preparation process. These contaminants cluster together upon the first illumination with the electron beam, which is common for polycarbonate residues from the exfoliation and stamping process. It stands out that the areas of lower layer count are less contaminated, which indicates that either the sticking coefficient is lower on these surfaces or that the contaminants diffused in between layers. Averaged over the area of one covered hole, the contaminants reduce the reflected intensity by ~25% throughout the considered energy range compared to small pristine areas.

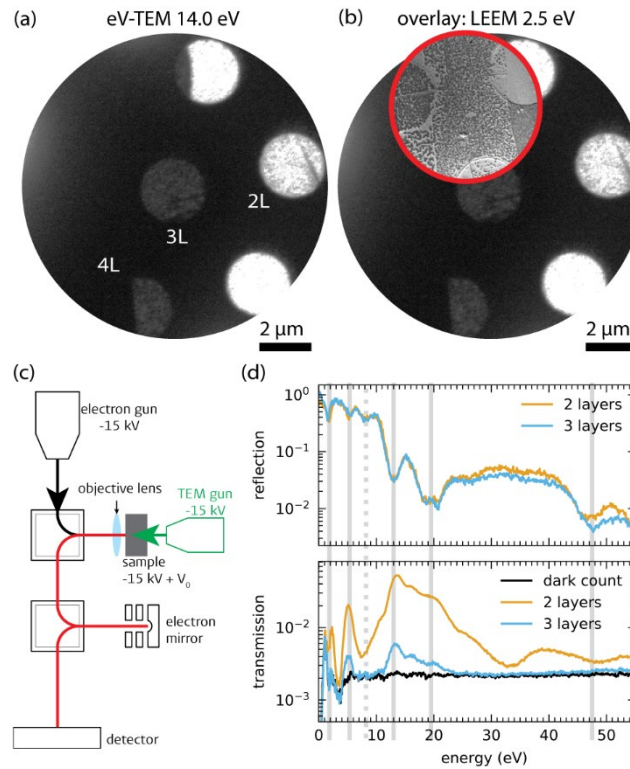


Figure 5.1: (a) eV-TEM image of 2, 3 and 4 layer (labeled 2L, 3L and 4L) MoS<sub>2</sub> flake covering a grid of holes, acquired by transmitted low-energy electrons. In (b), a smaller scale reflection image (LEEM) is shown, placed on top of the transmission image in (a) to pinpoint its position. (c) shows the low energy electron microscope (LEEM) setup with the additional electron gun behind the sample used for eV-TEM. (d) Reflection and transmission spectra of the bi- and trilayer areas. The lines mark the minima in reflectivity, i.e., states above the vacuum level where one expects corresponding transmission maxima at the same energy.

The reflection and transmission data sets of images recorded at 0-55 eV allow us to select areas of a specific layer count and extract the corresponding spectra. We have chosen flat, freestanding areas and for each energy have averaged over a circular area that almost fills a TEM grid hole. Figure 5.1d displays the spectra obtained, which have all been normalized to the incoming electron flux. For completeness, Figure 5.1d also displays the dark count (DC), which was extracted from an area on the TEM grid support blocking all electrons. The transmission spectrum of the four-layer area is not shown, as it is not distinguishable from the dark count. The dark count is caused by the microchannel plate used to amplify the electron signal: bright features, here predominantly the uncovered TEM grid holes, will ‘bleed’ into the adjacent detector area. The apparent features in the dark count spectrum are thus an artifact of the automatic adaptive gain of the channel plate [14] that prevents overexposure of the brightest features in the image. For the analysis following, we therefore subtracted the energy-dependent dark count from the transmission spectra.

In Fig. 5.1d, a set of characteristic reflectivity minima are shown, marked by vertical lines. Their positions are consistent with previous reports on MoS<sub>2</sub> [15,16]. Furthermore, they are consistent with calculations of the projected Density of (unoccupied) States (pDOS, [12] Fig. 5.S2): The projected bands at the  $\Gamma$  point, i.e., at zero in-plane momentum, coincide with the

reflection minima (transmission maxima) at the same energy. Indeed, an incoming electron resonant with an unoccupied state has a strongly enhanced probability of propagating into the material, leading to a minimum in reflectivity, and a maximum in transmission. In general, the electron reflectivity will thus depend on the dispersion of the states, i.e. on their energy vs. in-plane  $k$ -vector, as given by the pDOS and as demonstrated by recent angle-resolved reflected-electron spectroscopy (ARRES) [10]. In the LEEM and eV-TEM experiments reported here, the electrons are incident and detected exclusively along the surface normal, thus probing the electronic band structure at the  $\Gamma$  point only. (Off-normal reflected/transmitted electrons are filtered out by the contrast aperture.)

Of special importance is that all reflectance spectra recorded show a dip around 5.4 eV. This dip is absent in monolayer MoS<sub>2</sub>, as calculations and previous experiments [15] show (see also below). We conclude that all areas of the sample are at least 2 layers thick, although we had optically preselected the thinnest MoS<sub>2</sub> flakes during sample preparation. Whereas the study in reference [15] could only probe the electron reflectivity, the current study also employs eV-TEM to measure the transmissivity of the same sample area. The high transmissivity of the thinnest area strongly suggests that we are looking at 2, 3 and 4 layers of MoS<sub>2</sub>.

Let us now look at Fig. 5.1d in more detail. It shows a rather broad window of maximum transmissivity at a remarkably high energy range, i.e., from 10 to 25 eV. This feature is in sharp contrast to the simple case of graphene where the highest transmissivity is below 5 eV. We will discuss this phenomenon in more detail below. Furthermore, Fig. 5.1d shows that the maxima in transmission align with the minima in reflection, as illustrated by the vertical lines. This is exactly what a simple resonant theory, in which atomic layers act as ‘semi-transparent’ mirrors would yield: at resonance, there will be constructive interference for forward propagation (transmission) and destructive interference in backward propagation [5]. However, such a simple model will not suffice here as it cannot explain all features. The reflection maximum at 10 eV, for example, comes with a shoulder in transmission, on the flank of some broader feature. Furthermore, the reflection minimum at 8.2 eV (dashed vertical line) has no corresponding feature in transmission. We will attribute the latter to strong inelastic scattering at this particular energy (see below).

To gain further insight into the nature of the electron reflection and transmission, we calculated electron scattering by 1, 2 and 3 layers of MoS<sub>2</sub> using the *ab initio* method based on Bloch-waves developed in ref. [17]. Its application to an isolated slab is described in ref. [18]: In the scattering region the wave function is a linear combination of the eigenfunctions of an auxiliary three-dimensional periodic crystal, which contains the TMD sandwich as part of the unit cell. The Bloch eigenfunctions of the auxiliary crystal are obtained in terms of augmented plane waves, see refs. [17,18]. Inelastic scattering was taken into account by the optical potential, which increases smoothly with energy as calculated for the similar TMD, tungsten diselenide (WSe<sub>2</sub>), in ref. [19] within the *GW* approximation based on a full energy and momentum dependent *ab initio* dielectric function of WSe<sub>2</sub>.

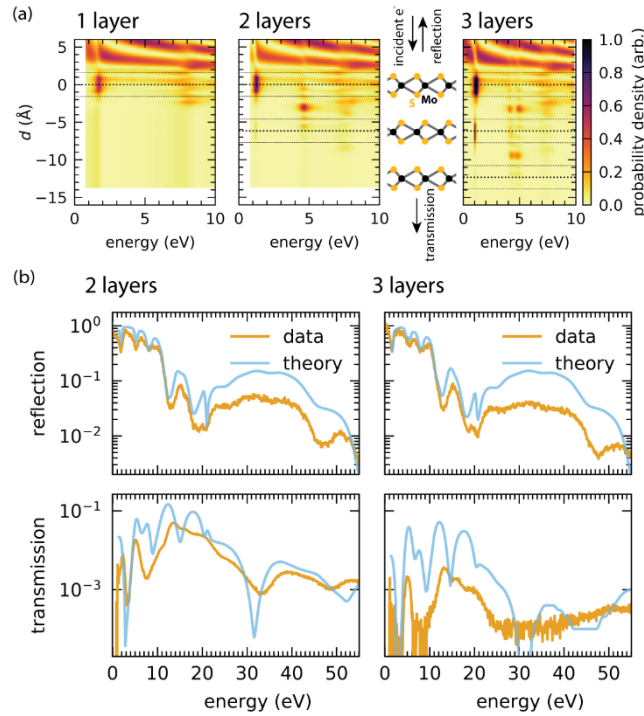


Figure 5.2: (a) Calculated probability density along the out-of-plane direction for an electron wave incident from the top for 1, 2 and 3 layers of MoS<sub>2</sub>, with the Mo and S planes marked as dotted lines. (b) Comparison of the recorded reflection and transmission (dark count subtracted) spectra and the calculated values. The features of the reflection curves match well. The experimental transmission spectrum appears more broadened as discussed in the text.

Figure 5.2a shows the solution to the scattering problem for an electron plane wave that is at normal incidence on the layers of MoS<sub>2</sub> from the top side and is partially reflected and partially transmitted. Note that it is the electron probability density that is plotted. Inside the material, the electron density shows where the electronic states are localized, whereas on the top vacuum side we see the interference of the incoming wave with the reflected wave. The electron wavelength in vacuum shortens with increased energy, as is seen in the interference between the incoming and reflected wave in front of the material.

Let us next focus on the (unoccupied) states involved (see Fig. 5.2a). The resonance at 1 eV has its highest electron density within the layers, while the resonance at 4 - 5 eV, which is characteristic of the multilayer ( $n > 1$ , absent in the monolayer), is centered between the layers. This interlayer resonance, around 4.5 eV for the bilayer, splits into two resonances for the trilayer, in theory causing a splitting of the reflection minimum as in graphene, but that is beyond the spectral resolution of our measurement. The electron density is not symmetrical but shifted towards the side of the incoming electrons. For example, the state at 1 eV has most of the electron density centered around the first layer, and it considerably decreases towards the second or even the third layer. Similarly, in the 3-layer case the interlayer state at 4 - 5 eV has a higher electron density between the first and second layer than between the second and third layer. The fact that the electron density is shifted towards the side of the incoming electrons intuitively explains why the reflection spectra of two and three layer MoS<sub>2</sub> largely coincide.

We note that the reflectivity and transmissivity spectra shown in Figure 5.2b are calculated for the specular beam. This was done to make them comparable to the measurement, where a diffraction-space aperture was placed around the (0,0) beam. To mimic the resolution of our instrument, the theoretical spectra were broadened by a Gaussian function with a FWHM of 0.3 eV and 0.8 eV for LEEM and eV-TEM, respectively. For the reflectivities, the measured features match the calculations very well. The fact that the measured reflectivity is lower than calculated is at least in part caused by the contaminants discussed above.

For the transmissivity spectra the calculated and measured spectra show qualitative correspondence, although there are clear differences. For example, the transmission intensity measured is generally lower than predicted by calculation, although still of the same magnitude. We relate this to contamination on the sample surface. In general, the energies of the transmission maxima and minima in experiment and theory match rather well, although the peaks and dips are less pronounced in the experiment. For example, the sharp minimum and maximum at a few eV as well as the large window of enhanced transmissivity from 10 eV to 25 eV reproduce for both the bilayer and the trilayer. But there is a clear outlier: a transmission maximum at 8 eV is calculated but not observed. This peak may be suppressed by inelastic loss processes [20,21]. The dip in reflectivity is less affected by inelastic loss, as neither electrons that are transmitted elastically nor electrons that scatter inelastically contribute to the reflectivity.

The LEEM-IV and eV-TEM spectra broaden with increasing energy, an effect that has also been observed for multilayer graphene [7,22]. We relate this to an increased loss in each layer, comparable to how the finesse in a Fabry-Pérot resonator [23] decreases when the reflectivity of the mirrors goes down. As the lifetime of an electron in an unoccupied state decreases, the spectral features broaden. These losses could be due to inelastic scattering, that generally increases with energy as more scattering paths become available, or due to increased elastic scattering out of the aperture. Note that increasing loss effects as a function of energy are also incorporated in our first principles calculations via an energy-dependent optical potential.

As introduced above, the transverse electron mean free path of graphene has been determined by direct [5] and more indirect methods, like photoemission [4], TOF of secondary electrons [24] and deconvolution of EELS spectrum [2]. Although the effects of multiple scattering increase the MFP if one also counts the distance travelled within the zig-zag path [25], in the case of MoS<sub>2</sub> the transmissivity is so low that we can make the approximation to neglect multiple scattering. This leads to the following simple model. Let us define  $R(E)$  as the fraction of electrons reflected at an energy  $E$ . Then  $1-R(E)$  is the percentage of electrons travelling into the material. The share of electrons that are actually transmitted through the material,  $T(E)$ , is then equal to  $(1-R(E))$  attenuated by the losses within the film due to scattering within the two or three layers of MoS<sub>2</sub>, respectively. With the thickness  $d$  (in layers), the transmissivity can hence be written as:

$$T(E) = (1 - R(E)) \cdot \exp(-d/\lambda(E)) \quad (1)$$

where  $\lambda(E)$  is the energy-dependent (inelastic) electron MFP. Note that the reflectivity  $R(E)$  in this model is independent of layer count. This is justified by the reflection data shown in Fig.



5.1d. Applying this model for  $d=2$  layers, we obtain the MFP vs. energy curve shown in Figure 5.3a, which is between 0.3 and 0.7 layers, or 1.8 Å to 4.3 Å.

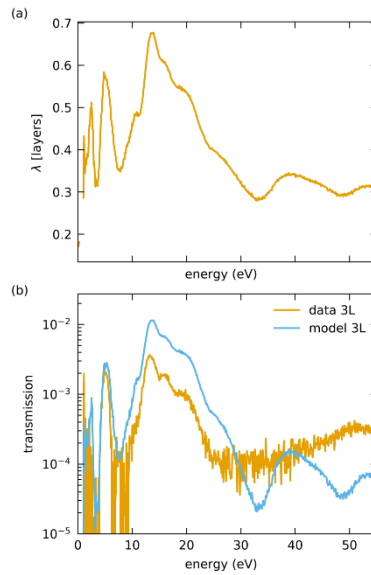


Figure 5.3: (a) From the reflectivity and transmissivity observed in the 2 layer data, we calculate the mean free path  $\lambda$ . Using the extracted  $\lambda$  in a simple model to predict the transmissivity (b) of the 3 layer sample yields reasonable agreement with the measured spectra.

To check for consistency, we take the  $\lambda(E)$  function obtained for the 2-layer case and calculate what should come out for the 3-layer case. In other words, we insert  $\lambda(E)$  back into eq. 1, together with the 3 layer  $R(E)$  function, and subsequently set  $d$  to 3 layers. The transmissivity function calculated this way (Fig. 5.3b) follows the measured one quite well up to an energy of 25 eV. At higher energies the transmissivity is somewhat lower for the 3-layer data (until the noise of  $10^{-4}$  dominates the spectrum). We relate this to the somewhat higher contamination observed on the surface of the trilayer.

## 5.4 Discussion

Next, we compare our data to the measurements of low-energy MFP by Da et al. [26] who employ the ‘virtual substrate’ method. They report significantly larger MFP values of 15 – 30 Å for bilayer  $\text{MoS}_2$  ([12], Fig. 5.S3). Accordingly, they also report a larger transmissivity of 45% - 60%. We propose that this significant difference of an order of magnitude is inherent to the different measurement techniques: In the virtual substrate method, the incident electrons, i.e., the secondary electrons emitted from the virtual substrate, are non-directional, so even after diffuse and/or inelastic scattering they contribute to the measured signal. In contrast, in our eV-TEM method, a collimated beam of electrons is incident on the sample, and measures have been taken to filter out all electrons that have been scattered diffusely and/or inelastically. The contamination of the sample discussed above only has a minor effect, since assuming a 25% higher value for  $T(E)$  increases the calculated MFP by less than 1 Å.

Da et al. also report a large window of increased MFP at 7-50 eV. This would correspond to what we see in the range 8-50 eV in Fig. 5.3a, if one were to consider that the dip in MFP

around 32 eV is not visible in their data due to a decreasing signal-to-noise ratio. Also, the MFP maxima at 2.3 eV and 5 eV cannot be distinguished in their measurements, which may be related to the lack of collimation of the secondary electron probe beam. Importantly, the unoccupied bands have a dispersion depending on electron momentum, which will further blur the features [9]. Hence, from the experimental side there are differences in methodology and hence in measurement resolution.

## 5.5 Summary

To summarize, we have studied electron transmission through MoS<sub>2</sub> and have directly obtained the mean free path as a function of electron energy,  $\lambda(E)$ , in the 0-55 eV energy range. This demonstrates that we can extend the methodology we previously applied to graphene [5,6] to the more complex TMDs. In contrast to graphene, the maximum transmissivity is found in a large window at 10-25 eV, rather than at energies below 5 eV. As for graphene, the transmission maxima found experimentally can be related to (resonant) electronic states within the MoS<sub>2</sub>, as obtained by calculations. However, in a more complicated system such as MoS<sub>2</sub>, these states are not limited to simple interlayer resonances. Note that in contrast to EELS, which measures the strength of inelastic scattering as a function of energy loss, the inelastic mean free path extracted here is a direct measure of the energy-dependent scattering cross section as a function of initial electron energy.

Having demonstrated our methodology for a rather complex system such as MoS<sub>2</sub>, we expect our methods and understanding to generalize to the other transition metal dichalcogenides and to heterostacks of van der Waals materials. In all cases, unoccupied electron states will play a large role in electron propagation and mean free paths.

## Acknowledgements

We acknowledge Herre van der Zant, Andres Castellanos-Gomez, Peter Steeneken and Martin Lee for support in preparing the samples. This research was funded by the Spanish Ministry of Science, Innovation and Universities (EK, Project No. PID2019-105488GB-I00) and the Dutch Research Council (PN, NWO Vrije Programma TNW18.071).

## Appendix

### Optical Images

Optical micrographs of the sample are shown in Figure 5.A1. All measurements reported in the main text were performed on the thin part of the MoS<sub>2</sub> flake, here towards the top of the image. Also, the TEM grid holes underneath the flake and another thicker MoS<sub>2</sub> flake to the right are visible.

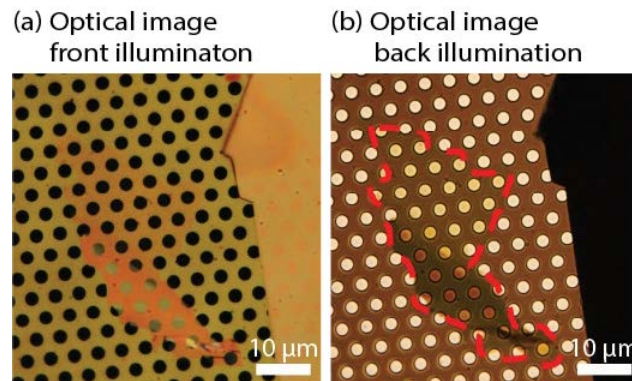


Figure 5.A1: Optical images after stamping the MoS<sub>2</sub> flake to the holey support grid. The flake is digitally outlined in the back illumination micrograph (b).

### Projected Density of States

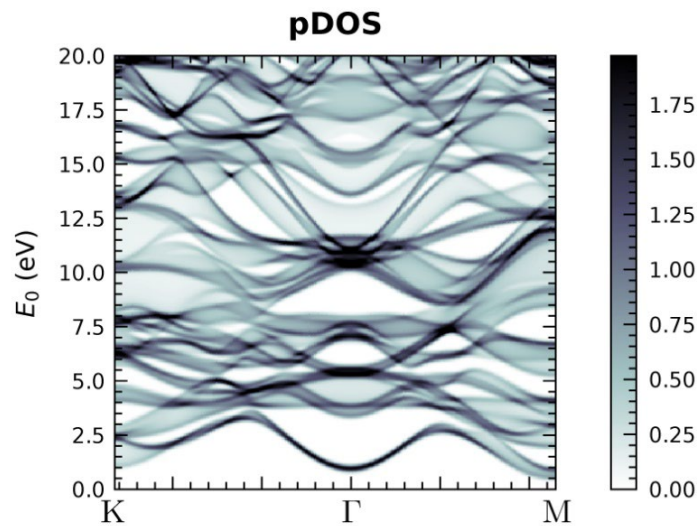


Figure 5.A2: Calculated projected Density of States (pDOS) of bulk MoS<sub>2</sub>. The energy 0 eV corresponds to the vacuum level.

The density of states (DOS) above the vacuum level is calculated and projected along the out-of-plane direction in Figure 5.A2. The LEEM and eV-TEM experiments reported in the main text probe the band structure at the  $\Gamma$  point, as only electrons at perpendicular incidence and perpendicular reflection/transmission are measured.

## Mean Free Path: comparing with previous work

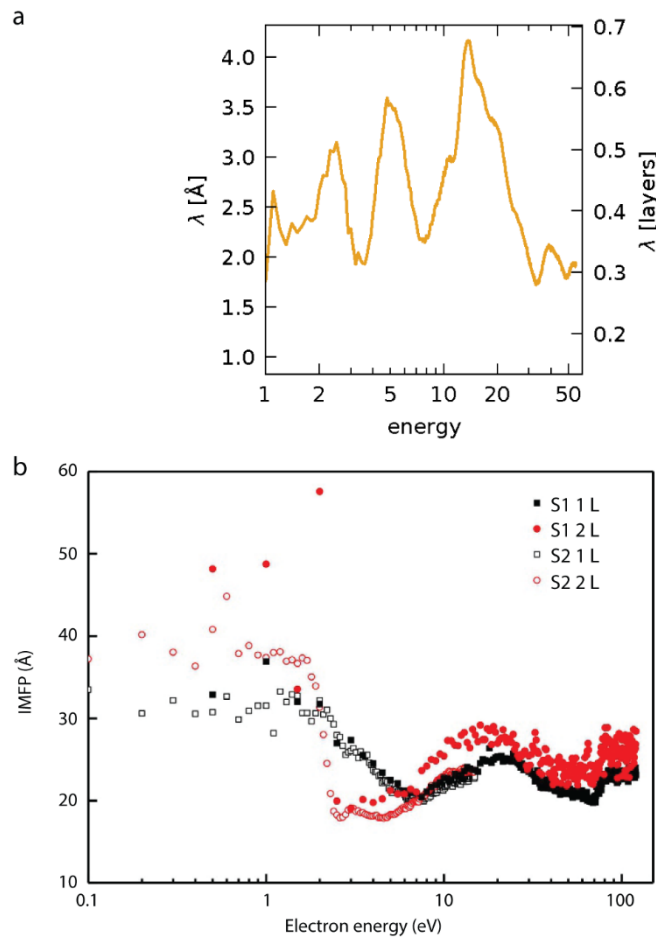


Figure 5.A3: Inelastic Mean Free Paths (IMFP) obtained (a) from the combination of LEEM and eV-TEM measurements (main text, eq. 1) compared to (b) results obtained by Da et al. by the virtual substrate method. Plot (b) is reproduced from [26].

Both methods of obtaining the IMFPs yield comparable key features in bilayer MoS<sub>2</sub> (Fig. 5.A3, a, red curves in b). Foremost, the broad IMFP maximum from 8 – 30 eV is reproduced in both methods. Also, the maximum at 5 eV in (a) may be visible in measurement S1 2L (b).

The most striking difference is the scale of the IMFPs obtained: 2 - 4 Å in our experiment and 15 - 30 Å reported by Da et al. This may be explained by the different momentum distributions of the electrons used in the two experiments: While the electrons in our experiment have close to zero in-plane momentum (with respect to the sample) when entering and exiting the material, the photoelectrons used in the virtual substrate method have a broad distribution of in-plane momenta when incident on the MoS<sub>2</sub> and also when measured after transmission. That means that in the virtual substrate method scattering events that change the in-plane momentum of the electrons don't contribute to lowering the IMFP. The broad distribution of in-plane momenta in the virtual substrate method also explains its apparently lower resolution: The electrons probe the band structure averaged over a large part of reciprocal space (see the pDOS, Figure 5.A2), thus the discrete states at the  $\Gamma$  point shown in (a) appear broadened.

## References

- [1] M.P. Seah, W.A. Dench, Quantitative electron spectroscopy of surfaces: A standard data base for electron inelastic mean free paths in solids, *Surf. Interface Anal.* 1 (1979) 2–11. <https://doi.org/10.1002/sia.740010103>.
- [2] W.S.M. Werner, A. Bellissimo, R. Leber, A. Ashraf, S. Segui, Reflection electron energy loss spectrum of single layer graphene measured on a graphite substrate, *Surf. Sci.* 635 (2015) L1–L3. <https://doi.org/10.1016/j.susc.2014.12.016>.
- [3] O.Y. Ridzel, V. Astašauskas, W.S.M. Werner, Low energy (1–100 eV) electron inelastic mean free path (IMFP) values determined from analysis of secondary electron yields (SEY) in the incident energy range of 0.1–10 keV, *J. Electron Spectros. Relat. Phenomena* 241 (2020) 146824. <https://doi.org/10.1016/j.elspec.2019.02.003>.
- [4] A. Locatelli, G. Zamborlini, T.O. Menteş, Growth of single and multi-layer graphene on Ir(100), *Carbon N. Y.* 74 (2014) 237–248. <https://doi.org/10.1016/j.carbon.2014.03.028>.
- [5] D. Geelen, J. Jobst, E.E. Krasovskii, S.J. van der Molen, R.M. Tromp, Nonuniversal Transverse Electron Mean Free Path through Few-layer Graphene, *Phys. Rev. Lett.* 123 (2019) 086802. <https://doi.org/10.1103/PhysRevLett.123.086802>.
- [6] P.S. Neu, D. Geelen, A. Thete, R.M. Tromp, S.J. van der Molen, Complementary LEEM and eV-TEM for imaging and spectroscopy, *Ultramicroscopy* 222 (2021) 113199. <https://doi.org/10.1016/j.ultramic.2020.113199>.
- [7] H. Hibino, H. Kageshima, F. Maeda, M. Nagase, Y. Kobayashi, Y. Kobayashi, H. Yamaguchi, Thickness Determination of Graphene Layers Formed on SiC Using Low-Energy Electron Microscopy, *E-Journal Surf. Sci. Nanotechnol.* 6 (2008) 107–110. <https://doi.org/10.1380/ejsnt.2008.107>.
- [8] R.M. Feenstra, M. Widom, Low-energy electron reflectivity from graphene: First-principles computations and approximate models, *Ultramicroscopy* 130 (2013) 101–108. <https://doi.org/10.1016/j.ultramic.2013.02.011>.
- [9] J. Jobst, J. Kautz, D. Geelen, R.M. Tromp, S.J. van der Molen, Nanoscale measurements of unoccupied band dispersion in few-layer graphene, *Nat. Commun.* 6 (2015) 8926. <https://doi.org/10.1038/ncomms9926>.
- [10] J. Jobst, A.J.H. van der Torren, E.E. Krasovskii, J. Balgley, C.R. Dean, R.M. Tromp, S.J. van der Molen, Quantifying electronic band interactions in van der Waals materials using angle-resolved reflected-electron spectroscopy, *Nat. Commun.* 7 (2016) 13621. <https://doi.org/10.1038/ncomms13621>.
- [11] A. Castellanos-Gomez, M. Buscema, R. Molenaar, V. Singh, L. Janssen, H.S.J. van der Zant, G.A. Steele, Deterministic transfer of two-dimensional materials by all-dry viscoelastic stamping, *2D Mater.* 1 (2014) 011002. <https://doi.org/10.1088/2053-1583/1/1/011002>.
- [12] See Appendix for optical images, the calculated projected Density of States and the mean free path compared to previous experimental work.

- [13] R.M. Tromp, J.B. Hannon, A.W. Ellis, W. Wan, A. Berghaus, O. Schaff, A new aberration-corrected, energy-filtered LEEM/PEEM instrument. I. Principles and design, *Ultramicroscopy* 110 (2010) 852–861. <https://doi.org/10.1016/j.ultramic.2010.03.005>.
- [14] T.A. de Jong, D.N.L. Kok, A.J.H. van der Torren, H. Schopmans, R.M. Tromp, S.J. van der Molen, J. Jobst, Quantitative analysis of spectroscopic low energy electron microscopy data: High-dynamic range imaging, drift correction and cluster analysis, *Ultramicroscopy* 213 (2020) 112913. <https://doi.org/10.1016/j.ultramic.2019.112913>.
- [15] T.A. de Jong, J. Jobst, H. Yoo, E.E. Krasovskii, P. Kim, S.J. van der Molen, Measuring the Local Twist Angle and Layer Arrangement in Van der Waals Heterostructures, *Phys. Status Solidi* 255 (2018) 1800191. <https://doi.org/10.1002/pssb.201800191>.
- [16] Z. Dai, W. Jin, M. Grady, J.T. Sadowski, J.I. Dadap, R.M. Osgood, K. Pohl, Surface structure of bulk 2H-MoS<sub>2</sub>(0001) and exfoliated suspended monolayer MoS<sub>2</sub>: A selected area low energy electron diffraction study, *Surf. Sci.* 660 (2017) 16–21. <https://doi.org/10.1016/j.susc.2017.02.005>.
- [17] E.E. Krasovskii, Augmented-plane-wave approach to scattering of Bloch electrons by an interface, *Phys. Rev. B* 70 (2004) 245322. <https://doi.org/10.1103/PhysRevB.70.245322>.
- [18] E. Krasovskii, Ab Initio Theory of Photoemission from Graphene, *Nanomaterials* 11 (2021) 1212. <https://doi.org/10.3390/nano11051212>.
- [19] F. Siek, S. Neb, P. Bartz, M. Hensen, C. Strüber, S. Fiechter, M. Torrent-Sucarrat, V.M. Silkin, E.E. Krasovskii, N.M. Kabachnik, S. Fritzsche, R.D. Muiño, P.M. Echenique, A.K. Kazansky, N. Müller, W. Pfeiffer, U. Heinzmann, Angular momentum-induced delays in solid-state photoemission enhanced by intra-atomic interactions, *Science* 357 (2017) 1274–1277. <https://doi.org/10.1126/science.aam9598>.
- [20] H.C. Nerl, K.T. Winther, F.S. Hage, K.S. Thygesen, L. Houben, C. Backes, J.N. Coleman, Q.M. Ramasse, V. Nicolosi, Probing the local nature of excitons and plasmons in few-layer MoS<sub>2</sub>, *NPJ 2D Mater. Appl.* 1 (2017) 1–8. <https://doi.org/10.1038/s41699-017-0003-9>.
- [21] E. Moynihan, S. Rost, E. O’connell, Q. Ramasse, C. Friedrich, U. Bangert, Plasmons in MoS<sub>2</sub> studied via experimental and theoretical correlation of energy loss spectra, *J. Microsc.* 279 (2020) 256–264. <https://doi.org/10.1111/jmi.12900>.
- [22] D. Geelen, eV-TEM: Transmission Electron Microscopy with Few-eV Electrons, Doctoral dissertation, Leiden University, 2018. <http://hdl.handle.net/1887/63484>.
- [23] N. Ismail, C.C. Kores, D. Geskus, M. Pollnau, Fabry-Pérot resonator: spectral line shapes, generic and related Airy distributions, linewidths, finesses, and performance at low or frequency-dependent reflectivity, *Opt. Express* 24 (2016) 16366–16389. <https://doi.org/10.1364/OE.24.016366>.
- [24] I. Konvalina, B. Daniel, M. Zouhar, A. Paták, I. Müllerová, L. Frank, J. Piños, L. Průcha, T. Radlička, W.S.M. Werner, E.M. Mikmeková, Low-Energy Electron Inelastic Mean Free Path of Graphene Measured by a Time-of-Flight Spectrometer, *Nanomaterials* 11 (2021) 2435. <https://doi.org/10.3390/nano11092435>.

- [25] L.H. Yang, B. Da, H. Yoshikawa, S. Tanuma, J. Hu, J.W. Liu, D.M. Tang, Z.J. Ding, Low-energy electron inelastic mean free path and elastic mean free path of graphene, *Appl. Phys. Lett.* 118 (2021) 053104. <https://doi.org/10.1063/5.0029133>.
- [26] B. Da, J. Liu, M. Yamamoto, Y. Ueda, K. Watanabe, N.T. Cuong, S. Li, K. Tsukagoshi, H. Yoshikawa, H. Iwai, S. Tanuma, H. Guo, Z. Gao, X. Sun, Z. Ding, Virtual substrate method for nanomaterials characterization, *Nat. Commun.* 8 (2017) 15629. <https://doi.org/10.1038/ncomms15629>.

# 6 PHOTOEMISSION FROM CHIRAL MOLECULE FILMS



## 6.1 Introduction

The Chirality-Induced Spin Selectivity (CISS) effect has been investigated for both its fundamental implications and its promising applications since the first report in 1999 [1]. This first study reported an asymmetry in spin population for electrons photoemitted from films of stearoyl lysine, a chiral organic molecule. The effect is intriguing, as the degree of spin polarization found cannot be quantitatively explained by spin-orbit coupling. Calculations based on spin-orbit coupling yield a 100-1000 times lower degree of spin polarization than found in experiments [2], due to the small spin-orbit coupling parameters of the lightweight (carbon-) atoms involved. Recent studies attempt to explain the CISS effect as intrinsically related to disorder that diminishes at low temperatures [3] or by spin-dependent coherent scattering [4].

The first set of experiments by Ray et al. [1] focused on films of lefthanded (L) and righthanded (D) stearoyl lysine, five monolayers thick, and the effect of the composition of the layers on spin-selectivity. They measured the (energy-dependent) photoemission intensity from five layers of L- stearoyl lysine under illumination with left- and right-circularly polarized light (reprinted in Fig. 6.1a). They interpreted the difference in photoemissivity between left- and right-circularly polarized light as a spin-filtering effect on the electrons photoemitted from the gold substrate, which have a preferred spin depending on the handedness of the light.

Furthermore, they found that in a stack of organic films of different handedness the degree of spin polarization was only dependent on the number of layers of each handedness and not their order. The authors concluded that the organic layers act as independent spin filters with a certain spin-dependent transmission probability. For five monolayers consisting of 99% L-stearoyl lysine and 1% R-stearoyl lysine, they reported the absence of the intensity-dependence on the handedness of light (Fig. 6.1a, panel B), suggesting that spin-selectivity is a collective phenomenon in the layer.

In a later photoemission experiment, Göhler et al. [5] reported on the spin polarization of photoelectrons emitted from monolayers of DNA. They show that the spin polarization differs by a few percent between left- and right-circular polarized illumination (Fig. 6.1c), which is attributed to the spin-asymmetry in photoemission from the underlying gold. However, the CISS effect was strong enough to keep the same majority spin anti-parallel to the direction of travel, independent of laser light polarization (see Fig. 6.1c). Also, they found a difference in photoemission intensity depending on the handedness of the laser light, as reprinted in Figure 6.1b, in line with the spin-filtering effect reported previously by Ray et al. (Fig 1a).

For DNA of different lengths, Göhler et al. [5] found a spin polarization of 31% for 50 base pairs, rising to 57% (anti-parallel to the direction of travel for all lengths) for 78 base pairs of double-stranded DNA (under illumination with linearly polarized light).

Scanning probe measurements of CISS report a large site-dependence of the degree of spin-polarization [6,7]. Although the assembly of organic film aims for uniformity, one can expect the formation of defects and domains of molecules (with the same orientation), possibly producing hotspots in photoemissivity and spin selectivity.

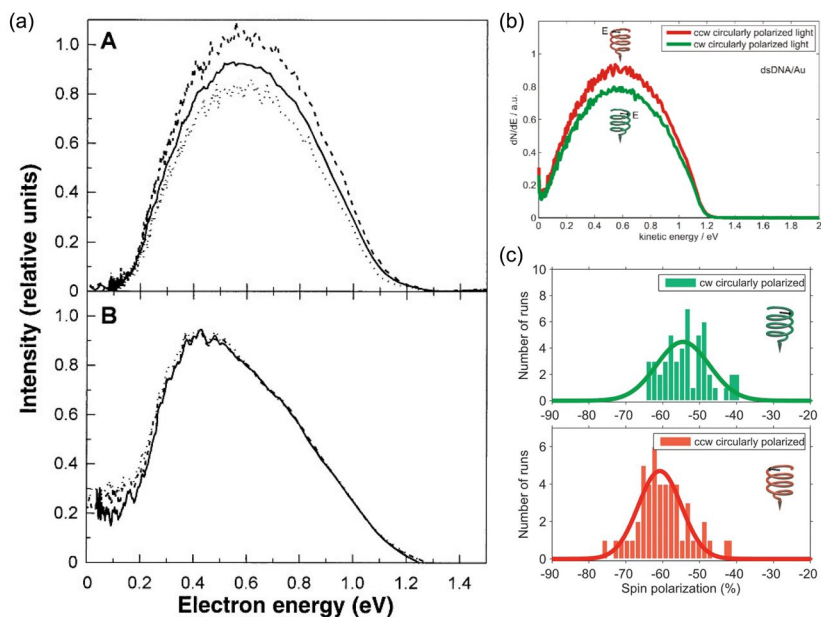


Figure 6.1: Exemplary reports of chirality-induced spin selectivity (CISS) and the accompanying intensity difference between right- and left-circularly polarized light measured in photoemission experiments. (a) Reprint of Figure 2 from Ray et al. [1] showing the electron energy distribution obtained with linearly polarized light (solid line), right-handed circularly polarized light (dashed lines), and left-handed circularly polarized light (dotted lines). The film consisted of five layers of enantiopure L-stearoyl lysine (A) and a mixture with 1% D-stearoyl lysine added (B). (b, c) Reprint of Fig. S6 and Fig. 3 from Göhler et al. [5] showing the photoemissivity intensity (b) and spin polarization (c) of double stranded DNA for right-circularly polarized light (green) and left-circularly polarized light (red). The interpretation is that chiral molecular layers act as spin filters with different transmission probabilities for the different spins emitted from the gold substrates, i.e. CISS. Reprinted with permission from AAAS.

In our experiment, we set out to use the imaging capabilities of the ESCHER setup, to acquire an image of the polarization-dependent photoemission. As we have no means of measuring spin directly in our ESCHER setup, we instead control the handedness of light and image the resulting photoemission intensity. The experiments by Ray et al. [1] and Göhler et al. [5] show that spin-selectivity goes hand in hand with the photoemission intensity dependent on handedness of light (see Fig. 6.1). The reported effect on intensity is in the order of  $\pm 10\%$  compared to the photoemission intensity under linearly polarized illumination.

We will study a sample of sulfur-functionalized R-BINAP molecules (2,2'-bis(diphenylphosphino)-1,1'-binaphthyl) on top of a 40 nm gold layer. The layered sample structure mimics the one in the photoemission experiments cited above. BINAP is a short, carbon-based molecule with a chiral center in the middle, and is commercially used for chiral synthesis. Recent studies report conductive-AFM measurements of the CISS effect in BINAP and a corresponding asymmetry in circular-dichroism over a broad DUV wavelength range [8]. As the thin chiral molecular film is prepared on top of a non-chiral layer, we will first explore the photoemission of a non-chiral substrate. To gain further understanding of the polarization control setup, we also investigate the polarization-dependent photoemission of gold

nanostructures with sizes in the order of the deep ultraviolet (DUV) wavelength. Finally, we report on the photoemission of a thin film of chiral R-BINAP molecules [9], and its dependence on the circular/elliptical polarization of the (DUV) light.

## 6.2 Experimental

### 6.2.1 Linear polarization and photoemission

In the ESCHER LEEM setup, the DUV laser beam (224 nm, HeAg70, PhotonSystems) enters the vacuum chamber through one of the fused silica viewports directed toward the sample. Unlike in the geometry used in the group of Zacharias [5,10], the light in our experiment does not hit the sample perpendicular to the surface, but under an angle of  $\Theta = 70^\circ$  from the surface normal. Thus, the incoming and reflected light rays span a plane, with different reflectivities for the linear polarization perpendicular to the plane (s polarization) and the linear polarization parallel to the plane (p polarization). The geometry of the light ray incident on the sample, together with the s and p polarization electric field components  $E_s$  and  $E_p$ , is shown in Figure 6.2. The angle enclosed by the ray and the sample is  $\alpha = 20^\circ$ .

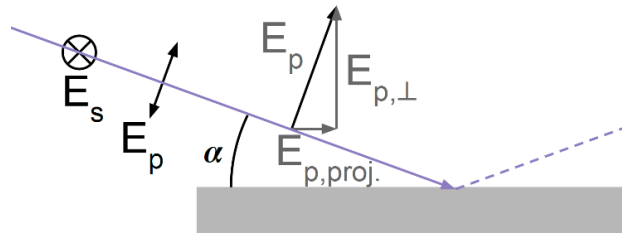


Figure 6.2: Sketch of the illumination geometry in our experiment. The DUV laser beam (violet) is incident on the sample (grey) under a sharp angle given by the setup of the vacuum chamber. Linear components of the electric field of the DUV light ray and electric fields projected on the sample are shown. The s component does not change when it is projected, as it is always perpendicular to the plane spanned by the incident and reflected light ray. The p component of the electric field is diminished when incident on the sample, with  $E_{p,proj.} = \sin(\alpha) \cdot E_p$ .

While usually the effect of linear polarization direction on light reflection (and for dielectrics transmission) is discussed, it will also have an influence on the photoemission from a non-transparent surface. In general, the photoemission intensity will depend on the band transitions in the material, which are the contrast mechanism in (polarization-dependent) ARPES of crystalline surfaces. For the gold and silicon surfaces one can expect a simple relation: The photoemission is proportional to the light that is not reflected, i.e., absorbed (assuming a bulk sample).

According to the Fresnel equations [11], the reflection coefficients of light, on the vacuum-sample interface with the complex refractive index  $n$  of the sample, are

$$R_s = \left| \frac{\cos \Theta - \sqrt{n^2 - \sin^2 \Theta}}{\cos \Theta + \sqrt{n^2 - \sin^2 \Theta}} \right|^2$$

and

$$R_p = \left| \frac{n^2 \cos \Theta - \sqrt{n^2 - \sin^2 \Theta}}{n^2 \cos \Theta + \sqrt{n^2 - \sin^2 \Theta}} \right|^2$$

for s and p polarized light, respectively, and the angle  $\Theta = 90^\circ - \alpha$  off the surface normal. Thus, the absorbed intensities are  $T_{s/p} = 1 - R_{s/p}$ .

At 224 nm wavelength and  $\Theta = 70^\circ$ , we can expect  $T_s = 0.44$  and  $T_p = 0.88$  for silicon according to the refractive index reported by Aspnes and Studna [12] and expect  $T_s = 0.32$  and  $T_p = 0.81$  for gold (Au) according to Ciesielski et al. [13], who measured a 35 nm thin Au film on  $\text{SiO}_2$ .

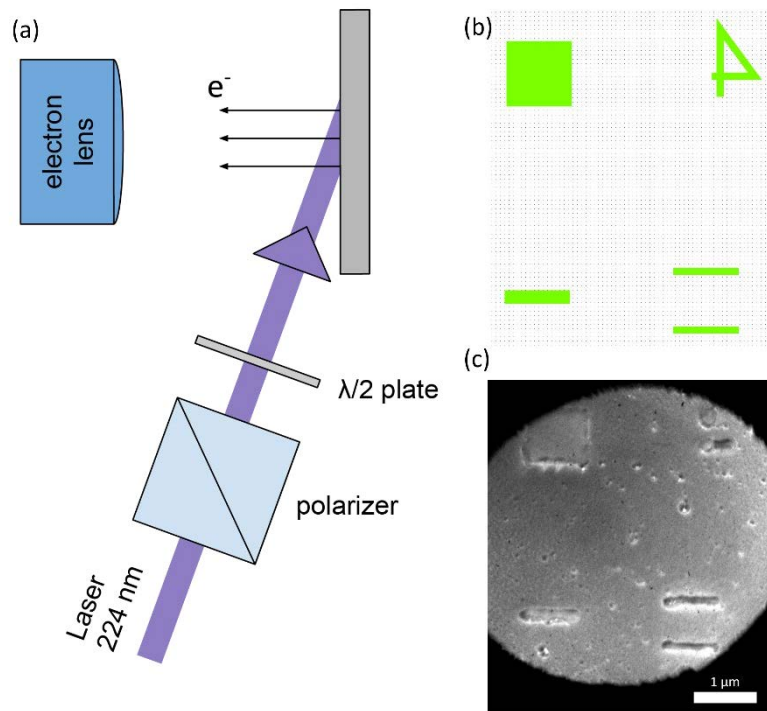


Figure 6.3: (a) The linear polarization is controlled by a polarizer (Glan-Taylor prism) and a  $\lambda/2$  plate on a motorized rotation mount outside the vacuum chamber. The sample was patterned electron-beam lithographically according to the design in (b). The LEEM image (c) at the mirror mode transition shows, that the square and lines transferred successfully, while the number 4 only shows up in a dot and a line. The raised features are made of 40 nm gold on top of a 5 nm titanium sticking layer.

The polarization control, which is attached to the outside of the vacuum viewport flange, (Fig. 6.2a) consists of a linear polarizer (Glan Taylor style prism, Thorlabs GLB10) and a  $\lambda/2$  plate (Tim optics Jena) that is rotated by a stepper motor. The laser beam is aligned onto the sample with a mirror (aluminum, DUV-enhanced mirror, Edmund optics). The mirror already introduces a partial polarization of the laser beam, due to the Fresnel equations explained earlier. The linear polarizer is kept constant during the data acquisition, as to not vary the intensity due to varying the mirror and linear polarizer axis, and the linear polarization direction is varied with the  $\lambda/2$  plate. We name the angle between the linear polarizer and the  $\lambda/2$  plate  $\Phi$ .

Turning the  $\lambda/2$  plate with respect to the linear polarizer leads to a doubling ( $2 \cdot \Phi$ ) of the polarization vector angle with respect to the lambda half plate fast (slow) axis. Aligning either the fast or slow  $\lambda/2$  plate axis with the linear polarizer, which happens every  $90^\circ$ , leads to an unchanged polarization. Therefore, the polarization vector after the  $\lambda/2$  plate, i.e., incident on the sample, is  $90^\circ$  periodic in  $\lambda/2$  plate angle.

To align the linear polarizer to the s polarization axis on the sample, we rotate the  $\lambda/2$  plate and find the angle of minimum photoemission. Then we set the linear polarizer to double the angle where that minimum was found, as the angle was doubled by the  $\lambda/2$  plate. The setting of the linear polarizer is then checked by rotating the  $\lambda/2$  plate symmetrically around the new  $\Phi = 0^\circ$  axis of the linear polarizer.

## 6.2.2 Principal tests on gold structures

To test our set-up, we first use samples that consist of a lithographically defined gold (40 nm, on 5 nm chromium) pattern (Fig. 6.3b). We acquired a LEEM image at the mirror mode transition energy and with a contrast aperture inserted (Fig. 6.3c). The size of the gold square is approximately  $1 \mu\text{m} \times 1 \mu\text{m}$  and the size of the lines is approximately  $1 \mu\text{m} \times 150 \text{nm}$  according to the LEEM image. The electron beam lithography design contained smaller structures, with four times smaller base lengths as indicated by the 4 in Figure 6.3b, which could not be found in PEEM (with the 224 nm laser or the Hg light source) or LEEM. Small structures are known to not be exposed correctly or not adhere to the substrate during the removal of the excess gold (lift-off). Alike, the number 4 in the design was too small to transfer fully, as seen in the LEEM image Figure 6.3c. The size of  $1 \mu\text{m}$  of the smallest structures produced and shown in Figure 6.3c is still comparable to 4 times the wavelength of the light used and the short dimension of the lines is smaller than the wavelength, thus can be expected to show plasmonic behavior. The lines have a characteristic aspect ratio of  $1000 \text{nm}/150 \text{nm} \approx 6.7$ .

The data in Figure 6.4 is acquired by rotating the  $\lambda/2$  plate angle in steps of  $360^\circ/64 \approx 5.6^\circ$  and integrating the image over 256 laser pulses. The integrated image is shown in the inset of Figure 6.4, with the arrow colors corresponding to the plot. First, we note that all curves in Fig. 6.4 are indeed  $90^\circ$  periodic. The substrate photoemission curve, which was used to align the linear polarizer to the s polarization and define the  $\Phi$  angle, has a minimum at  $0^\circ$ , by construction, and at multiples of  $90^\circ$ . The photoemission curve of the gold square (orange, Figure 6.4) follows the same sine-like curve, but at approximately 5 times higher intensity. Photoemission from gold is indeed expected, as the work function of gold is  $5.10 - 5.47 \text{eV}$  according to literature [14,15] (depending on facet, crystallinity, etc.), which is lower than the photon energy of  $5.54 \text{eV}$  at 224 nm wavelength. Although the work functions of the (p-doped) Si and its native silicon oxide layer are lower than that of gold, around  $5.0 \text{eV}$  [16], the Si substrate emits fewer photoelectrons than the gold. We attribute this to the lowering of the gold work function due to organic contaminations deposited during the dissolution of PMMA in acetone. Organic contamination of Au is known to further lower the work function by up to  $1 \text{eV}$  [17].

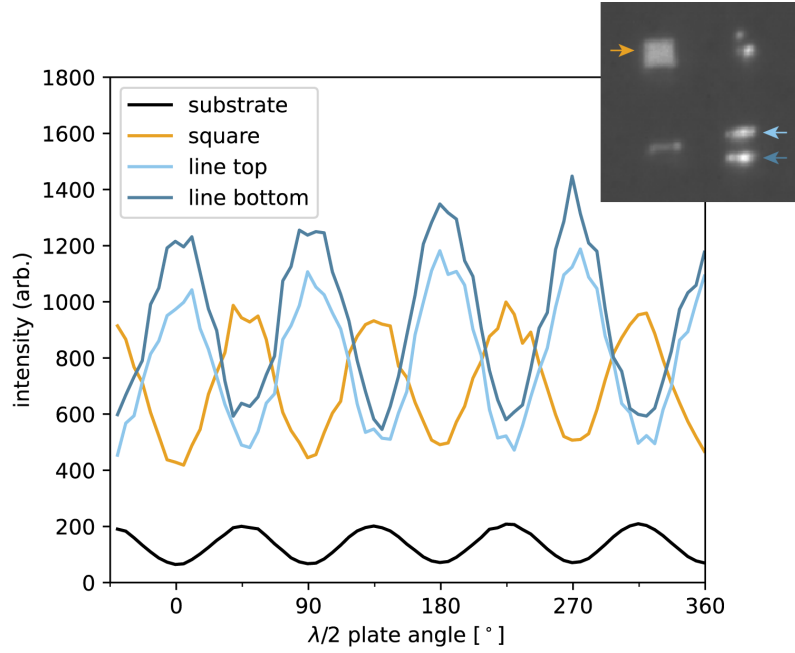


Figure 6.4: Photoemission intensity as function of  $\lambda/2$  plate angle for the features indicated in the inset. The inset shows the integrated photoemission image. The dependence of photoemission on linear polarization direction is expected as the light is incident on the surface under a sharp angle, leading to polarization-dependent reflection. All curves are  $90^\circ$  periodic in  $\lambda/2$  plate angle, as this is the periodicity of going from p-polarized to s-polarized to p-polarized linear light. The photoemissivity curve of the square is in phase with the one of the substrate, while the ones of the lines are shifted by  $45^\circ$ , pointing to a plasmonic response. Here, the maximum of photoemission occurs when the light is polarized parallel to the long direction of the lines.

The photoemission of the two gold lines (marked in blue in Figure 6.4) is shifted by  $45^\circ$  in  $\lambda/2$  plate coordinates/angle with respect to the gold square (and substrate) photoemission curve. As a check, we moved the sample stage along the direction of the lines, to move the stage by a visible amount to determine the orientation of the lines with respect to the polarizer. As far as can be judged by eye, the lines are perpendicular to the linear polarizer orientation. Thus, the photoemission maxima at  $\Phi = 45^\circ$  in  $\lambda/2$  plate correspond to polarization parallel to the lines. This is in line with the results reported by Sun et al. [18], where two photoemission hotspots at the ends of the gold structures parallel the laser polarization were observed.

As argued above, the photoemission intensity is expected to follow a sine function, as the polarization rotated by  $2\Phi$  with respect to the original s-polarization, is projected onto the s- and p-component. Figure 6.5 shows the function

$$\frac{I(\Phi)}{I_0} = 1 + \left( \frac{T_p}{T_s} - 1 \right) \cdot \sin^2(2\Phi + \Phi_0) \quad \text{eq. 1}$$

overlaid on the data. For the lines, a phase shift  $\Phi_0 = 45^\circ$  is applied, as they are out of phase as discussed above, whereas no phase shift ( $\Phi_0 = 0^\circ$ ) is applied to the substrate or gold square. The only free parameter in the model is the intensity  $I_0$ . The relative intensity of maxima and

minima is not fitted but set by the ratio  $T_p/T_s = 0.81/0.32$  (0.88/0.44 for the Si substrate) calculated from the literature refractive indices.

The data in Figure 6.5 is described well by the sine behavior in Equation 1 for  $I(\Phi)$ . The photoemissivity of both the line and square gold structures matches the contrast between s and p polarized expected from literature. This in turn confirms that the photoemission is proportional to the non-reflected intensity, as determined by the Fresnel equations. The phase shift  $\Phi_0$  of the line structures is close to  $45^\circ$ , although that is a coincidence in how the sample was oriented. Had the sample been rotated by another  $90^\circ$  during mounting, then the lines would have been parallel to the s polarization direction and thus not show a phase shift. The relative difference between the maxima and minima of the substrate is slightly larger than expected for Si, which can be the result using p-doped Si, that is more conductive than undoped Si.

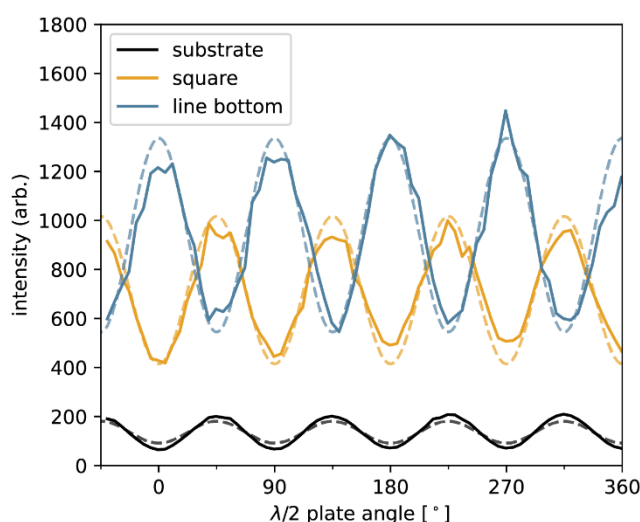


Figure 6.5: Photoemission intensity data (solid lines) and sine function fit according to Eq. 1 (dashed lines). The relative amplitude of the sine, i.e., the ratio of maximum to minimum, is fixed to the calculated value of  $T_p/T_s$  according to literature,  $T_p/T_s = 0.81/0.32$  for gold and  $T_p/T_s = 0.88/0.44$  for the Si substrate. The scaling factor of the sine is fitted, and the angular offset is set to  $0^\circ$  (for the substrate and ‘square’ curves) or  $45^\circ$  (for the ‘line bottom’ curve). The good correspondence with this one parameter fit shows, that the photoemission is proportional to the intensity of light not reflected according to the Fresnel equations.

### 6.2.3 Polarization-dependent Photoemission from BINAP

Molecules based on 2,2'-bis(diphenylphosphino)-1,1'-binaphthyl (BINAP) are commonly used as enantiopure precursors/catalysts for the enantiomer-specific synthesis of molecules. BINAP is commercially available in high enantiopurity. The S-functionalized short BINAP molecule used in this chapter was provided by our collaborators C. Hsu, A. Philip and F. Grozema at the Faculty of Applied Sciences, Delft University. The same molecule has been studied in fast break junction experiments described in chapter 7 of the PhD thesis of Chunwei Hsu [19].



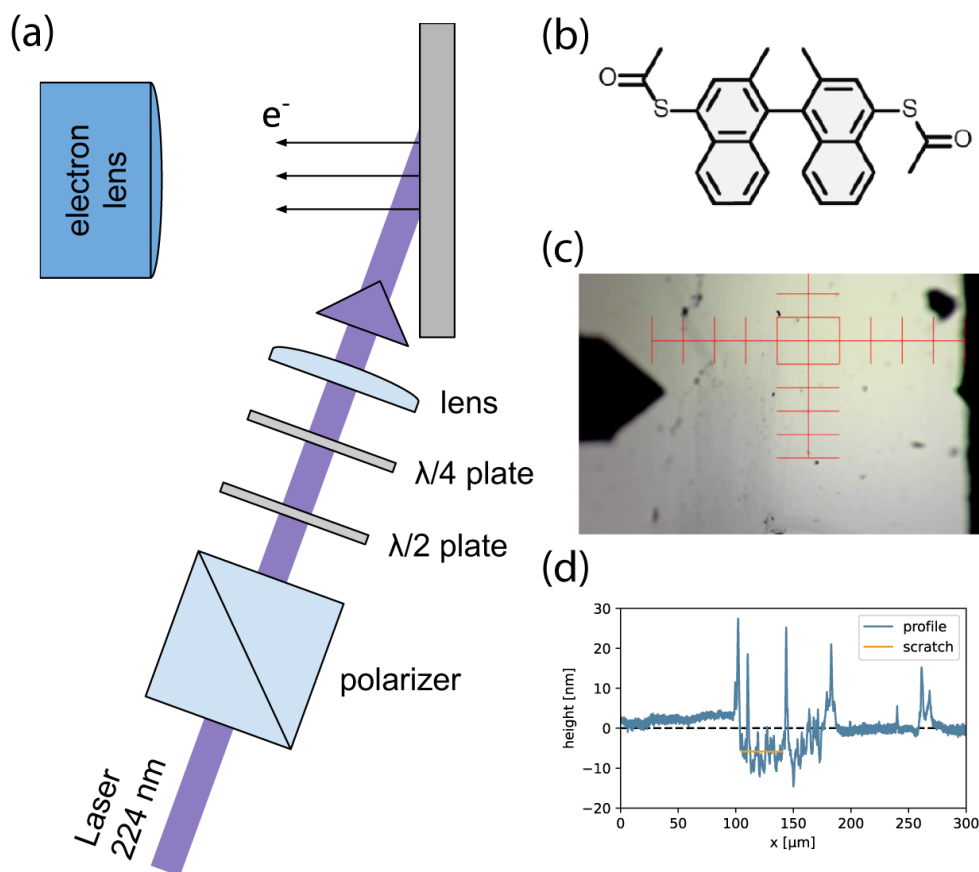


Figure 6.6: Optical setup (a) for elliptical polarization generation used on the chiral molecules. Compared to the linear polarization experiment (Fig. 6.3a), a  $\lambda/4$  plate is added after the rotatable  $\lambda/2$  plate, to turn the linear polarization into elliptical polarization. Also, a lens (focal length  $f=175$  mm) is added, to focus the DUV laser beam and thus increase the flux of photons and proportionally photoemitted electrons. The BINAP molecule is sketched in Figure 6.3b. The height of the BINAP film on gold is measured with the profilometer, by scratching the surface with a carbon tweezer tip and measuring the depth of the created trench. The optical image (c) with the vertical scratch (between the black tip and the red crosshairs) and the measured height profile (d) are shown. The scratch (marked orange in the profile, d), removing the molecular layer and possibly some of the gold layer, is 5 nm deep. The molecule structure (b) is a reproduction of Figure 7.6 in [19], where the same molecules were used.

For sample preparation, a 20 nm gold film was evaporated on a Si chip with a 5 nm titanium sticking layer. Then the modified BINAP molecules were deposited on the coated chip, by incubating it in a 0.1 mM BINAP (in dichloromethane, DCM) solution for 24 hours. On the next day, the chip was rinsed in DCM and blow-dried in nitrogen to remove excess BINAP molecules. We scratched the sample with a carbon tweezer tip to remove a strip of molecules and create an achiral reference area. Profilometer profiles were acquired after the in-vacuum measurement. The roughness of the layer shows, that it is not a well-assembled monolayer (shown in Figure 6.6d). Still the profile linecut across this scratched trench, that scratched down into the gold layer, shows that the BINAP film is thinner than 5 nm high.



To measure photoemission depending on the handedness of the circularly polarized light, a  $\lambda/4$  plate was added to the polarization control optics. The optical setup for this experiment is shown in Figure 6.6a. If the linear polarized light is incident at  $\pm 45^\circ$  from the fast axis of the  $\lambda/4$  plate, the resulting light will be right-/left- polarized. If the linear polarized light is incident along the fast (or slow) axis of the  $\lambda/4$  plate, the polarization will remain linear. In between these prototypical settings, any elliptical polarization is possible. We note that the axes of the ellipse always coincide with the fast and slow axes of the  $\lambda/4$  plate, unlike what many illustrations in textbooks suggest [20,21]. Therefore, we will keep the  $\lambda/4$  plate fixed in our experiment, aligned parallel to the linear polarizer, and vary the resulting polarization by rotating the  $\lambda/2$  plate angle  $\Phi$  on a motorized mount. Rotating the  $\lambda/4$  plate would result in a rotation of the long axis of the ellipse with respect to the s-/p-polarization axis. If the  $\lambda/4$  plate is indeed perfectly aligned parallel to the s-/p- axis of the sample and if it were rotated symmetrically, the linear projection of the long ellipse axis on the s-/p-axis would not affect the photoemission intensity background, but as we expect the chirality signal to be small compared to the linear polarization response (investigated above), fixing the  $\lambda/4$  plate is advantageous.

We checked the alignment of the  $\lambda/4$  plate by symmetrically rotating the  $\lambda/2$  plate and comparing the photoemission intensity on an achiral area of the sample. The achiral area was produced by illuminating it with the LEEM beam at 100 eV electron energy for 30 s, which leads to bond breaking and making [22]. A loss of the chiral signal has been shown in transport devices after applying 1 mA current over a  $5 \times 5 \mu\text{m}^2$  junction [23] and by ellipsometry after exposure to UV light [24].

As the light is incident on the sample under an angle of  $\Theta = 70^\circ$  from the surface normal, the projection of circular polarization on the sample will be squished into elliptical polarization along the plane spanned by the incident and reflected ray, while the polarization component perpendicular to that plane (s-component) remains unaltered. The projected component  $E_{p,\text{proj}}$  of the polarization  $E_p$  is shortened to  $E_{p,\text{proj}} = \sin(\alpha) \cdot E_p \approx 0.34 \cdot E_p$  as shown in Figure 6.2. To compensate for this projection effect and reach a circular polarization projected on the sample, we aim to adjust the laser polarization to elliptical polarization that is elongated by  $1/\sin \alpha$  in the p-polarization direction. The ellipticity of the light after passing the  $\lambda/4$  plate is given by the ratio of the linear electric field projected on the fast and slow axis of the  $\lambda/4$  plate,  $E_{\text{fast}}/E_{\text{slow}} = E_{\text{lin}} \cdot \cos(2\Phi)/\sin(2\Phi)$ . Thus, the requirement is  $\tan(2\Phi) = \sin(\alpha)$ . This is the case for the fast axis of the  $\lambda/4$  plate aligned to the p-polarization direction and the linear polarized light incident on the  $\lambda/4$  plate at  $2\Phi = \pm 18^\circ$  from the fast axis. Therefore, we will acquire images with the  $\lambda/2$  plate set to  $\Phi = \pm 9^\circ$  from the fast axis of the  $\lambda/4$  plate. For short, we will refer to these settings as R-polarized ( $\Phi = +9^\circ$ ) and L-polarized ( $\Phi = -9^\circ$ ) light.

For the following measurement, we also added a lens (DUV enhanced, plano-convex,  $f=175$  mm) to the setup, to focus the laser intensity to a smaller spot and thus increase the flux of photoemitted electrons. The focused spot is still larger than the field of view in PEEM mode. As the focal length of the lens is large with  $f = 175$  mm, the distortions it introduces to

polarization are expected to be minimal. As the electron emission is still low and the low electron count will be the major noise source, a large field of view was chosen in the recording.

The horizontal lines in Figure 6.6 are the scratch marks created by scratching the carbon tweezer tip over the sample to remove the molecules. The darker photoemission indicates that we reached a more pristine gold layer that has a higher work function than the BINAP molecules.

To test the effect of the different elliptical polarization on electron emission, thus the CISS effect on the BINAP film, the difference image between the right-handed and left-handed illumination images (Fig. 6.7b and Fig. 6.7a, respectively) is shown in Figure 6.8a. The scale bar shows the relative difference between R and L polarization, with areas that are brighter in right-handed polarization in red and areas that are brighter in left-handed polarization in blue. Zero difference, i.e., no chiral effect, is shown in white. The difference image in Figure 6.8a is very noisy and does not allow us to identify a clear trend. However, this may be due to the fact that we start with noisy images (due to low electron count) already. To reduce the noise in the difference image further, we will need more images.

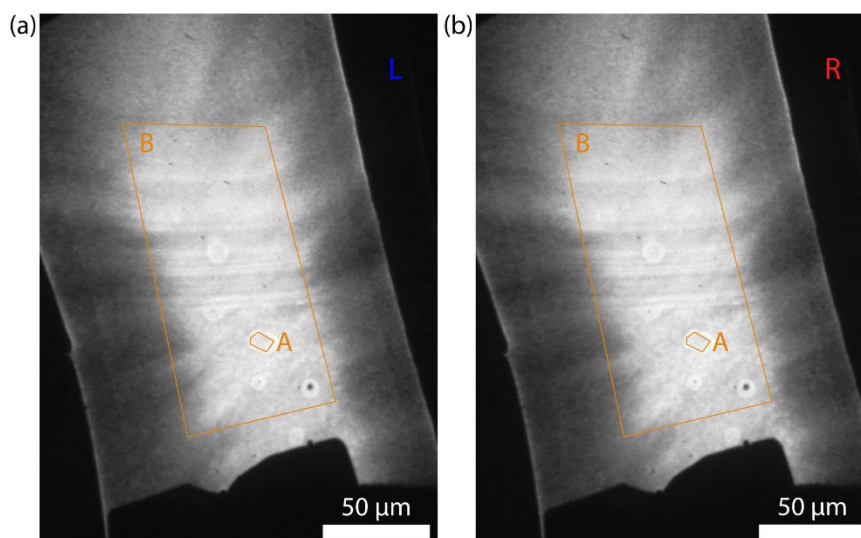


Figure 6.7: Photoemission microscopy images acquired with (a) left elliptical polarized (labelled L) light and (b) right elliptical polarized light (labelled R). Each image is integrated over 64 laser pulses, and no clear difference between L- and R-polarization is visible. Area A marks the area that is expected to be achiral, as it was illuminated with the electron beam at 100 eV for 30 s. Area B is taken as a large reference area. The intensity histograms of area A and B will be discussed in Figure 6.8d.

Figure 6.7 shows photoemission images of the sample acquired by illuminating the sample with left-polarized light (labeled L, Fig. 6.7a) and with right-polarized light (labeled R, Fig. 6.7b). Each image was acquired by integrating 64 laser pulses. There is no clear difference visible between the two images. The electron beam imprint, created by exposing the sample to 100 eV electrons for 30 seconds, is labeled area A in Figure 6.7a/b. It appears as a bright, elongated imprint, and was used to align the optical retardation plates symmetrically, as we assume that the chirality of the molecules has been destroyed. Some other bright spots with a dark spot in

the center are visible; these are not beam imprints, but bubbles formed during drying of the sample.

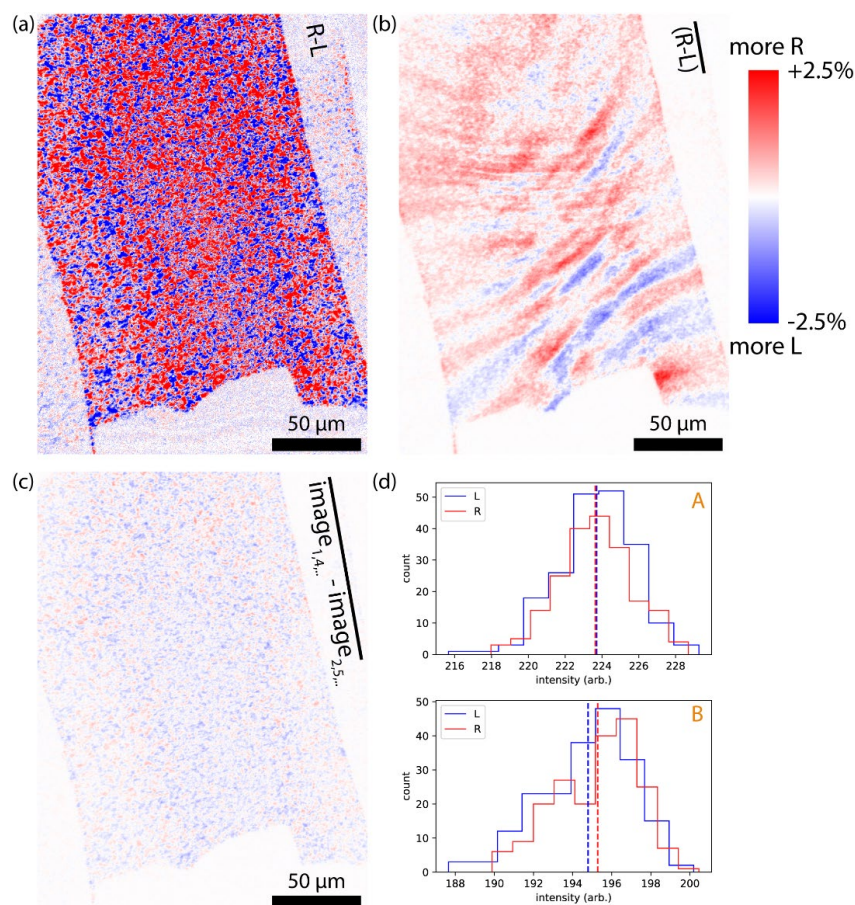


Figure 6.8: (a) Difference image between one left elliptical polarized and one right elliptical polarized image, showing mostly noise as the intensity in each image is low. (b) Difference between all 200 left elliptical polarized images and all 200 right elliptical polarized images, showing characteristic streaks of areas that are more emissive in R-polarization and areas that are more emissive in L-polarization. These large, smoothly transitioning areas do not coincide with the sharp features, like the achiral beam damage spot or the scratch, on the sample, indicating that the emissivity difference is related to uneven illumination depending on  $\lambda/2$  plate setting. (c) Difference between 132 images in steps of 3, and their following images, thus image 1,4,7,.. minus image 2,5,8,... . Thus, there are 66 right-elliptical and 66 left-elliptical images in each group, thus polarization effects should even out, as we see in the noisy image. (d) Photoemission intensity histograms, separate for right- and left-handed elliptical light (L and R), for the areas indicated in Figure 6.7. Area A is a beam imprint used for aligning the polarization symmetrically and area B a large average.

Hence, we recorded 200 left-polarized and 200 right-polarized images like in Figure 6.7, illuminated with 64 laser pulses each, always alternating between L and R polarization after 64 laser pulses, as to minimize the effect of laser intensity drift and sample deterioration over the acquisition period of approximately 3 hours. The difference image between these 200 left-polarized and 200 right-polarized images is shown in Figure 6.8b. This image is less noisy indeed and features patches of more photoemissivity at right-handed or left-handed polarization, with relative intensity differences of up to 2.5 %.

However, these areas mostly have very smooth transitions, like continuous hills and valleys, that do not coincide with the features on the sample visible in Figure 6.7. For CISS features, we would expect a sharp loss of contrast at the non-chiral, i.e., the scratched and electron beam-burnt, areas. Only the sharp edges of the horizontal scratches are visible as white lines in Figure 6.8b, but there is no difference between the scratched area and the surrounding molecules. The beam imprint used for aligning polarization falls between a R-dominated and a L-dominated area.

The fact that the difference image has little coincidence with the features of the sample, suggests that the polarization difference in different areas is caused by different intensity distribution of the incoming light when changing the  $\lambda/2$  plate setting. To test that the difference between images shown in Figure 6.8b is a result of the different polarizations, instead of different intensities, we next regroup the images and take the difference between equally many right-polarized and left-polarized images. The difference image is shown in Figure 6.8c. Here, we have grouped images 1,4,7,... together, thus 66 right and 66 left circularly polarized images grouped together, minus images 2,5,8,..., thus again 66 right and 66 left circularly polarized images, grouped together. The fact that the resulting difference image only contains noise around zero shows, that the difference in Figure 6.8b is related to the different polarization settings.

The mean intensity of the beam imprint area A was extracted for each of the 200 left-polarized and 200 right-polarized images and makes up the histograms shown in Figure 6.8d, separated for left (L, blue) and right (R, red) circular polarization. The mean of the R- and L-polarized histogram is shown with a dashed line in the respective color. In area A, the mean intensity of the R- and L-polarized photoemissions coincides, which is not surprising as we used this area to align the polarization symmetrically.

The histogram acquired in the same way on the big, illuminated area, labeled B in Figure 6.7, is also shown in Figure 6.8d. The shift towards higher intensity of the histogram in R-polarized illumination suggests that photoemission is favored in R-polarization. The mean intensity of area B in R-polarization is approximately 1% higher than in L-polarization. However, from the different L- and R-polarization favored patches in the integrated difference image Fig. 6.8b, we conclude that this majority is ambiguous, as we could have chosen a different spot than area A to align the polarization symmetrically and would have gotten a different result.

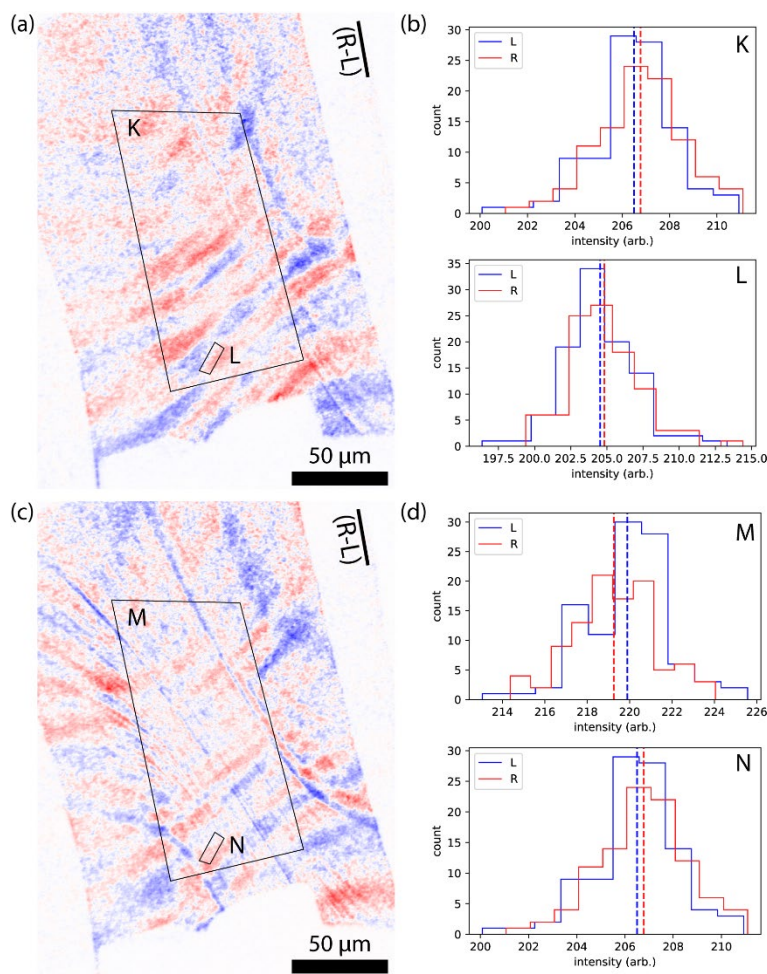


Figure 6.9: More difference images (a,c) of different areas and their histograms (b,d) on the respective large areas (K, M) and the beam imprint areas (L, N). The difference images (a,c) were acquired like the one on Figure 6.8b, but on different areas. The images show areas around the vertical tweezer tip scratch. The streaks caused by uneven illumination in L- and R-polarization show the same pattern for all the areas, confirming that they are unrelated to the chiral molecules on the sample. Depending on the chosen area, one may get a preference for photoemission in L- or R-polarization, as visible in the histograms (b,d). The electron beam spots (L,N) are shifted with respect to Figure 6.7, as the sample was moved, deflecting the electron beam.

The integrated difference images from another two areas (100 R-polarized minus 100 L-polarized images each) are shown in Figure 6.9a/c, together with their corresponding histograms in Figure 6.9b/d, respectively. Both difference images show the same horizontal streak pattern, which we attributed to uneven illumination in Figure 6.8. The difference image in Figure 6.9c shows an area closer to the edge of the sample. The histograms in Figure 6.9 are acquired on the large illuminated areas K/M (like area B in Figure 6.7) and the beam imprint areas L/N (comparable to area A in Figure 6.7). The real-space position of the beam imprint area is shifted in comparison to Figure 6.7 because of the non-perpendicular electric field lines close to the edge of the sample. The area K in Figure 6.9a shows a slight preference for photoemission from R-polarized light, while the area M in Figure 6.9c is brighter in L-polarized light. Still, both these differences lie within 0.5 %. The difference in the small beam imprint



areas (K, M) is not zero anymore, as the electron beam is shifted due to moving the sample and the same polarizer angles as in the previous images have been used.

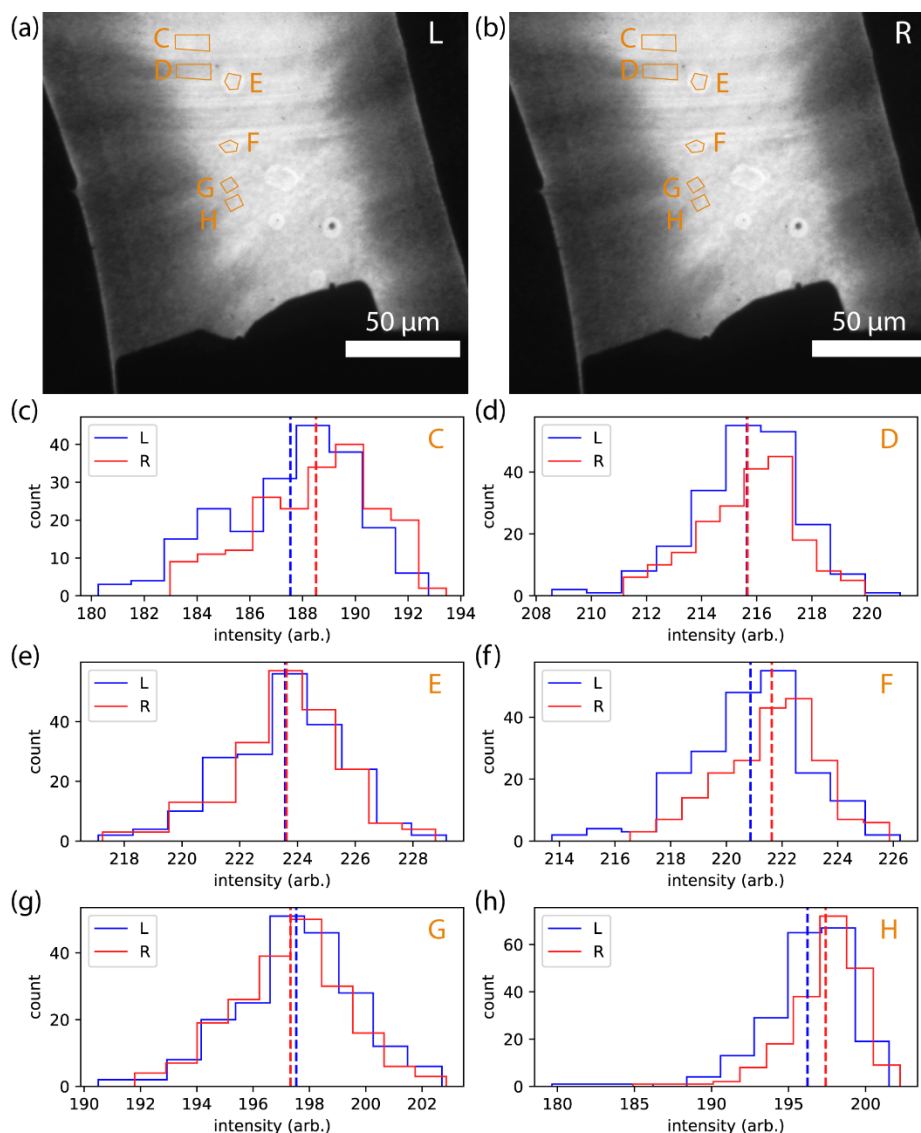


Figure 6.10: Intensity histograms (c-h) on more areas with specific features indicated in the L-polarization (a) and R-polarization (b) images. In area C, the molecules were scratched off with carbon tweezers, whereas area D next to the layer was left untouched. Areas E and F show bubbles that formed during incubation of the sample. G and H have no apparent different morphology in the photoemission images a/b. However, they happen to be illuminated with different intensity in the right- and left-elliptical polarization setting.

The polarization-dependent histograms of more features that we pointed out in Figure 6.8 are shown in Figure 6.10. The areas labeled in Figure 6.10a/b are the horizontal scratch (D) and a neighboring area (C), a beam imprint (E), a bubble F, and two neighboring areas that are not separated by a visible feature (G and H). Areas G and H have been chosen, as they look like parts of the same uniform area in the photoemission images but fall on streaks of different majority polarization emission in the difference image (Fig. 6.8b).

The histograms of the different areas, shown in Figure 6.10c-h, show how the photoemission intensity varies over the sample in real space: From favoring L-polarization in area G, over no chiral asymmetry in areas D and E, to favoring R-polarization in the other 3 areas. We note again that we attribute the handedness-asymmetry to the differences in illumination, although one could arrive at a different conclusion by looking at each of the individual histograms. Especially the difference between histograms of areas G and H, which cannot be explained by differences in the sample, evokes suspicion.

In all cases, the differences between the mean intensity of left-handed and right-handed induced photoemission we measured are below 1% for each area considered.

#### 6.2.4 Further calculation of transmitted polarization

Still, our conclusion above needs some refinement. In an experimental geometry with normal incidence of the light, the phase shift of the reflected light does not change light polarization due to symmetry, as s- and p-polarization are equivalent/undefined. The larger the incidence angle (from the normal) is, the larger the phase shift difference between the s- and p-polarization [25]. While the photoemission experiments by Ray et al. [1] were conducted with the UV light at normal incidence on the sample, in our case the laser beam hits the sample at  $70^\circ$  from the surface normal. We expect that most electron microscopy setups will suffer from similar constraints, as it is crucial to have the electron objective lens aligned straight over the sample, thus obstructing the normal light path.

Although we chose the incident light polarization in our experiments such that its projection on the surface yields circularly polarized light, we will now also discuss the polarization of the transmitted light after taking the phase shift upon transmission through a metal into account. We expect that the transmitted polarization, i.e., right below the gold surface, is decisive for the polarization-dependent spin-polarized photoemission from gold.

For this reason, we calculated the reflected polarization from the incident elliptical polarization as applied in our experiment above, using the complex refractive index reported in [13]. The sum of the incident and reflected field are shown in Figure 6.11. The blue curve shows the path the electric field vector described as it is propagated in time. As the  $\vec{D}$  field is continuous at the vacuum-gold interface, the transmitted polarization right under the gold surface is proportional to the sum of the incident and reflected field.

The aspect ratio of the minor to the major axis of the polarization ellipse is  $r = 0.45$ . When projected on the gold surface this ratio is only  $r_{xy} = 0.20$ , much closer to linear than to circular polarization. The elliptical polarization can be expressed as a sum of left- and right-circular polarizations with (non-normalized) amplitudes  $E_{\text{right-circ.}} = 1$  and  $E_{\text{left-circ.}} = 1 - r$  (and vice-versa for the opposite polarizations). As a result, we expect that the spin-polarization of the photoexcited electrons is reduced by  $(E_{\text{right-circ.}} - E_{\text{left-circ.}})/(E_{\text{right-circ.}} + E_{\text{left-circ.}}) = r/(2 - r)$ . Thus, for  $r = 0.45$  we expect a reduction factor of the spin-polarization of 0.29 and for the ellipticity projected on the gold surface of  $r_{xy} = 0.20$  a reduction factor of 0.11.

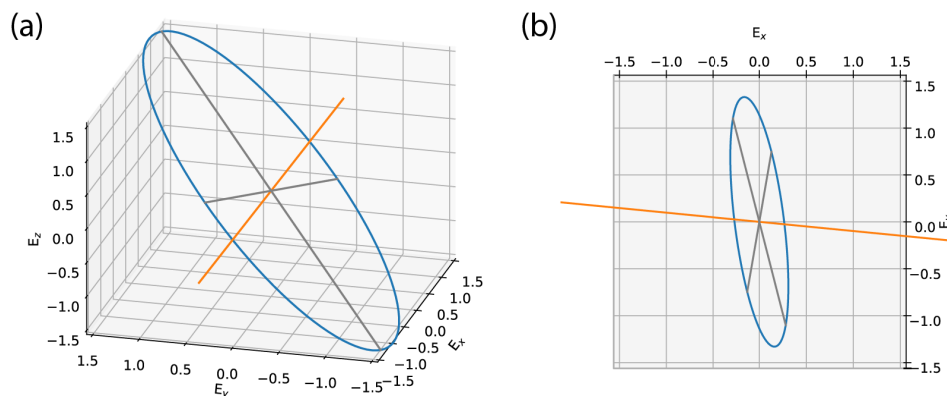


Figure 6.11: Three-dimensional view (a) and top view (b; i.e., projected on the gold surface) of the light polarization (electric field vector, blue) at the gold surface. The major/minor axes of the ellipse (gray) and the normal (orange) are shown for orientation. The reflected light experiences a phase shift difference between s- and p-polarization and is superimposed on the incoming light.

If we assume that the polarization transmitted into the gold surface is decisive for the photoemitted spin-polarization, the off-normal light incidence in our experiment diminishes the detectable spin population asymmetry by a factor nine, making a CISS-related intensity difference of 10% indistinguishable from the spatial variation of incident polarization. This may be improved by optimizing the elliptical polarization of the incident light.

### 6.3 Conclusions and Recommendations

While the optical polarization is well characterized in our experiment, the quality of the chiral layer prevents us from making final claims about the CISS effect in BINAP. Specifically, Ray et al. [1] showed that little disorder (1% of the opposite enantiomer) destroys the spin selectivity of the sample. Measurements of the flatness of the molecular film and the depth of the scratched trench show that we did not have a self-assembled monolayer. To grow better films, more elaborate characterization techniques, e.g., ellipsometry, are necessary. When imaging polarization-dependent photoemission we recommend having a known-achiral reference area, to be contrasted to the signal.

While we have aligned the polarizers to yield symmetric photoemission on the beam spot on the electron-optical axis, the other areas show streak-like asymmetries of up to 1%. These asymmetries do not correlate with the features on the sample and are thus attributed to the illumination optics. Together with the off-normal incidence, reducing the spin-polarization of the electrons photoemitted from the gold surface by up to a factor nine, this asymmetry is comparable to the asymmetry in photoemission due to the CISS effect, which is in the order of 10% as suggested in [5,10] (at normal incidence of circularly polarized light). The effect of asymmetric polarization of the incident light may be partially mitigated by patterning achiral reference areas on the sample on a length scale much smaller than the streaks seen in the illumination.



The experiment could be improved by aligning the illumination laser to perpendicular incidence, thus removing the asymmetry between s- and p-linearly polarized light. In a LEEM setup, this would require aligning the laser beam through the electromagnetic prism and through the electromagnetic objective lens. Alternatively, it is more feasible to reach normal light incidence by illuminating the sample from the backside. This requires a gold surface grown on a transparent, optically isotropic substrate (at UV wavelengths) and polarization-controlled illumination from the back of the sample holder. After we conducted the above experiments, a back illumination of the sample holder was installed in our LEEM instrument to conduct back-illuminated PEEM [26]. In the final form of optical near-field electron microscopy (ONEM) [27] polarization control will be added to the ESCHER LEEM, fulfilling the requirements for new photoemission experiments on chiral organic layers with a more suitable illumination geometry.

We note that spin-dependent low energy electron microscopy (SPLEEM) [28] and angle-resolved photoemission spectroscopy (ARPES, spin-PES) [29,30] setups are developed, that can gain insight into the CISS effect with spatial and angular resolution in the future.

The variety of measurement techniques that have shown the CISS effect also implies that the effect is robust over a large energy scale. While the transport experiments probe the band structure around the Fermi energy, the photoemission experiments (together with time-of-flight spectroscopy) reveal it up to 2 eV above the vacuum level, i.e., 5 to 8 eV higher. This energy scale is in practice limited by the photon energy that can be applied without damaging the sample.

The robustness in applications and the implications for the understanding of biological chiral molecules make the study of chirality-induced effects fascinating and worthwhile. Despite the large progress in recent years, it still requires efforts from experimental and theoretical side to fully understand the CISS effect.

## Acknowledgements

We acknowledge Brenda Rovers for fabricating the plasmonic samples and the first organic layer samples, and Chunwei Hsu, Ferdinand Grozema and Abbey Philip for providing us with the modified BINAP molecule. We thank the groups of Jan van Ruitenbeek, Ferdinand Grozema, Herre van der Zant, and Jos Thijssen for valuable discussions throughout the project.

## References

- [1] K. Ray, S.P. Ananthavel, D.H. Waldeck, R. Naaman, Asymmetric scattering of polarized electrons by organized organic films of chiral molecules, *Science* (80-. ). 283 (1999) 814–816. <https://doi.org/10.1126/science.283.5403.814>.
- [2] F. Evers, A. Aharony, N. Bar-Gill, O. Entin-Wohlman, P. Hedegård, O. Hod, P. Jelinek, G. Kamieniarz, M. Lemeshko, K. Michaeli, V. Mujica, R. Naaman, Y. Paltiel, S. Refaely-Abramson, O. Tal, J. Thijssen, M. Thoss, J.M. van Ruitenbeek, L. Venkataraman, D.H. Waldeck, B. Yan, L. Kronik, Theory of Chirality Induced Spin Selectivity: Progress and Challenges, *Adv. Mater.* 34 (2022) 1–11. <https://doi.org/10.1002/adma.202106629>.
- [3] T.K. Das, F. Tassinari, R. Naaman, J. Fransson, Temperature-Dependent Chiral-Induced Spin Selectivity Effect: Experiments and Theory, *J. Phys. Chem. C* 126 (2022) 3257–3264. <https://doi.org/10.1021/acs.jpcc.1c10550>.
- [4] J.M. van Ruitenbeek, R. Korytár, F. Evers, Chirality-controlled spin scattering through quantum interference, *J. Chem. Phys.* 159 (2023). <https://doi.org/10.1063/5.0156316>.
- [5] B. Göhler, V. Hamelbeck, T.Z. Markus, M. Kettner, G.F. Hanne, Z. Vager, R. Naaman, H. Zacharias, Spin selectivity in electron transmission through self-assembled monolayers of double-stranded DNA - Supplementary Information, *Science* (80-. ). 331 (2011) 894–897. <https://doi.org/10.1126/science.1199339>.
- [6] Z. Xie, T.Z. Markus, S.R. Cohen, Z. Vager, R. Gutierrez, R. Naaman, Spin specific electron conduction through DNA oligomers, *Nano Lett.* 11 (2011) 4652–4655. <https://doi.org/10.1021/nl2021637>.
- [7] V. Kiran, S.P. Mathew, S.R. Cohen, I. Hernández Delgado, J. Lacour, R. Naaman, Helicenes - A New Class of Organic Spin Filter, *Adv. Mater.* 28 (2016) 1957–1962. <https://doi.org/10.1002/adma.201504725>.
- [8] D. Amsallem, A. Kumar, R. Naaman, O. Gidron, Spin polarization through axially chiral linkers: Length dependence and correlation with the dissymmetry factor, *Chirality* 35 (2023) 562–568. <https://doi.org/10.1002/chir.23556>.
- [9] C. Clever, E. Wierzbinski, B.P. Bloom, Y. Lu, H.M. Grimm, S.R. Rao, W.S. Horne, D.H. Waldeck, Benchmarking Chiral Induced Spin Selectivity Measurements - Towards Meaningful Comparisons of Chiral Biomolecule Spin Polarizations, *Isr. J. Chem.* 62 (2022) 1–14. <https://doi.org/10.1002/ijch.202200045>.
- [10] M. Kettner, V. V. Maslyuk, D. Nürenberg, J. Seibel, R. Gutierrez, G. Cuniberti, K.H. Ernst, H. Zacharias, Chirality-Dependent Electron Spin Filtering by Molecular Monolayers of Helicenes, *J. Phys. Chem. Lett.* 9 (2018) 2025–2030. <https://doi.org/10.1021/acs.jpcllett.8b00208>.
- [11] E. Hecht, 4 The Propagation of Light, in: *Optics*, 2nd ed., Addison-Wesley Publishing Company, 1987.

- [12] D.E. Aspnes, A.A. Studna, Dielectric functions and optical parameters of Si, Ge, GaP, GaAs, GaSb, InP, InAs, and InSb from 1.5 to 6.0 eV, *Phys. Rev. B* 27 (1983) 985–1009. <https://doi.org/10.1103/PhysRevB.27.985>.
- [13] A. Ciesielski, L. Skowronski, M. Trzcinski, E. Górecka, P. Trautman, T. Szoplík, Evidence of germanium segregation in gold thin films, *Surf. Sci.* 674 (2018) 73–78. <https://doi.org/10.1016/j.susc.2018.03.020>.
- [14] W.M. Haynes, *CRC Handbook of Chemistry and Physics*, CRC Press, 2014. <https://doi.org/10.1201/b17118>.
- [15] W.M.H. Sachtler, G.J.H. Dorgelo, A.A. Holscher, The work function of gold, *Surf. Sci.* 5 (1966) 221–229. [https://doi.org/10.1016/0039-6028\(66\)90083-5](https://doi.org/10.1016/0039-6028(66)90083-5).
- [16] A.N. Guerreiro, I.B. Costa, A.B. Vale, M.H. Braga, Distinctive Electric Properties of Group 14 Oxides: SiO<sub>2</sub>, SiO, and SnO<sub>2</sub>, *Int. J. Mol. Sci.* 24 (2023). <https://doi.org/10.3390/ijms242115985>.
- [17] T. Yoshioka, H. Fujita, Y. Kimura, Y. Hattori, M. Kitamura, Wide-range work function tuning in gold surfaces modified with fluorobenzenethiols toward application to organic thin-film transistors, *Flex. Print. Electron.* 5 (2020). <https://doi.org/10.1088/2058-8585/ab71e3>.
- [18] Q. Sun, K. Ueno, H. Yu, A. Kubo, Y. Matsuo, H. Misawa, Direct imaging of the near field and dynamics of surface plasmon resonance on gold nanostructures using photoemission electron microscopy, (2013) 1–8. <https://doi.org/10.1038/lssa.2013.74>.
- [19] C. Hsu, Chirality-induced spin selectivity, in: *Conform. Spin Eff. Single - Mol. Electron. Transp.*, 2022: pp. 99–121. <https://doi.org/10.4233/uuid:1d3b6977-0abf-40fa-bc94-b7617e158b81>.
- [20] F.L. Pedrotti, L.S. Pedrotti, L.M. Pedrotti, 14 Matrix treatment of Polarization, in: *Introd. to Opt.*, 2nd ed., Pearson Prentice Hall, San Francisco, 1993.
- [21] E. Hecht, A. Zajac, 8 Polarization, in: *Optics*, 4th ed., Addison-Wesley Publishing Company, 1979. <https://books.google.nl/books?id=eLruAAAAMAAJ>.
- [22] A. Tebyani, F.B. Baalbergen, R.M. Tromp, S.J. van der Molen, Low-Energy Electron Irradiation Damage in Few-Monolayer Pentacene Films, *J. Phys. Chem. C* 125 (2021) 26150–26156. <https://doi.org/10.1021/acs.jpcc.1c06749>.
- [23] T. Liu, X. Wang, H. Wang, G. Shi, F. Gao, H. Feng, H. Deng, L. Hu, E. Lochner, P. Schlottmann, S. Von Molnár, Y. Li, J. Zhao, P. Xiong, Linear and nonlinear two-terminal spin-valve effect from chirality-induced spin selectivity, *ACS Nano* 14 (2020) 15983–15991. <https://doi.org/10.1021/acsnano.0c07438>.
- [24] A. Steinbacher, P. Nuernberger, T. Brixner, Optical discrimination of racemic from achiral solutions, *Phys. Chem. Chem. Phys.* 17 (2015) 6340–6346. <https://doi.org/10.1039/c4cp05641h>.
- [25] F.A. Jenkins, H.E. White, Chapter 25: Reflection, in: *Fundam. Opt.*, 4th ed, 1976: pp. 523–543.

- [26] A. Moradi, M. Rog, G. Stam, R.M. Tromp, S.J. van der Molen, Back illuminated photo emission electron microscopy (BIPEEM), *Ultramicroscopy* 253 (2023) 113809. <https://doi.org/https://doi.org/10.1016/j.ultramic.2023.113809>.
- [27] R. Marchand, R. Šachl, M. Kalbáč, M. Hof, R. Tromp, M. Amaro, S.J. Van Der Molen, T. Juffmann, Optical Near-Field Electron Microscopy, *Phys. Rev. Appl.* 16 (2021) 1–8. <https://doi.org/10.1103/PhysRevApplied.16.014008>.
- [28] L. Yu, W. Wan, T. Koshikawa, M. Li, X. Yang, C. Zheng, M. Suzuki, T. Yasue, X. Jin, Y. Takeda, R. Tromp, W.X. Tang, Aberration corrected spin polarized low energy electron microscope, *Ultramicroscopy* 216 (2020) 113017. <https://doi.org/10.1016/j.ultramic.2020.113017>.
- [29] C. Jozwiak, J.A. Sobota, K. Gotlieb, A.F. Kemper, C.R. Rotundu, R.J. Birgeneau, Z. Hussain, D.H. Lee, Z.X. Shen, A. Lanzara, Spin-polarized surface resonances accompanying topological surface state formation, *Nat. Commun.* 7 (2016) 1–7. <https://doi.org/10.1038/ncomms13143>.
- [30] Y.S. Dedkov, M. Fonin, U. Rüdiger, G. Güntherodt, Spin-resolved photoelectron spectroscopy of the MgO/Fe(110) system, *Appl. Phys. A* 82 (2006) 489–493. <https://doi.org/10.1007/s00339-005-3447-2>.



# SUMMARY

Molecules, crystal structures, and viruses are too small to see by the naked eye. Nonetheless, they undeniably impact our daily lives. Microscopy was developed to explore this microcosmos on smaller and smaller scales. Typically, we mean optical microscopy when we think about microscopy. However, electron microscopy allows us to look at different properties and smaller length scales than light microscopy. Throughout this thesis, we draw parallels between electron and light waves, because the electron behaves as a quantum mechanical wave.

Instead of shining light at a sample and collecting what is reflected or transmitted, in electron microscopy we send electrons to the sample and detect how they are reflected or transmitted. We conduct this experiment with a low energy electron microscope (LEEM). Instead of detecting color, i.e., the wavelength of light, we can detect (and adjust) the electron energy, related to its wavelength. In both light- and electron microscopy we call the wavelength-dependent intensity a spectrum.

The spectra of thin materials presented in this thesis can largely be understood from interference, again a concept we know from optics. Optical interference answers questions like: Why do soap bubbles appear in all colors of the rainbow, while they are made from colorless soap solution? The answer is that the thickness of a bubble's wall is a few 100 nanometers, comparable to the wavelength of the light. When the light bounces back and forth between the front and back surfaces of the soap bubble wall, the transmission of some wavelengths that fit (twice) the optical path length is enhanced, and other wavelengths are reflected. The same is true for our thin samples and the electron wavelength, although on a scale of less than 1 nanometer. The electron energy needed for this is between 0 and 25 eV, which is considered very low for electron microscopy. Thus, we use a LEEM.

For example, graphene is a crystalline layer of carbon only one atom thick. When we have two layers of graphene, the electron wave bouncing back and forth between these layers interferes just like the light wave does in a soap bubble wall. By changing the electron energy, thus the electron wavelength, we can measure the spectra and find a characteristic reflection minimum and transmission maximum at 2.5 eV above the vacuum level. Upon adding more layers of graphene, these spectral features split, making for a spectral fingerprint of the layer count. The intensity and broadness of these spectral features are related to the probability of inelastically scattering the electron, characterized by the inelastic mean free path determined in Chapter 3. The inelastic mean free path tells us, how far an electron will travel on average before it hits

something and loses energy. The more often the electron bounces back and forth between the layers without being disturbed, the sharper the features. In optical terms, the finesse of the cavity (that is light bouncing between two mirrors in optics), increases with the lifetime of the resonance state.

We apply this interference model to different two-dimensional materials, reaching from the conducting graphene, via the insulating hexagonal boron nitride (hBN), to the semiconducting molybdenum disulfide ( $\text{MoS}_2$ ).  $\text{MoS}_2$  is different from graphene and hBN, as the molybdenum atoms are located in a 2D plane sandwiched between a plane of sulfur atoms above and below. Thus, the samples of bi- and tri-layer  $\text{MoS}_2$  we measure in Chapter 5 are relatively thick compared to tri-layer graphene. Comparison to calculated reflection and transmission spectra shows that we can measure and model the electron interactions even in this rather complicated compound.

Another central concept in physics is symmetry: We ask ourselves, whether an electron can know if it hits the front or the back side of the sample. For a sample consisting of only graphene, the front side and the rear side of the sample are indistinguishable. However, if we have a sample with graphene on one side and hexagonal boron nitride on the other, there may be a difference in electron reflection. In Chapter 4 we consider such a sample with broken symmetry and show that inelastic scattering is vital to change reflection depending on the sample orientation.

In the final chapter, we are concerned with a different type of symmetry breaking. A chiral object is one that cannot be rotated and/or moved to look like its mirrored version. The typical example of chirality (from Greek *cheir*=hand) are our hands, which are mirror versions of each other but clearly distinct. On the length scale of molecules, handed molecules have the same chemical composition but a different arrangement in space. Remarkably, the arrangement plays a role in biological processes.

In Chapter 6 we use ultraviolet (UV) light to liberate ('photoemit') electrons out of a surface covered with chiral molecules. We investigate the interplay between the handedness of light polarization with the handedness of chiral organic molecules. The chirality of the molecules has been reported to couple to the spin of transmitted electrons and spin-filter them: a phenomenon known as the chirality-induced spin selectivity (CISS) effect. We demonstrate control of the light polarization on 400 nm long gold rods. As the size of the gold rods is comparable to the UV wavelength, the electric field (of the light wave) can excite a resonant wave in the gold electrons when it is aligned with the long axis. This enhancement of the electric field leads to a larger electron emission.

Furthermore, we show photoemission from chiral BINAP molecules. However, we could not see a significant difference between excitations with light of opposite chirality. This may be due to insufficient order of the molecular film. We characterize our setup and estimate that it is sensitive enough to detect a 1% emission difference between excitation with right-handed and left-handed circularly polarized light. Imaging the CISS effect with nanometer resolution, as opposed to measuring averages over a whole sample, will allow for a better understanding and for building better devices utilizing the effect.

# SAMENVATTING

Moleculen, kristalstructuren en virussen zijn te klein om met het blote oog te zien. Toch hebben ze een enorme invloed op ons dagelijks leven. Om deze microkosmos op een steeds kleinere schaal te verkennen werden microscopen uitgevonden. Als we aan microscopen denken, bedoelen we meestal lichtmicroscopen. We kunnen echter ook elektronenmicroscopen gebruiken. Hiermee kunnen we andere eigenschappen en kleinere lengteschalen te onderzoeken dan met conventionele lichtmicroscopen. In dit proefschrift zullen we herhaaldelijk parallellen tussen elektron- en lichtgolven trekken, omdat elektronen zich als kwantummechanische golven gedragen.

In plaats van een monster te belichten met licht en te meten wat wordt weerkaatst en/of doorgelaten, sturen wij elektronen naar het monster en meten we hoe de elektronen worden gereflecteerd of doorgelaten. Dit doen we in onze lage-energie elektronenmicroscop (LEEM). In plaats van de kleur te meten, d.w.z. de golflengte van het licht, kunnen wij de elektronenenergie meten (en instellen), die gerelateerd is aan de kwantummechanische golflengte van het elektron. Bij zowel licht- als elektronenmicroscopie noemen we een meting van intensiteit als functie van golflengte (of energie) een spectrum.

De spectra van dunne materialen in deze studie kunnen grotendeels worden begrepen door middel van interferentie, een ander concept dat we kennen uit de optica. Optische interferentie beantwoordt vragen als: Waarom verschijnen zeepbellen in alle kleuren van de regenboog, ook al zijn ze gemaakt van een kleurloze zeepoplossing? Het antwoord is dat de wanddikte van een zeepbel een paar honderd nanometer is, wat dicht bij de golflengte van het licht komt. Wanneer het licht tussen de voor- en achterkant van de zeepbelwand heen en weer wordt geëkaatst, worden sommige golflengtes die overeenkomen met (tweemaal) de optische weglengte bij voorkeur doorgelaten, terwijl andere golflengtes worden gereflecteerd. Hetzelfde geldt voor onze dunne monsters en de golflengte van de elektronen, zij het dat de lengteschaal nu minder dan één nanometer is. De elektronenergieën die we hiervoor gebruiken liggen tussen de 0 en 25 eV wat zeer laag is voor een elektronenmicroscop. Vandaar de keuze voor LEEM.

Grafeen is een kristallijne laag koolstof van slechts één atoom dik. Als we twee lagen grafeen hebben, interfereert de golf van het elektron dat tussen deze lagen heen en weer kaatst net zoals de lichtgolf in een zeepbelwand. Door de elektronenenergie en dus de elektronengolflengte te variëren, kunnen we de spectra meten en we zien een karakteristiek reflectieminimum en transmissiemaximum op 2,5 eV boven het vacuümniveau. Als er meer lagen grafeen worden



toegevoegd, splitsen deze extremen zich en geven ze een spectrale vingerafdruk van het aantal lagen. De intensiteit en breedte van deze spectrale kenmerken zijn gerelateerd aan de waarschijnlijkheid dat het elektron inelastisch (d.w.z. met verlies van energie) uit zijn baan wordt geworpen. Deze inelastische verstrooiing wordt gekarakteriseerd door de inelastische gemiddelde vrije weglengte, die we in hoofdstuk 3 bepalen. De inelastische gemiddelde vrije weglengte geeft aan hoe ver een elektron gemiddeld vliegt voordat het iets raakt en energie verliest. Hoe vaker het elektron heen en weer botst tussen de lagen zonder verstoord te worden, hoe scherper de kenmerken in het spectrum. In optische termen: de finesse van de optische resonator (in de optica is dat het licht dat heen en weer kaatst tussen twee spiegels) neemt toe met de levensduur van de resonantietoestand.

We passen dit interferentiemodel toe op verschillende tweedimensionale materialen, van geleidend grafeen tot isolerend hexagonaal boornitride (hBN) en halfgeleidend molybdeendisulfide ( $\text{MoS}_2$ ).  $\text{MoS}_2$  verschilt van grafeen en hBN doordat de molybdeenatomen zich in een laag bevinden, die van boven en onder wordt omsloten ('gesandwich') door een laag zwavelatomen. Daarom zijn de monsters van twee- en drielaags  $\text{MoS}_2$ , die we in hoofdstuk 5 meten al relatief dik in verhouding tot drie lagen grafeen. Een vergelijking met berekende reflectie- en transmissiespectra laat zien dat we de interacties met elektronen zelfs in dit tamelijk ingewikkelde materiaal kunnen meten en modelleren.

Een ander centraal concept in de natuurkunde is symmetrie. In het bijzonder vragen wij ons hier af of een elektron kan weten of het de voorkant of de achterkant van het monster raakt. In een monster dat alleen uit grafeen bestaat, zijn de voor- en achterkant niet te onderscheiden. Voor een monster dat bestaat uit grafeen aan de ene kant en hexagonaal boornitride aan de andere kant, kan er echter een verschil in elektronenreflectie zijn. In hoofdstuk 4 beschouwen we zo'n monster met gebroken symmetrie en laten we zien dat inelastische verstrooiing cruciaal is om de ongelijke reflectie van de onder- en bovenkant te begrijpen.

In het laatste hoofdstuk kijken we naar een ander type symmetriebreking. Een chiraal object is een object dat niet gedraaid en/of verplaatst kan worden zodat het lijkt op zijn gespiegelde versie. Het naamgevend voorbeeld van chiraliteit (van het Griekse *cheir* = hand) zijn onze handen, die elkaars spiegelbeeld zijn maar toch duidelijk verschillend. Op moleculair niveau hebben chirale moleculen dezelfde chemische samenstelling maar een andere driedimensionale ordening. Opmerkelijk genoeg speelt deze ordening een belangrijke rol in biologische processen.

In hoofdstuk 6 gebruiken we ultraviolet (UV) licht om elektronen uit een oppervlak bedekt met chirale moleculen te bevrijden (foto-elektrisch effect). We onderzoeken de interactie tussen de chiraliteit van de lichtpolarisatie en de chiraliteit van de chirale organische moleculen. In de wetenschappelijke literatuur is gerapporteerd dat de chiraliteit van de moleculen koppelt aan de spin van de doorgelaten elektronen en deze filtert: een fenomeen dat bekend staat als het *chirality-induced spin selectivity-effect* (CISS-effect). We laten zien dat we de polarisatietoestand van het licht willekeurig kunnen variëren, door licht op 400 nm lange goudnanostaafjes te schijnen. Aangezien de grootte van de goudnanostaafjes vergelijkbaar is met de UV-golflengte, kan het elektrische veld (van de lichtgolf) een resonante elektronenbeweging van de goudlektronen opwekken als het langs de lange as van de staafjes

gepolariseerd is. Deze versterking van het elektrische veld leidt tot een grotere elektronenemissie.

Daarnaast tonen we foto-emissie aan van chirale BINAP-moleculen. We zagen echter geen significant verschil tussen excitaties door licht van tegengestelde chiraliteit. Wellicht was onze moleculaire laag niet voldoende geordend. We karakteriseren onze opstelling en schatten dat deze gevoelig genoeg is om een emissieverschil van 1% te detecteren tussen excitatie met rechts- en linksdraaiend circulair gepolariseerd licht. Het in kaart brengen van het CISS-effect met een resolutie op nanometerschaal, in tegenstelling tot het meten van gemiddelden van een hele laag, zal een beter begrip en de constructie van betere apparaten die dit effect benutten mogelijk maken.



# ZUSAMMENFASSUNG

Moleküle, Kristallstrukturen und Viren sind zu klein, um sie mit dem bloßen Auge zu sehen. Trotzdem haben sie großen Einfluss auf unser tägliches Leben. Um diesen Mikrokosmos in immer kleinerem Maßstab zu erforschen, wurden Mikroskope erfunden. Wenn wir an Mikroskope denken, meinen wir in der Regel optische Mikroskope. Elektronenmikroskope hingegen erlauben uns andere Eigenschaften und kleinere Längenskalen zu untersuchen als mit konventionellen Lichtmikroskopen möglich ist. In dieser Arbeit ziehen wir immer wieder Parallelen zwischen Elektronen- und Lichtwellen, da sich die Elektronen wie quantenmechanische Wellen verhalten.

Anstatt eine Probe mit Licht zu beleuchten und zu messen, was reflektiert oder transmittiert wird, schicken wir bei einem Elektronenmikroskop Elektronen auf die Probe und erfassen, wie diese reflektiert oder transmittiert werden. Diese Experimente führen wir in unserem niederenergetischen Elektronenmikroskop (englisch low-energy electron microscope, LEEM) durch. Anstatt die Farbe, d. h. die Wellenlänge des Lichts, zu messen, können wir die Elektronenenergie messen (und einstellen), welche mit der quantenmechanischen Wellenlänge des Elektrons zusammenhängt. Sowohl in der Licht- als auch in der Elektronenmikroskopie nennen wir die Messung der Intensität als Funktion der Wellenlänge ein Spektrum.

Die Spektren dünner Materialien in dieser Arbeit lassen sich größtenteils durch Interferenz verstehen. Ebenfalls ein Konzept, das wir aus der Optik kennen. Optische Interferenz beantwortet Fragen wie: Warum erscheinen Seifenblasen in allen Farben des Regenbogens, obwohl sie aus farbloser Seifenlösung hergestellt sind? Die Antwort ist, dass die Wanddicke einer Seifenblase einige 100 Nanometer beträgt, was der Wellenlänge des Lichts nahekommt. Wenn das Licht zwischen der Vorder- und der Rückseite der Seifenblasenwand hin- und her gespiegelt wird, werden einige Wellenlängen, die der (doppelten) optischen Weglänge entsprechen, bevorzugt durchgelassen, während andere Wellenlängen reflektiert werden. Das Gleiche gilt für unsere dünnen Proben und die Wellenlänge der Elektronen, wenn auch in einer Größenordnung von weniger als einem Nanometer. Wir benutzen hierfür Elektronen mit einer Energie zwischen 0 und 25 eV, was sehr niedrig für ein Elektronenmikroskop ist. Daher fiel die Wahl auf das niederenergetische Elektronenmikroskop.

Graphen, zum Beispiel, ist eine kristalline Schicht aus Kohlenstoff, die nur ein Atom dick ist. Wenn wir zwei Graphenschichten haben, interferiert die Wellenfunktion des Elektrons, das zwischen diesen Schichten hin und her prallt, genauso wie die Lichtwelle in einer

Seifenblasenwand. Indem wir die Elektronenenergie und somit die Elektronenwellenlänge variieren, können wir die Spektren messen und finden ein charakteristisches Reflexionsminimum und Transmissionsmaximum bei 2,5 eV über dem Vakuumniveau. Wenn weitere Graphenschichten hinzugefügt werden, spalten sich diese Extrema auf und ergeben einen spektralen Fingerabdruck der Schichtanzahl. Die Intensität und Breite dieser spektralen Merkmale hängen mit der Wahrscheinlichkeit zusammen, dass das Elektron inelastisch aus seiner Bahn geworfen wird. Diese inelastische Streuung wird durch die inelastische mittlere freie Weglänge quantifiziert, die wir in Kapitel 3 bestimmen. Die inelastische mittlere freie Weglänge gibt an, wie weit ein Elektron im Durchschnitt fliegt, bevor es auf etwas trifft und Energie verliert. Je öfter das Elektron zwischen den Schichten hin und her springt, ohne gestört zu werden, desto schärfer sind die Extrema im Spektrum. Um es mit optischen Begriffen auszudrücken: Die Finesse des optischen Resonators (in der Optik ist es das Licht, das zwischen zwei Spiegeln hin und her geworfen wird) nimmt mit der Lebensdauer des Resonanzzustands zu.

Wir wenden dieses Interferenzmodell auf verschiedene zweidimensionale Materialien an, die vom leitfähigen Graphen über das isolierende hexagonale Bornitrid (hBN) bis hin zum halbleitenden Molybdändisulfid ( $\text{MoS}_2$ ) reichen.  $\text{MoS}_2$  unterscheidet sich von Graphen und hBN, da sich die Molybdänatome in einer 2D-Schicht befinden, die von oben und unten durch je eine Schicht Schwefelatome umschlossen („gesandwich“) ist. Daher sind die Proben von zwei- und dreischichtigem  $\text{MoS}_2$ , die wir in Kapitel 5 messen, schon relativ dick im Vergleich zu drei Lagen Graphen. Der Vergleich mit berechneten Reflexions- und Transmissionspektren zeigt, dass wir die Wechselwirkungen mit Elektronen sogar in diesem recht komplizierten Material messen und modellieren können.

Ein weiteres zentrales Konzept in der Physik ist Symmetrie: Wir fragen uns, ob ein Elektron wissen kann, ob es auf die Vorder- oder die Rückseite der Probe trifft. Bei einer Probe, die nur aus Graphen besteht, sind die Vorder- und die Rückseite der Probe nicht zu unterscheiden. Bei einer Probe, die auf der einen Seite aus Graphen und auf der anderen Seite aus hexagonalem Bornitrid besteht, kann es jedoch einen Unterschied in der Elektronenreflexion geben. In Kapitel 4 betrachten wir eine solche Probe mit gebrochener Symmetrie und zeigen, dass inelastische Streuungen entscheidend sind, wenn sich die Reflexion von der Unter- und Oberseite unterscheiden soll.

Im letzten Kapitel befassen wir uns mit einer anderen Art von Symmetriebrechung. Ein chirales Objekt ist ein Objekt, das nicht so gedreht und/oder verschoben werden kann, dass es wie seine gespiegelte Version aussieht. Das typische Beispiel für Chiralität (aus dem Griechischen *cheir*=Hand) sind unsere Hände, die spiegelbildlich sind, sich aber offensichtlich voneinander unterscheiden. Auf der Ebene von Molekülen haben chirale Moleküle die gleiche chemische Zusammensetzung, aber eine andere dreidimensionale Anordnung. Bemerkenswerterweise spielt diese Anordnung bei biologischen Prozessen eine große Rolle.

In Kapitel 6 verwenden wir ultraviolettes (UV) Licht, um Elektronen aus einer mit chiralen Molekülen bedeckten Oberfläche herauszuschlagen (photoelektrischer Effekt). Wir untersuchen die Wechselwirkung zwischen der Händigkeit der Lichtpolarisation und der Händigkeit der chiralen organischen Moleküle. Kürzlich wurde publiziert, dass die Chiralität

der Moleküle an den Spin der durchgelassenen Elektronen koppelt und diese filtert: ein Phänomen, das als chirality-induced spin selectivity-Effekt (CISS-Effekt) bekannt ist. Wir demonstrieren an 400 nm langen Goldnanostäbchen, dass wir den Polarisationszustand des Lichts beliebig variieren können. Da die Größe der Goldnanostäbchen mit der UV-Wellenlänge vergleichbar ist, kann das elektrische Feld (der Lichtwelle) eine resonante Schwingung der Goldelektronen anregen, wenn es entlang der langen Achse der Stäbchen polarisiert ist. Diese Verstärkung des elektrischen Feldes führt zu einer verstärkten Elektronenemission.

Darüber hinaus demonstrieren wir die Photoemission von chiralen BINAP-Molekülen. Allerdings konnten wir keinen Unterschied zwischen den Anregungen durch Licht mit entgegengesetzter Chiralität feststellen. Möglicherweise war unsere Moleküllschicht nicht ausreichend geordnet. Aus der Kontrollmessung von achiralen Teilen der Probe folgern wir, dass unser Versuchsaufbau empfindlich genug ist, um einen Emissionsunterschied von 1% zwischen der Anregung mit rechts- und linksseitig zirkular polarisiertem Licht zu erkennen. Die Abbildung des CISS-Effekts mit einer Auflösung im Nanometerbereich, im Gegensatz zur Messung von Durchschnittswerten einer ganzen Probe, wird ein besseres Verständnis und den Bau besserer Instrumente, die diesen Effekt nutzen, ermöglichen.



# ACKNOWLEDGEMENTS

This thesis would not have been possible without the support of colleagues and friends.

First, I want to thank my promotores Sense Jan van der Molen and Ruud Tromp for their guidance, encouragement, and feedback during the last four years. They fulfilled their roles of combined supervisor, manager, critical reader, and colleague excellently. Furthermore, I want to thank my fellow group members Tobias de Jong, Vera Janssen, Arash Tebyani, Guido Stam, Xing Chen, and Amin Moradi, who have been amazing team players when sharing an electron microscope and running experiments together. Of course, experiments would not be possible without the highly valued technical support of Marcel Hesselberth, Ruud van Egmond, and Federica Galli.

Also, Johannes Jobst, Daniël Geelen, and Aniket Thete as former group members were a big help in sharing their knowledge and experience.

I also want to thank Eugene Krasovskii for providing calculations whenever we asked and Jan van Ruitenbeek and Jędrzej Tepper for discussions throughout the project.

I was especially pleased with the students who enthusiastically drove our project forward every year. Thanks, Bob, Leander, Zhiyuan, Brenda, Sharif, and Resi for your contributions.

I am grateful to Jimi, Tycho, and Norman who always helped with small and big problems and shared their lunch. In that row, I want to thank my officemates turned beach volleyball team Alice, Amber, Jaimy, Kirsten, Koen, Marshall, Petr, and Stef. Also, my friends Corné, Karina, Kirsten, and Stefano who started their master's degrees with me in Leiden, chose different fields and stayed in touch. Special thanks go to the online lockdown support group with Gesa and Tim and Jannis, Konrad, Kennet, Georg, Thomas, and Dominik for providing an outside perspective.

Last but not least I thank my loving parents and extended family. You have been a great support and a safe haven.





# CURRICULUM VITAE

PETER SEBASTIAN NEU

10-10-1995 Born in Duisburg, Germany

2005 – 2014 Highschool

Gymnasium Broich, Mülheim an der Ruhr, Germany

2014 – 2017 Bachelor of Science in Physics

RWTH Aachen, Aachen, Germany

Thesis: Jet-Parton Assignment in Top-Quark-Pair Associated Higgs  
Events using an Iterative Deep Learning Method

2017 – 2019 Master of Science in Physics

Universiteit Leiden, Leiden, The Netherlands

Thesis: Electronic Transport in 1T-TaS<sub>2</sub> at Low Temperatures

2019 – 2024 Ph.D. Physics

Universiteit Leiden, Leiden, The Netherlands

Thesis: Low energy electron transmission through layered materials and  
chiral organic films



# LIST OF PUBLICATIONS

<https://orcid.org/0000-0001-9569-6220>

- [1] P.S. Neu, M. Šiškins, E.E. Krasovskii, R.M. Tromp, S.J. van der Molen, Electron transmission and mean free path in molybdenum disulfide at electron-volt energies, *Phys. Rev. B.* 107 (2023) 075427. <https://doi.org/10.1103/PhysRevB.107.075427>.
- [2] P.S. Neu, D. Geelen, R.M. Tromp, S.J. van der Molen, Extracting transverse electron mean free paths in graphene at low energy, *Ultramicroscopy.* 253 (2023) 113800. <https://doi.org/10.1016/j.ultramic.2023.113800>.
- [3] P.S. Neu, D. Geelen, A. Thete, R.M. Tromp, S.J. van der Molen, Complementary LEEM and eV-TEM for imaging and spectroscopy, *Ultramicroscopy.* 222 (2021) 113199. <https://doi.org/10.1016/j.ultramic.2020.113199>.
- [4] M.D. Baaske, P.S. Neu, M. Orrit, Label-Free Plasmonic Detection of Untethered Nanometer-Sized Brownian Particles, *ACS Nano.* 14 (2020) 14212–14218. <https://doi.org/10.1021/acsnano.0c07335>.
- [5] P.S. Neu, E.E. Krasovskii, R.M. Tromp, S.J. van der Molen, Bi-directional LEEM and eV-TEM spectra of a graphene-hBN heterostack, to be published.